Small rock-slope failures conditioned by Holocene permafrost degradation: a new approach and conceptual model based on Schmidt-hammer exposure-age dating, Jotunheimen, southern Norway.

BOREAS An international journal of Quaternary research

Small rock-slope failures conditioned by Holocene permafrost degradation: a new approach and conceptual model based on Schmidt-hammer exposure-age dating in Jotunheimen, southern Norway

Journal:	*Boreas*
Manuscript ID	BOR-005-2018.R1
Manuscript Type:	Original Article
Date Submitted by the Author:	27-Apr-2018
Complete List of Authors:	Matthews, John; Swansea University, Geography Winkler, Stefan; University of Würzburg, Department of Geography wilson, peter; university of ulster, environmental sciences Tomkins, Matthew; University of Manchester, Department of Geography Dortch, Jason; University of Kentucky, Kentucky Geological Survey Mourne, Richard; University of the West of England, Geograohy and Environmental Sciences Hill, Jennifer; University of the West of England, Geography and Environmental Sciences Owen, Geraint; Swansea UNiversity, Geography Vater, Amber; Swansea University, Geograpohy
Keywords:	small rock-slope failures (SRSFs), Schmidt-hammer exposure-age dating (SHD), permafrost degradation, Holocene Thermal Maximum, climate-change impacts, paraperiglacial processes, southern Norway

Small rock-slope failures conditioned by Holocene permafrost degradation: a new approach and conceptual model based on Schmidt-hammer exposure-age dating, Jotunheimen, southern Norway

JOHN A. MATTHEWS[1*], STEFAN WINKLER[2], PETER WILSON[3], MATT D. TOMKINS[4], JASON M. DORTCH[5], RICHARD W. MOURNE[6], JENNIFER L. HILL[6], GERAINT OWEN[1] AND AMBER E. VATER[1]

[1] *Department of Geography, College of Science, Swansea University, Singleton Park, Swansea SA2 8PP, Wales, UK*
[2] *Department of Geography and Geology, Julius-Maximilians-University Würzburg, Am Hubland, 97070 Würzburg, Germany*
[3] *School of Geography and Environmental Sciences, Ulster University, Cromore Road, Coleraine BT52 1SA, Northern Ireland, UK*
[4] *Cryosphere Research at Manchester, Department of Geography, University of Manchester, Manchester M13 9PL, UK*
[5] *Kentucky Geological Survey, 228 Mining and Mineral Resources Building, University of Kentucky, Lexington, Kentucky 40506, USA*
[6] *Department of Geography and Environmental Management, University of the West of England, Coldharbour Lane, Bristol BS16 1QY, UK*

* corresponding author: J.A.Matthews@Swansea.ac.uk

Rock-slope failures (RSFs) constitute significant natural hazards but the geophysical processes which control their timing are poorly understood. However, robust chronologies can provide valuable information on the environmental controls on RSF occurrence: information which can inform models of RSF activity in response to climatic forcing. This paper uses Schmidt-hammer exposure-age dating (SHD) of boulder deposits to construct a detailed regional Holocene chronology of the frequency and magnitude of small rock-slope failures (SRSFs) in Jotunheimen, Norway. By focusing on the depositional fans of SRSFs ($\leq 10^3$ m^3), rather than on the corresponding features of massive RSFs (~10^8 m^3), 92 single-event RSFs are targeted for chronology building. A weighted SHD age-frequency distribution and probability density function analysis indicate four centennial- to millennial-scale periods of enhanced SRSF frequency, with a dominant mode at ~4.5 ka. Using change detection and discreet Meyer wavelet analysis, in combination with existing permafrost depth models, we propose that enhanced SRSF activity was primarily controlled by permafrost degradation. Long-term relative change in permafrost depth provides a compelling explanation for the high-magnitude departures from the SRSF background rate and accounts for (1) the timing of peak SRSF frequency, (2) the significant lag (~2.2 ka) between the Holocene Thermal Maximum and the SRSF frequency peak and (3) the marked decline in frequency in the late-Holocene. This interpretation is supported by geomorphological evidence, as the spatial distribution of SRSFs is strongly correlated with the aspect-dependent lower altitudinal limit of mountain permafrost in cliff faces. Results are indicative of a causal relationship between episodes of relatively warm climate, permafrost degradation and the transition to a seasonal-freezing climatic regime. This study highlights the importance of permafrost degradation as a conditioning factor for cliff collapse, and hence the importance of paraperiglacial processes; a result with implications for slope instability in glacial and periglacial environments under global warming scenarios.

Key words: small rock-slope failures (SRSFs), Schmidt-hammer exposure-age dating (SHD), permafrost degradation, Holocene Thermal Maximum, climate-change impacts, paraperiglacial processes, southern Norway

Rock-slope failures (RSFs) are indicative of instability in the landscape and reflect several geophysical processes and potential trigger factors related to rock mechanics, geomorphology, hydrology and environmental change. Moreover, RSFs constitute significant natural hazards. As a result, understanding the environmental controls on RSF occurrence provides crucial information which can inform modelling of future RSF activity in response to climate forcing (Rapp 1960a, 1960b; Brunsden & Prior 1984; Evans et al. 2006; Clague & Stead 2012; Davies 2015).

Numerous RSFs have been investigated in regions of high relief and, in some cases, RSF deposits have been dated (e.g. Korup et al. 2007; Ballantyne et al. 2014a, 2014b). However, previous research has primarily focused on modern examples, spectacular cases or small numbers of massive rock-slope failures (MRSFs; ~10^8 m^3). Which, in combination with uncertainty associated with current geochronological approaches, limits our understanding of the fundamental geophysical processes and environmental controls that determine RSF occurrence. Particular studies of RSFs have used a variety of techniques and, on some occasions, a combination of geochronological methods (Lang et al. 1999; Hermanns et al. 2000; Crosta & Clague 2009; Deline & Kirkbride 2009; Prager et al. 2009; Pánek 2014; Böhme et al. 2015; Moreiras et al. 2015; Mercier et al. 2017), but the opportunities for accurate dating are relatively rare.

The primary method for numerical-age dating of RSF deposits is terrestrial cosmogenic nuclide dating (TCND; ^{10}Be, ^{26}Al, ^{36}Cl) as this technique permits direct sampling and age determination of the exposed rock surfaces associated with RSFs (Hermanns et al. 2001, 2004, 2017; Cossart et al. 2008; Dortch et al. 2009; Ivy-Ochs et al. 2009; Penna et al. 2011; Ballantyne & Stone 2013; Ballantyne et al. 2013, 2014a, 2014b; Böhme et al. 2015; Schleier et al. 2015, 2017). However, the high financial cost of this technique limits its routine application which, in turn, often prevents statistically robust identification and rejection of erroneous results (Tomkins et al. 2018b). Consequently, there are still few reliable chronologies of RSFs which limits our understanding of the environmental factors determining their spatial and temporal occurrence.

In this paper we develop a methodology for the investigation and dating of RSFs, with targeted study of 'small rock-slope failures' (SRSFs; < 10^3 m^3). This focus has the advantage over MRSFs of permitting the dating and study of a relatively large sample of simple, likely single-event RSFs within a specified region. The methodology has been developed in conjunction with the relatively new calibrated-age dating technique of Schmidt-hammer exposure-age dating (SHD) (Shakesby et al. 2006, 2011; Matthews & Owen 2011; Matthews et al. 2015; Matthews & Wilson 2015; Winkler et al. 2010, 2016; Wilson et al. 2017). SHD has the potential to estimate the numerical age of rock-surface exposure at low cost with comparable accuracy and precision, and greater representativeness, than TCND over the Late

Glacial and Holocene (cf. Winkler 2009; Winkler & Matthews 2010; Matthews & Winkler 2011; Matthews et al. 2013; Wilson & Matthews 2016; Tomkins et al. 2016, 2018a, 2018b, 2018c).

Specific objectives of this paper are three-fold:

- To establish a Holocene chronology of SRSF events in the alpine zone of Jotunheimen, southern Norway and identify any phases of instability;
- To explore relationships between the timing of Holocene SRSF events and regional environmental changes, including climatic changes; and
- To develop further the potential of SHD as a calibrated-age dating technique in the context of RSFs.

Study area and environmental context

SRSFs were investigated in a broad area of northern Jotunheimen, the highest mountain massif in southern Norway, which culminates in Galdhøpiggen (2469 m above sea level; a.s.l.). The study area extends from Sognefjell in the west to Veodalen in the east (Fig. 1). Most SRSFs were found in Leirdalen, Bjørndalen (a western tributary valley to upper Leirdalen) and Gravdalen. The SRSFs occurred over an altitudinal range of 600 m (950-1550 m a.s.l.), mainly above the tree line, which lies at ~1000-1100 m a.s.l., in the alpine zone, and mainly in the low- and mid-alpine belts (Moen 1999). Examples of SRSFs from the study area are shown in Fig. 2.

Climatic data from the Sognefjell meteorological station (1413 m a.s.l.) indicate a mean annual air temperature of +3.1 ºC (mean July temperature +13.4 ºC; mean January temperature –10.7 ºC), and a mean annual precipitation of 860 mm, much of which occurs as snow (climatic normals AD 1961-1990; Aune 1993; Førland 1993). These data are consistent with a lower altitudinal limit of discontinuous permafrost at ~ 1450 m a.s.l. in the Galdhøpiggen massif (Ødgård et al. 1992; Isaksen et al. 2002; Farbrot et al. 2009; Lilleøren et al. 2012) with permafrost limits rising eastwards as continentality increases (Etzelmüller et al. 2003; Ginås et al. 2017). However, Hipp et al. (2014) have demonstrated a large difference of several hundred metres in the lower limits of permafrost between north- and south-facing rock walls. In the Galdhøpiggen massif, the lower altitudinal limit of rock-wall permafrost is located at 1500-1700 m a.s.l. in south-facing rock walls but only 1200-1300 m a.s.l. in shaded, north-facing rock walls (Hipp et al. 2014). Small valley glaciers, cirque glaciers and ice caps are common at and above these altitudes on the surrounding mountain peaks and plateaux (Andreassen & Winsvold 2012).

The metamorphic geology of the region consists primarily of pyroxene-granulite gneiss with peridotite intrusions and quartzitic veins (Battey & McRitchie 1973, 1975; Lutro & Tveten 1996), and gabbroic gneiss in the area investigated on Sognefjell (Gibbs & Banham 1979). Only boulders and bedrock of pyroxene-granulite gneiss and gabbroic gneiss were used in this study, as described below. Although these broad lithological categories include quite variable mineralogy, any differences in surface R-values due to lithology will likely be significantly smaller than the effect of variable exposure age given the relatively long Holocene timescales of exposure and limited climatic variability within the study region.

Topographically, most of the valley-side slopes have experienced a considerable degree of glacial erosion, although elements of ancient palaeic surfaces are preserved in the landscape (Ahlmann 1922; Gjessing 1967; Lidmar-Bergström et al. 2000) due, at least in part, to non-erosive, cold-based conditions during glaciations.

Jotunheimen was located near the position of the main ice-divide and ice-accumulation area of the Scandinavian ice-sheet at the maximum of the Last (Weichselian) Glaciation. Deglaciation of the main valleys is likely to have occurred by ~9.7 ka, following the Erdalen Event, late in the Preboreal chronozone (Dahl et al. 2002; Matthews & Dresser 2008; Velle et al. 2010). Most glaciers appear to have melted away during the Holocene Thermal Maximum (Nesje 2009) when permafrost limits were also higher than today (Lilleøren et al. 2012), but regenerated during neoglaciation, certainly by 5.5 ka and possibly as early as 7.6 ka (Ødgård et al. 2017). Both neoglaciation and lowering of permafrost limits occurred as a result of climatic deterioration (cooler and wetter) in the late Holocene, culminating in the Little Ice Age glacier maximum of the eighteenth century (Matthews 1991, 2005; Matthews & Dresser 2008). Future predicted mean annual warming of 0.3-0.4 ºC per decade in Scandinavia (Benestad 2005) is likely to lead to unprecedented glacier retreat (Nesje et al. 2008) and a continuing rise in permafrost limits (Lilleøren et al. 2012).

Methodology

Definitions and criteria for recognition of SRSFs

The term 'rock-slope failure' (RSF) refers to both (1) a mass-movement process involving the deformation and loss of integrity of a volume of intact bedrock followed by its *en masse* collapse and downslope movement under gravity and (2) the resulting landform. This definition is used here to distinguish RSF from 'rockfall' – the smaller-scale process involving the piecemeal detachment and free fall of individual rock particles – even though the term rockfall is commonly used at all scales, including the largest landslides and rock avalanches (MRSFs), which are often complex and multiphase (cf. Bates & Jackson 1987; Cruden & Varnes 1996; Braathen et al. 2004; Luckman 2004; Evans et al. 2006; Hermanns et al. 2006; Jarman 2006; Frattini et al. 2012; Hermanns & Longva 2012; Shakesby 2014; Brideau & Roberts 2015).

Fundamental to this study was the selection of SRSF landforms that represented, as far as it was possible to ascertain, the product of single events. Criteria for recognition of such SRSFs were as follows:

- a compact and coherent depositional fan of predominantly angular boulders located close to a bedrock cliff.
- a simple erosional scar in the cliff, immediately upslope of the fan, which is comparable in scale to the fan and therefore represents the likely source of the failed rock material;
- an absence of alternative sources of boulders up-slope of the scar.

Although no upper limit was placed on the size of the SRSFs recognized in this study, these criteria become less easily satisfied as RSFs increase in size. The lower size limit was the practical one of sufficient boulders for reliable Schmidt hammer measurement. Thus, the size range included in the study was determined by the RSFs in the region. Furthermore, the 92 investigated cases represent the whole population of SRSFs that satisfied the above criteria in the study area.

Measurement of SRSF characteristics

Estimates were made in the field of the length and average width of the depositional fan of each SRSF. Aspect and the altitude of the fan apex were estimated from topographic maps at a scale of 1:50,000 with a contour interval of 20 m, supplemented by altimeter and GPS measurements in the field. Fan volume was calculated from the length and average width measurements, assuming an average fan thickness of 1 m and a voids fraction (volume of voids/total fan volume) of 40%. Although some of the largest fans are thicker than 1 m in places, all are thinly spread across and down slope and rarely involve piles of debris. Lower voids fractions have generally been used for MRSFs, rock avalanches, talus and other mass movement types involving mixed particle sizes, fine matrix and/or compacted material (Owen et al. 2010; Sass & Wollny 2001; Hungr & Evans 2004; Wilson 2009; Stock & Uhrhammer 2010; Sandøy et al. 2017). The value of 40% is justified given the absence of fine matrix (Fig. 2) and lack of compaction, and its compatibility with similar values for clean, open-graded, angular aggregate material used as backfill in foundation engineering (StormTech 2012; cf. Dann et al. 2009).

Measurement of Schmidt-hammer R-values

N-type mechanical Schmidt hammers (Proceq 2004; Winkler & Matthews 2014) were used to measure rebound (R-) values from 100 boulders in each depositional fan. R-values reflect lithologically-determined rock hardness and the compressive strength of the rock surface: hence, R-values decline following exposure of a rock surface to subaerial weathering. For boulder surfaces of the same lithology but differing age, R-values therefore reflect the exposure age (time elapsed since exposure) of the rock surface. Use of one impact per boulder from a large sample of boulders ensures that the R-value frequency distribution can be used to approximate the boulder-age distribution (Matthews et al. 2014, 2015).

Precautions taken to eliminate or reduce possible sources of uncertainties and errors in Schmidt-hammer measurement included avoiding unstable or small boulders, boulder or bedrock edges, joints or cracks, unusual lithologies and lichen-covered or wet surfaces (cf. Shakesby et al. 2006; Matthews & Owen 2010; Viles et al. 2011). Rock surfaces were not cleaned or artificially abraded prior to impact with the Schmidt hammer (cf. the carborundum treatment of Viles et al. 2011) because such treatment would likely remove age-related weathering effects. However, there is continued debate as to whether rock surfaces should be abraded prior to testing (Moses et al. 2014) although a consistent sampling approach may enable age-related information to be retained (c.f. Tomkins et al. 2018b). Where possible, horizontal boulder surfaces were impacted but only vertical rock faces were available on cliffs. The two hammers used had been recently re-calibrated at a recognised service centre and were tested frequently on the manufacturer's test anvil throughout the study to

ensure there had been no deterioration in instrument performance following large numbers of impacts (cf. McCarroll 1987, 1994; Winkler & Matthews 2016). Measurements at 84 sites were restricted to rock surfaces of pyroxene-granulite gneiss. At the 8 sites on Sognefjell, gneissic rocks with gabbroic textures were used, which necessitated a separate calibration equation (see below).

Testing the validity of the approach

In order to test the validity of our approach and especially whether the boulders comprising the depositional fans actually represent single rock-failure events and whether the local source of the boulders had been correctly identified, R-value distributions associated with six fans and their corresponding scars were investigated. Two separate tests of validity were conducted.

First, in the *fan-scar comparison test,* a comparable sample of R-values (n = 100) from the surface of the corresponding scar was compared with the R-value distribution of the fan to identify whether or not the scar was the likely source of the boulders in the fan. If the scar was indeed the source of the boulders, the expectation would be no significant difference in the R-values derived from the scar and its corresponding fan because both would have experienced exposure over the same period of time.

Second, the *unfailed-cliff test* required a comparable sample of R-values (n = 100) from the adjacent intact (unfailed) bedrock cliff and also aimed to establish that the cliff was the bedrock source for the fan boulders. If this was the case, it would be expected that R-values from the unfailed cliff would be similar to or lower than the R-values of both the scar and the fan. Any departure from these expectations would indicate possible flaws in our approach.

The principles behind the fan-scar comparison test and the unfailed-cliff test are illustrated in Fig. 3, which also shows the expected relationships between R-values from the fans and R-values from the rock surfaces used as control points in the calibration equations.

Calibrated-age dating using SHD

Although there was earlier use of the Schmidt hammer for dating purposes (e.g. Matthews & Shakesby 1984; Nesje et al. 1994; Aa & Sjåstad 2000; Aa et al. 2007), SHD has been developed more recently as a calibrated-age dating technique (Colman et al., 1987) incorporating measures of uncertainty based on statistical confidence intervals (cf. Shakesby et al. 2006; Matthews & Owen 2011; Matthews & Winkler 2011; Matthews & McEwen 2013). Critically, this involves the derivation of a calibration equation and confidence limits for age.

The calibration equation is based on linear regression of surface age (Y) on mean R-value (X):

$$Y = a + bX \quad (1)$$

A linear relationship can be justified on both theoretical and empirical grounds. Although chemical weathering rates are likely to decline over longer timescales (Colman 1981; Colman & Dethier 1986; Stahl et al. 2013; Tomkins et al. 2018a, 2018b), near-linear rates can be expected over the Holocene timescale, especially where relatively resistant lithologies are subject to relatively slow rates of chemical weathering in a periglacial environment (André 1996, 2002; Nicholson 2008, 2009; Matthews & Owen 2011; Matthews et al. 2016). Although physical (freeze-thaw) weathering is well known in periglacial environments, it is highly dependent on moisture availability for ice-lens growth (Hallet et al. 1991; Hall et al. 2002; Murton et al. 2006; Matsuoka & Murton 2008) and there is no evidence that it has affected the well-drained surfaces used in this study (neither boulders in the dated depositional fans nor bedrock control surfaces).

Furthermore, Shakesby et al. (2011) specifically tested the linearity assumption in relation to granite boulders on independently-dated staircases of raised beaches deposited since 10.4 ka in northern Sweden, with the conclusion that the relationship between mean R-value and age was best described by a linear function. The same conclusion can be reached from age-calibration curves in the British Isles (Tomkins et al. 2018a) and the Pyrenees (Tomkins et al. 2018b), which are based on 54 and 52 ^{10}Be TCND-dated granitic surfaces respectively, all associated with glacial depositional or erosional landforms (moraine boulders or ice-sculpted bedrock). While the Pyrenean age-calibration curve is clearly non-linear over the full age range of ~50 ka, both age-calibration curves evidence linearity over the last ~20 ka. Other studies that have suggested non-linear relationships have involved long timescales and/or have had insufficient control points to test the linearity assumption rigorously over the Holocene timescale (e.g. Betts & Latta 2000; Sánchez et al. 2009; Černá & Engel 2011; Stahl et al. 2013).

Based on two control points, the b coefficient can be defined as:

$$b = (y_1 - y_2) / (x_1 - x_2) \quad (2)$$

where x_1 and x_2 are the mean R-values of the older and younger control points, respectively, and y_1 and y_2 are their respective ages. Once the b coefficient is known, the a coefficient is found by substitution in equation (1). Only two control points of widely differing age are available from Jotunheimen (see below). Provided they are of good quality, however, two control points are sufficient for accurate R-value calibration provided the underlying relationship between R-value and age is approximately linear.

For a landform produced by a single event, the SHD age resulting from this calibration is the average age of the surface boulders and hence the landform age (Matthews et al. 2015). Confidence intervals for the SHD age (95%) are calculated as the total error (C_t) by combining the error associated with the calibration equation (C_c) with the sampling error associated with the surface to be dated (C_s):

$$C_t = \sqrt{(C_c^2 + C_s^2)} \quad (3)$$

$$C_c = C_o - [(C_o - C_y)(R_s - R_o) / (R_y - R_o)] \quad (4)$$

$$C_s = b[ts / \sqrt{(n-1)}] \quad (5)$$

where C_o and C_y are the 95% confidence intervals of the older and younger control points (in years); and R_o, R_y and R_s are the mean R-values of the older control point, the younger control point and the surface to be dated, respectively. C_s depends on the number of R-value impacts on the surface to be dated (sample size, n), the standard deviation of those impacts (s), and Student's t statistic. Thus, the confidence interval (C_t) associated with any SHD age depends not only on the sample sizes used to establish the calibration equation and characterize the surface to be dated but also the natural variability exhibited by all the rock surfaces involved.

Control points for calibration equations

For this study, we constructed separate calibration equations for rock surfaces composed of pyroxene-granulite gneiss and gabbroic gneiss (each equation based on two control points). Data for the older control points, which relate to glacially-scoured bedrock surfaces, were taken from Matthews & Owen (2010). Their data from four sites in Leirdalen and Gravdalen (S and E Smørstabbtindan) were used for the pyroxene-granulite gneiss calibration equation: four sites near Leirbreen and Bøverbreen, close to Sognefjell (W Smørstabbtindan) supplied the data for the gabbroic gneiss calibration equation (Fig. 1).

Evidence for deglaciation of these sites is provided by basal ^{14}C dates from peat bogs and lakes in Leirdalen, Bjørndalen, and on Sognefjell (Table 2). These ^{14}C dates were recalibrated to calendar age ranges with the OxCal online program (v.4.3) using the IntCal13 calibration dataset (Reimer et al., 2013). Although one of the calibrated age ranges is significantly older, 9.7 ka is the only date for deglaciation that is compatible with the other four ^{14}C dates. Use of 9.7 ka as the age of the old control points for SHD calibration can be justified on the further grounds that it is the expected date for termination of the Erdalen Event in neighbouring regions (Dahl et al. 2002) and is consistent with empirical evidence for and large-scale modeling of deglaciation in southern Norway (Dahl et al. 2002; Goehring et al. 2008; Nesje 2009; Mangerud et al. 2011; Hughes et al. 2016; Stroeven et al. 2016). Thus, the potential errors in the old control points appear to be small in relation to the calibration errors (C_c and C_s) that are taken fully into account in this study.

Calibration equations given in Matthews & Owen (2010) for these rock types could not be used because their younger control points were derived from glacially-abraded surfaces from glacier forelands. Such smooth surfaces are not appropriate as a source of young control points for dating the exposure-age of boulders originating from SRSFs, which are rougher in texture yielding lower R-values than abraded surfaces of the same age (Shakesby et al. 2006; Matthews & McEwen 2013; Matthews et al. 2015). In contrast, after prolonged weathering, originally smooth surfaces are expected to yield similar R-values, and hence SHD ages, to initially rough surfaces.

Young control points with similar roughness properties to fresh boulder surfaces derived from SRSFs were therefore sought. These included: (1) boulders and bedrock surfaces produced by a recent rock-slope failure in Gravdalen and (2) bedrock exposed recently in road cuts in Gravdalen and on Sognefjell (Fig. 1). Both

types of surfaces have been shown in previous studies to yield R-values that are statistically indistinguishable from each other provided sufficient care is taken to impact only truly fresh rock surfaces (Matthews & Wilson 2015; Matthews et al. 2016). Furthermore, both types of recent rock surfaces used as young control points in this study were lichen-free and hence were assigned a maximum exposure age of 25 years based on various estimates of the time required for the establishment (ecesis) of crustose lichens on bedrock surfaces in this environment (Matthews 2005; Matthews & Owen 2008; Matthews & Vater 2015). Errors in the age of the young control point are therefore considered to be negligible in the context of this study.

Chronology construction and analysis

Holocene chronologies of SRSF events were constructed from the SHD ages of the 92 SRSF fans using a number of statistical approaches. First, graphical analysis of age-frequency distributions used 2000-yr, 1000-yr, 500-yr and 200-yr time intervals to define major clusters of SHD ages and hence possible multi-centennial to millennial phases of enhanced SRSF frequency (Matthews et al. 2009; Matthews & Seppälä 2015). Based on the same events weighted according to their rock volume, a second chronology was constructed showing the changing magnitude of SRSF events through the Holocene.

In order to take account of dating uncertainty, a weighted age-frequency distribution was constructed in which each SHD age was plotted over five 200-yr age classes: a weight of 4 was used for the central class; the second and fourth classes were weighted 2. Thus, the SHD age was plotted over a range of 1000 yr, consistent with the average 95% confidence interval of ± 991 yr calculated for the 92 SRSF fans (see below). One-sample χ^2 tests were used to test the hypothesis that the dated events were sampled from an underlying population of events with an even distribution through time.

To support weighted age-frequency analysis, the distribution of calculated SRSF ages was analysed using probability density function analysis. Probability density estimates (PDEs) were produced and modelled to separate out individual Gaussian distributions using the KS density kernel in MATLAB (2015) and a dynamic smoothing window based on age uncertainty (c.f. Dortch et al. 2013). The sum of individual Gaussian distributions integrates to the cumulative PDE at 1000 iterations to obtain a good model fit. The goodness of fit between the re-integrated PDE, which is derived from individual Gaussian distributions, and the cumulative PDE, which is derived from the full age dataset, is indicated graphically. PDE analysis was repeated using a number of individual Gaussian distributions (n = 1-10). To avoid over-interpretation of SRSF modes, the PDE model with the minimum number of individual Gaussian distributions, which also achieved a good model fit, was selected. This analytical method has primarily been employed in studies using ^{10}Be (cf. Dortch et al. 2013; Murari et al. 2014) or SHD (Barr et al. 2017; Tomkins et al. 2018a; 2018b; 2018c) to account for negative or positive skew of moraine boulder datasets and to identify and reject ages that are compromised by moraine degradation (Briner et al. 2005; Heyman et al. 2011) or nuclide inheritance (Hallet & Putknonen 1996). In these applications, PDE analysis and interpretation of individual Gaussian distributions (cf. Fig. 3 in Dortch et al. 2013) is based on the assumption that analysed ages relate to a single event e.g. moraine deposition. This assumption is clearly not

applicable to the analysis of SRSF ages, as each numerical age relates to a distinct event and an individual landform. As a result, individual Gaussian distributions are interpreted as reflecting the temporal clustering of events. The characteristics of individual Gaussian distributions, i.e. the peak probability density, width of PDE tails, 1σ uncertainties and the number of contributing ages (Fig. 7), were used to assess the significance and temporal clustering of SRSF events in Jotunheimen over the last ~10 ka.

The individual distributions resulting from the PDE analysis indicated that further analysis was necessary. Thus, a change detection analysis approach was undertaken in MATLAB (2015) to identify statistically unique events. Change detection analysis utilizes the cumulative sum algorithm (cusum), which is commonly used to detect abrupt change in time series data in fields ranging from seismology (Dera & Shumwayb 1999), remote sensed imagery (Lu et al. 2016), and GPS monitoring (Goudarzi et al. 2013). Parameters were set by using the average frequency and occurrence (~1 occurrence per 100 years) of SRSFs throughout the Holocene to filter out 'background' SRSF occurrence. The alarm limit was set at ≥2 standard errors above background. To further explore the temporal pattern of SRSFs, discreet Meyer wavelet analysis was undertaken in MATLAB (2015) to decompose SRSF occurrence through time. Wavelets are discreet oscillations in both time and amplitude and, as such, are useful for identifying discreet events. Wavelet analysis has been used to identify climate signals from various records including δO^{18} (Lau & Weng 1995), and sea surface temperature (Torrence & Compo 1998). The 100 yr binned SRSF age data was passed though the discreet Meyer wavelet with six levels of deconvolution.

Major and minor changes in SRSF activity were then compared with changes in regional Holocene climatic and other geo-environmental indicators to infer possible causes. Specific analyses were performed to investigate relationships between the occurrence of SRSF events and the lower altitudinal limits of discontinuous permafrost using aspect-dependent limits determined for rock walls in the Galdhøpiggen massif by Hipp et al. (2014). The current (AD 2010-2013) lower limits that were used for rock walls facing north, east, south and west were 1250 m, 1450 m, 1600 m and 1450 m, respectively.

Results

Data on the SRSFs

Data on the size and environmental characteristics of the SRSFs are summarized in Table 1 and Fig. 4. The volume of the fans (Fig. 4A) ranges from 12 to 2520 m^3, with 90% <1000 m^3, 40% <100 m^3 and a median size of only 180 m^3. The altitudinal range is 960 to 1550 m a.s.l. (Fig. 4B), with a mean altitude of 1340 m a.s.l. There is a preferred aspect with 43% facing east, 34% facing south and 17% facing west, but only 5% facing north (Fig. 4C).

Schmidt-hammer R-values vary widely between SRSFs (Table 1) and the frequency distribution of mean R-values reveals several important features (Fig. 4D). Mean R-values exhibit a very wide range of >20 units from 37.0 to 57.5. The overall

mean R-value across the 92 SRSFs is 48.2 but those R-values associated with gabbroic gneiss (overall mean R-value 39.4, n = 8) are appreciably lower than the remainder involving pyroxene-granulite gneiss (overall mean R-value 49.1, n = 84). The latter value corresponds closely with the 49-50 modal class for the distribution.

Control-point data and calibration equations

Data from the control points (Table 3) indicate widely different mean R-values (differing by at least 20 units) for surfaces that differ in age by ~9700 years. It should also be noted that the overlapping 95% confidence intervals associated with each pair of replicates for particular control points indicate that their mean R-values do not differ significantly from each other. Control surfaces of the same age on different lithologies are, however, characterized by non-overlapping confidence intervals, and thus show significantly different mean R-values and justify the use of separate calibration equations for SRSFs developed in pyroxene-granulite gneiss and gabbroic gneiss. The calibration equations derived from these data for the two lithologies are shown in Figure 5 alongside the linear relationships they represent.

Fan-scar-cliff comparison tests

Mean R-values for three of the six fans tested did not differ significantly from the mean R-values of the corresponding scars, in accordance with expectation (Fig. 3 and Table 4). However, three fans (Nos 51, 58 and 81) are characterized by mean R-values that are significantly lower than the mean R-values from their scars. This suggests one or more of four possible explanations: (1) rock surfaces of some boulders in these fans are more weathered because they include the products of older rock failures than those that produced the measured bedrock faces of the scars; (2) some of the measured R-values from boulders in the fans reflect the incorporation of bedrock surfaces that were pre-weathered on the cliff face before the failures occurred; (3) some of the R-values from boulders in the fans reflect the incorporation of inherited structures (e.g. joint planes) that were pre-weathered at depth before the failures occurred; and (4) at least part of the cliff bedrock is more resistant to weathering than the boulder surfaces measured in the fans. Interestingly, no fan exhibits a mean R-value that is significantly greater than that of its corresponding scar. This shows that even where more than one phase of activity seems possible, any blocks that were later removed from the scars were insufficient in number to affect appreciably the mean R-values of the fans.

Comparisons between scars and unfailed cliffs or between fans and unfailed cliffs are entirely in agreement with expectation. In three cases (fan Nos 5, 51 and 58) neither the mean R-values for scars and unfailed cliffs nor the mean R-values for fans and unfailed cliffs differ significantly, suggesting that all the exposed surfaces are of the same age (and relatively old). In the other three cases (fan Nos 46, 47 and 81) the mean R-values of the scars and the fans are both significantly higher than the mean R-values of the unfailed cliffs, confirming the SRSFs are younger than the exposure age of the unfailed cliffs.

Comparison of the mean R-values from unfailed cliffs with the values from the older control points given in Table 3 indicates that unfailed cliff surfaces were exposed during or immediately after deglaciation at ~9700 cal. BP. As all surfaces

yielded mean R-values lower than those characteristic of the younger control points (Table 4), it appears that fan deposition and scar exposure occurred throughout the Holocene and, in some cases, thousands of years after regional deglaciation. As a result, the temporal distribution of fan mean-R-values likely reflects the timing of single-event SRSF activity.

Temporal variations in SRSF activity

The age of each SRSF event, including its 95% confidence interval, is summarized graphically in Fig. 6A. Although there is some evidence of differences in the age distributions between the different valleys, there is no statistically significant correlation between SRSF age and altitude and no significant difference in age between aspects. The overall mean age of all 92 SRSF events is 5124 years, which equates with an average regional frequency of 1 in 105 years.

Simple age-frequency distributions of the SRSF events within the region as a whole are shown in Fig. 6B. Although these events occurred without any prolonged break in activity, their frequency varied considerably over the last ~10,000 years. The distribution based on 2000-yr time intervals has a single mode indicating an increase in the frequency of events through the early Holocene, a distinct peak in activity in the 6.0-4.0 ka time interval, and a consistent decline in activity thereafter. The use of 1000-year time intervals reveals two modes – at 8.0-7.0 and 5.0-4.0 ka, respectively. At least three modes can be recognized when 500-yr time intervals are used (at 9.0-8.5, 7.5-7.0 and 4.5-4.0 ka) and many more can possibly be discerned in the distribution based on 200-year time intervals. However, analysis of SRSF modes based on 200-year time intervals is not advisable, as this time interval (0.2 ka) is significantly smaller than the typical uncertainty of SRSF ages (~1 ka). Despite this, the hypothesis of an even distribution of SRSF events through time can be rejected at $p<0.01$ irrespective of the age classes used.

The weighted age-frequency distribution (Fig. 6C) has four modes (at ~ 8.9, 7.3, 5.9 and 4.5 ka), which suggests that only four minor phases of enhanced SRSF frequency are meaningful. Furthermore, according to the weighted distribution, the frequency of events declines steadily after ~4.5 ka with no marked fluctuations.

The temporal pattern in the magnitude of the SRSFs (rock volume), as shown in in Fig. 6D, is substantially the same as the frequency distribution (compare with use of a 200-yr interval in Fig. 6B). In particular, the age-volume distribution has a similar major peak between 4.8 and 4.2 ka, and relatively little activity before 9.0 ka or after 1.0 ka.

Probability density function analysis indicates that the spread of SRSF ages does not conform to a normal distribution (Fig. 7A) and instead, is best explained by 5 individual Gaussian age distributions (Fig. 7B). The sum of individual Gaussian distributions produces a re-integrated PDE which achieves a good model fit with the cumulative PDE. PDE analysis using < 5 individual Gaussian age distributions returns a poor ($n \leq 3$) or sub-optimal ($n = 4$) model fit. PDE analysis using > 5 individual Gaussian age distributions does not therefore significantly improve the model fit and instead risks over-interpretation of the number of SRSF modes. PDE analysis returns peak Gaussian ages (Fig. 7C) of 9.00 ± 1.13 ka ($n = 14$), 7.38 ± 0.99 ka ($n = 17$), 6.40

± 0.77 ka (n = 14), 4.50 ± 1.42 ka (n = 42) and 1.90 ± 1.42 ka (n = 18). Although these modes overlap with adjacent modes within 1σ, statistically significant differences between sequential Gaussian age distributions are revealed by two-sample Students t-tests ($p < 0.01$).

These Gaussian age distributions closely match the four modes identified in weighted age-frequency analysis, with a dominant mode at ~4.5 ka (Fig. 7B). This mode is the highest probability Gaussian distribution, comprises a significant number of SRSF events (n = 42; Fig. 7D) and accounts for a large proportion of total SRSF volume over the last ~10 ka (18,744 m^3). In contrast to weighted age-frequency analysis, PDE analysis returns an additional Gaussian age distribution during the late Holocene at ~1.9 ka. However, this is unlikely to reflect a period of enhanced SRSF activity as there is no clear clustering of SRSF ages (Fig. 7A), as evidenced by weighted age-frequency analysis. Instead, late Holocene ages likely reflect declining SRSF activity after the mid-Holocene peak.

The combined results of the age-frequency analyses and the Gaussian separation achieved for PDEs demonstrate that SRSF occurrence through time is non-uniform and multi-modal. Most notable is the high level of occurrence during the mid Holocene, the clear statistical significance of which is confirmed by the results of change detection analysis. The cumulative sum change detection graph (Fig. 8A) shows a clear peak in the rate of SRSF intensity between 4.8 and 2.6 ka, significantly exceeding the 2σ threshold, with the largest departure from background occurring at 4.3 ka. Conversely, SRSF intensity is significantly reduced beyond the negative 2σ threshold during the late Holocene at 0.6–0.1 ka. These peaks are a significant departure from the normal rate of occurrence during the Holocene. The three other modes identified above as statistically significant must be regarded as relatively small departures from background SRSF periodicity.

Meyer wavelet analysis was used to explore the two statistically significant departures (> 2σ) from the background SRSF rate, as identified by change detection analysis. The lowest frequency decomposed signal (d_6) is shown in Fig. 8C. The full analysis record is provided in Supplementary Fig. 1.

Discussion

Previous models of the timing of RSFs

Widely different conceptual models can be proposed to describe and explain the temporal distribution of Late Pleistocene and Holocene RSFs. A schematic representation of several models, each of which links a distinctive pattern of change in the frequency and/or magnitude of RSFs to one or more specific causes or triggers, is shown in Fig. 9. Although they have been based mainly on MRSFs, these models are introduced here as a basis for discussion of our Holocene SRSFs. It should be emphasised, moreover, that RSFs may be multicausal and that most if not all of the models have yet to be rigorously tested against data sets with a large number of consistently dated RSFs.

Model 1. – The '*continuity-of-activity model*', proposes that there are no

significant temporal variations in the frequency and/or magnitude of RSFs throughout the Holocene. Despite the small number of dated RSFs available in most studies, few authors have advocated this model. However, the model does appear to be consistent with the temporal distribution of about 60 RSFs located in an extensive area of the Alps centred on the Austrian Tyrol (Prager et al. 2008), which exhibits only limited evidence of temporal clustering at ~10.5-9.4 ka and 4.2-3.0 ka. Prager et al. (2008) attributed the continuity of activity to complex interactions between the processes characterizing models 2-5 together with rock-strength degrading processes such as time-dependent progressive fracture propagation that can both prepare and trigger slope instabilities.

Model 2. – The '*intermittent-earthquakes model*', which is applicable to tectonically active regions and assumes that RSFs are triggered directly by large-magnitude earthquakes generated by tectonically-driven uplift or other crustal stresses. Such earthquakes are essentially randomly distributed in time and therefore bear little or no relationship to deglaciation, climate or any of the other potential causative factors in models 3-5 that are effective in tectonically stable regions (see, for example, Fjeldskaar et al. 2000; Hermanns et al. 2001; Keefer 2002, 2015; Hewitt et al. 2008; Antinao & Gosse 2009; Stock & Uhrhammer 2010; Penna et al. 2011; McPhillips et al. 2014; Marc et al. 2015; Murphy 2015).

Model 3. – The '*deglaciation-close-tracking model*', is characterised by a dominant peak in RSF activity immediately (i.e. within the first millennium) following regional deglaciation, with subsequent asymptotic decline in activity. The temporal pattern of activity is therefore a typical paraglacial response (cf. Ballantyne 2002). Causal factors that may account for such a pattern include glacial unloading, glacial debuttressing, stress-release fracturing, enhanced groundwater pressure in rock joints and permafrost degradation, all closely associated in time with deglaciation (Fischer et al. 2006; Cossart et al. 2008; McColl 2012; McColl & Davies 2012; Ballantyne et al. 2014a, 2014b; Böhme et al. 2015; Deline et al. 2015; Mercier et al. 2017). Hermanns et al. (2017) found nearly half of 22 dated rock avalanches in southwest Norway occurred within the first millennium following local deglaciation. Although the majority of RSF events occur shortly after deglaciation, some occur much later, due to time-dependent fracture propagation and progressive failure (e.g. Eberhardt et al. 2004; Krautblatter et al. 2013; Phillips et al. 2017). The occurrence of recent RSFs on glacier forelands following the retreat of mountain glaciers from their Little Ice Age maximum limits provides some support for this model (Evans & Clague 1994; Holm et al. 2004; Matthews & Shakesby 2004; Arsenault & Meigs 2005; Allen et al. 2010; Stoffel & Huggel 2012).

Model 4. – The '*deglaciation-lagging model*', features a significantly delayed response to deglaciation. Peak RSF activity typically occurs within a few millennia of deglaciation and corresponds with maximum glacio-isostatic rebound (Hicks et al. 2000; Ballantyne & Stone 2013; Ballantyne et al. 2013, 2014a, 2014b; Cossart et al. 2014; Decaulne et al. 2016). The cause of RSF events is seen as fault reactivation and fracture propagation triggered by earthquakes, the frequency of earthquakes and RSFs generally diminishing through the Holocene as the rate of glacio-isostatic uplift declines.

Model 5. – The '*cool/wet-climate-response model*', which applies particularly

to the Holocene, reflecting several possible effects of climatic variations on RSF activity. Field monitoring, historical documentation and palaeo-studies indicate that precipitation variations can be a dominant trigger factor in the timing of RSFs but both cooler conditions and indirect effects such as variations in cleft water pressure, frost shattering and permafrost degradation have also been implicated in rock-slope instability (Eisbacher & Clague 1984; Matthews et al. 1997; Trauth et al. 2000, 2003; Dapples et al. 2003; Soldati et al. 2004; Prager et al. 2008; Crozier 2010; Borgatti & Soldati 2010; Blikra & Christiansen 2014; Zerathe et al. 2014; Johnson et al. 2017). Furthermore, Evans & Clague (1994), Huggel et al. (2010, 2012) and Stoffel & Huggel (2012) highlighted the possible effects of recent climate warming on RSFs, and direct solar heating of rock faces has also been examined as a possible trigger (cf. Allen & Huggel 2013; Collins & Stock 2016). In Fig. 7, model 5 assumes cool/wet conditions produce an increase in RSF activity, resulting in a strong rising trend through the late Holocene with fluctuations culminating in a Little Ice Age maximum of RSF activity.

A new model of Holocene SRSF activity in Jotunheimen

Based on analysis of Holocene SRSF activity in Jotunheimen and comparison with regional climatic and geo-environmental indicators, a new thermally-driven, permafrost-degradation model is proposed (Fig. 7, model 6). This model is characterized by several key elements:

- minimal activity following deglaciation in the early Holocene;
- maximum activity late in the mid Holocene on the multi-millennial timescale;
- declining activity through the late Holocene with a second minimum close to the present;
- secondary fluctuations on multi-centennial to millennial timescales throughout the Holocene;

This pattern of change bears little relationship to any of the previous models, which are clearly inappropriate in the context of these data. Model 1 can be rejected for Jotunheimen on the basis of the χ^2 tests in Table 5. Although there is an element of randomness in our data, and earthquakes do occasionally occur in this part of southern Norway, their magnitudes tend to be too low to be effective in triggering SRSFs inland from the seismically more active coastal and off-shore areas (cf. Bungum et al. 2000; Fjeldskaar et al. 2000; Hicks et al. 2000; Olesen et al. 2000; Blikra et al. 2006). Moreover, there is no sign of a dominant early-Holocene activity peak in our histogram or change detection analysis, which is the characteristic feature of the two deglaciation-related models (3 and 4). Absence of an early peak may well be accounted for by considerable thinning of the Late Weichselian Ice Sheet prior to final deglaciation in Jotunheimen (Goehring et al. 2008; Mangerud et al. 2011; Hughes et al. 2016; Stroeven et al. 2016), which is likely to have reduced the scale of any paraglacial effects on RSFs after ~10.0 ka. For example, over half (56%) of the estimated glacio-isostatic rebound of 160 m that has taken place in Jotunheimen since 12.0 ka was completed prior to 10.0 ka and a further quarter (26%) by 6.0 ka (Lysså et al. 2008). Finally, the temporal pattern of SRSF activity in Jotunheimen is negatively correlated with model 5, which indicates that cool/wet conditions should be rejected as the major cause of enhanced SRSF activity. Instead, this inverse pattern points to the counterintuitive conclusion that enhanced activity is linked to relatively warm

climatic conditions.

Association of SRSF activity with the thermal climate record

The possible associations between enhanced Holocene SRSF activity and relatively warm climatic conditions can be explored with reference to proxy temperature records and reconstructions of temperature-sensitive geo-environmental indicators (Fig. 10A-G).

The long-term annual air temperature trend for Northern Europe shown in Fig. 10B is a stacked pollen-based reconstruction expressed as deviations from the mean (Seppä et al. 2009). The Holocene Thermal Maximum (HTM) is clearly expressed in this figure from ~8.0 to 4.0 ka by mean annual temperatures consistently >0.5 °C higher than today. Alkenone-based temperature reconstruction similarly documents warmest sea-surface temperatures in the North Atlantic at this time (Eldevik et al. 2014; see also Jansen et al. 2008; Renssen et al. 2012). However, other reconstructions based on chironomids (Velle et al. 2010), aquatic macrofossils (Väliranta et al. 2015) and megafossils (Dahl & Nesje 1996; Paus & Haugland 2017), which are not dependent on tree-pollen production or ocean temperatures, indicate that the highest temperatures probably occurred at 10.0–8.0 ka. Mean summer temperatures estimated from pine-tree limits in the Scandes Mountains (Dahl & Nesje 1996), for example, peak at ~1.5 °C above present temperatures around 9.0 ka (Fig. 10C). An early temperature maximum at ~9.0 ka is also shown in the pollen-based reconstruction of July air temperature from Øvre Heimdalsvatnet in the low-alpine belt of eastern Jotunheimen (Fig. 10D, Velle et al. 2010). At this location, a temperature of at least 3.5 °C higher than present was attained by 9.0 ka, falling to the long-term Holocene average by 4.0 ka. Comparison with these reconstructions indicates that (1) SRSF frequency increased during the HTM and (2) maximum activity was not reached until late in the HTM.

Three other palaeorecords can be used to focus on shorter-term warm intervals comparable in scale with our minor phases of enhanced SRSF frequency (Fig. 10E-G). The first of these (Fig. 10E), based on a standardized temperature reconstruction derived from the record of $\delta^{18}O$ in the GISP 2 Greenland ice core (Alley 2004; Wanner et al. 2011, their Fig. 1a), shows periods of above average air temperature. Fig. 10F, based on the North Atlantic standardized stacked ocean ice-rafted debris (IRD) record (Bond et al. 2001; Wanner et al. 2011, their Fig. 3a), shows periods between IRD events, when sea-surface temperatures are likely to have been above the long-term average. Both sets of warm periods demonstrate only moderate agreement between themselves and with our minor phases of enhanced SRSF frequency. There is poorer agreement (particularly in the late Holocene after ~3.0 ka) with the final record, which relates to variations in the size of mountain glaciers in the study area (Fig. 10G). Glacier variations are widely accepted as climate indicators that reflect, in part, temporal variations in summer temperature, especially in the case of glaciers in continental locations where winter precipitation variations tend to be less effective than in maritime regions (Oerlemans 2005; Bakke et al. 2008; Nesje et al. 2008; Winkler et al. 2010). Local glacier variations in the Smørstabbtindan massif, Jotunheimen, which is centrally located in relation to the sites of our SRSF events in a relatively continental region of southern Norway, exhibit at least nine Holocene time intervals when the glaciers were smaller than they are today, including a prolonged

period from ~7.8 to 4.8 ka, which includes most of the HTM (Fig. 10G; Matthews & Dresser 2008).

Thus, overall, a strong case can be made for linking millennial-scale variations in SRSF activity to the thermal environment. However, causal mechanisms are required to answer the following questions: (1) why was maximum SRSF activity attained late in the mid-Holocene, rather than earlier in the HTM when temperatures were at a maximum; and (2) why was there not a closer relationship between the minor phases of enhanced SRSF activity and shorter-term warm periods, such as the Mediaeval, Roman and Bronze Age warm periods, in particular during the late-Holocene? We propose that permafrost degradation, and climate-dependent variation in permafrost depth, can explain the temporal pattern of SRSF activity and, in particular, the departure of the temporal pattern of SRSF activity from a simple 'warm-climate' model.

Conditionality of SRSF activity on permafrost degradation

To interpret the results of both the change detection analysis and Meyer wavelet analysis, a modelled permafrost record for Fennoscandia (Kukkonen & Šafanda 2001) is used (Fig. 8B). This provides a basis for attributing SRSF activity in Jotunheimen to permafrost degradation by focusing on relative changes to permafrost depth in bedrock over the last ~10 ka. The 5% porosity model was selected for comparison as this is more representative than the 0% porosity model given the numerous fractures that lead to slope instability and SRSFs. The permafrost model shows a significant decrease in depth beginning at ~8 ka and reaching a steady 'shallow' equilibrium by ~5 ka. Permafrost is relatively stable from 5 ka until ~0.6 ka when permafrost depth increases. This permafrost model is subdivided into five distinct periods and is related to the SRSF record as follows:

Phase 1: 10.0–8.1 ka ('stable phase'). – SRSF frequency is in equilibrium with permafrost, which is at its maximum depth, with no alarms detected in the change detection analysis and no low-order oscillations in the Meyer wavelet record. Bedrock permafrost is stable throughout this period and is used to define background Holocene depth. In this phase, persistent bedrock permafrost acts to stabilize slopes and limits major SRSF activity.

Phase 2: 8.1–4.8 ka ('transition phase'). – Progressive warming throughout the mid-Holocene, as recorded in palaeo-climate reconstructions, acts to decrease permafrost depth. In response, there is a minor progressive decrease in negative change detection rates and increase in positive change detection within 2σ. This trend is matched by Meyer wavelet analysis, with a progressive increase in SRSF frequency above the Holocene background rate. In this phase, a gradual (~3 ka) but clear transition from 'deeper' to 'shallower' permafrost (~28% depth change) is matched by a minor increase in SRSF frequency and may explain the minor phases of enhanced SRSF activity identified during this period. Moreover, this gradual change in permafrost depth, as opposed to a stochastic response to climate warming, provides a compelling explanation for the significant lag between SRSF activity and the HTM.

Phase 3: 4.8–2.6 ka ('peak phase'). – Permafrost depth is more-or-less stable and remains close to its minimum Holocene depth for ~2 ka. This period is matched by

SRSF activity, as change detection analysis records a significant, sustained and positive rate of change (> 2σ) for ~2.2 ka, with a maximum attained at ~4.3 ka and with SRSF frequency significantly exceeding the average frequency until ~3.3 ka (> 6σ). This change is matched by the Meyer wavelet record, with a peak at ~4.6 ka and a gradual decline to the Holocene background rate at ~2.5 ka. In this phase, persistent shallow permafrost may directly influence SRSF occurrence by (1) actively destabilizing bedrock cliffs and causing slope failure and/or by (2) weakening bedrock cliffs and making them more susceptible to other trigger factors.

Phase 4: 2.6–0.6 ka ('exhaustion phase'). – Permafrost depth remains relatively stable and shallow for ~2 ka, with no significant deviation from modelled depths during the 'peak phase'. However, there is a clear decrease in SRSF frequency after the mid-Holocene peak with a return to the Holocene background rate, as revealed by both change detection and Meyer wavelet analysis. In this phase, we propose that bedrock cliffs have reached a new equilibrium with permafrost, as the majority of slopes that can fail under these permafrost conditions have failed by this time; that is the supply of 'potentially failable' cliffs is exhausted. As a result, SRSF occurrence returns to an average frequency comparable with the 'stable phase' of the early Holocene.

Phase 5: 0.6 - 0.1 ka ('stabilization phase). – Contrary to the dominant Holocene trend, this short-term late-Holocene phase shows a clear increase in permafrost depth after ~0.6 ka. This transition is coeval with a statistically significant decrease in SRSF frequency (> 2σ) while Meyer wavelet analysis records the continued decrease in frequency below the Holocene background level. These data suggest that an increase in bedrock permafrost depth directly controls SRSF activity by stabilizing slopes and decreasing the susceptibility of bedrock cliffs to direct or indirect failure.

The correlation between SRSF frequency and permafrost depth in bedrock as modeled by Kukkonen & Šafanda (2001) provides a compelling explanation for the low-frequency variations in SRSF activity during the Holocene and, in particular for:

- the significant departure from mean Holocene SRSF frequency at the end of the mid Holocene;
- the lag between the HTM and the SRSF frequency peak;
- the low SRSF frequency in the early Holocene; and
- the marked decline in SRSF frequency near the end of the late Holocene (after ~0.6 ka).

These explanations are supported by change detection analysis and (d_6) Meyer wavelet analysis. A causal link between SRSF frequency and regional permafrost degradation is also supported by the close match between the altitudinal distribution of the 92 SRSFs and the current aspect-dependent lower altitudinal limit of permafrost in rock faces in the Galdhøpiggen massif (Hipp et al. 2014). Approximately 87% (n = 80) of SRSFs occur within ± 300 m of the limit and ~62% (n = 57) are ≤ 200 m below this limit. A small number of SRSFs are found above the permafrost limit (~16%; n = 15) but the majority are restricted to within ≤ 50 m above this limit. These data imply a causal relationship between SRSF occurrence and the time-dependent degradation and aggradation of bedrock permafrost during the Holocene, as driven by climate and locally controlled by aspect. Based on an altitudinal lapse rate of 0.6 °C per 100 m in mean annual air temperatures (MAAT), this implies that all SRSF sites would have

been in the permafrost zone when temperatures were 3.0 °C lower than today. It is likely, therefore, that much of the permafrost that had survived or developed in SRSF cliffs following deglaciation would have degraded during the HTM when MAAT is likely to have reached 2.0–3.0 °C warmer than at present and when permafrost limits would have been correspondingly higher (Lilleøren et al. 2012).

Higher-frequency changes in SRSF activity as reflected by weighted age-frequency (Fig. 6C) and (d_1 - d_5) wavelet analysis (see Supplementary Fig. 1) can be interpreted as representing Holocene background SRSF frequency after removal of the mid-Holocene peak of the change detection analysis (Fig. 8A). These higher frequency changes are more challenging to interpret, given the limited availability of palaeo-environmental records (e.g. seasonal paleo-precipitation data, storm-event chronologies, palaeoseismic and groundwater flux records) and the inherent SHD age uncertainties. The conceptual models related to deglaciation and characterized by early-Holocene peak activity (Fig. 9) can be discounted as these bear limited resemblance to the chronology of SRSF events.

Changes in permafrost depth might be expected to play a role in explaining the higher-frequency changes. However, we cannot preclude a contribution to higher-frequency variability from the continuity, earthquake, and cool/wet climate conceptual models (Fig.9). Thawing permafrost may be a direct trigger factor for SRSF events due, for example, to loss of strength or elevated hydrostatic pressure, or it may render the rock slope susceptible to other triggers involving meltwater from spring snow melt or extreme rainfall events in summer (Gruber et al. 2004; Gruber & Haeberli 2007; Krautblatter et al. 2013; Blikra & Christiansen 2014; Draebing et al. 2014; Krautblatter & Leith 2015; Messenzehl & Dikau 2017). Extreme summer rainfall events, which are likely to have been more frequent during warm periods, have been implicated in triggering debris-flow events in Leirdalen (Matthews et al. 2009) and might have triggered some SRSFs.

Further conceptual and methodological implications

Thus, the timing of SRSFs in this study, with fluctuating SRSF activity rising to a sustained peak at the transition from the mid- to late-Holocene, suggests the importance of progressive but intermittent permafrost degradation lagging behind the highest temperatures of the Holocene. Subsequent declining SRSF frequencies, in contrast, appear to signal exhaustion of the supply of failable cliffs and/or renewed aggradation of permafrost.

These fundamental findings recognize that Holocene SRSF activity in Jotunheimen essentially reflects paraperiglacial processes: that is, it is a conditional response to the transition from a permafrost to a seasonal-freezing climatic regime as permafrost depth decreases (cf. Mercier 2008; Scarpozza 2016; Matthews et al. 2017). While this model is primarily applicable to the SRSFs sampled in this study, it could be tested in comparable mountain regions. In particular, links between permafrost degradation and enhanced slope failure may explain SRSF frequency in regions with comparable seismotectonics, glaciation and deglaciation histories or climatic trends. Robust SRSF chronologies would need to be constructed to test the model, either using radiometric methods (e.g. ^{10}Be) or calibrated-age dating techniques (e.g. SHD).

Our new SRSF chronology indicates, moreover, that SHD can be used to generate reliable SRSF chronologies, although further work is necessary to verify this technique by directly comparing age estimates for individual landforms derived from both SHD and radiometric methods.

Finally, the recognition of a causal link between climate, permafrost degradation and enhanced slope instability may have important implications for glacial and periglacial environments under global warming scenarios. In particular, while widespread retreat of mountain ice caps and valley glaciers may trigger initial slope instability,our data suggest that the geomorphological impact of current climatic and deglacial trends and, in particular, the slow transition from glacial to periglacial, and to seasonal-freezing climatic regimes, may have a long-lasting impact on mountain environments.

Conclusions

(1) We have developed an approach to the exposure-age dating of a large sample of rock-slope failures, which involves adapting Schmidt-hammer exposure-age dating (SHD) as a calibrated-age dating technique to the specific characteristics of small rock-slope failures (SRSFs). SHD has provided an effective and low-cost method for constructing a regional Holocene chronology of SRSFs (12 to 2520 m^3) in the alpine zone of Jotunheimen.

(2) Focusing on a large sample of SRSFs enables the detection of temporal variations in the frequency and magnitude of events through the Holocene. Modes in a weighted age-frequency distribution at ~8.9, 7.3, 5.9 and 4.5 ka were substantiated by probability density function analysis, which produced individual Gaussian age distributions of 9.00 ± 1.13 ka, 7.38 ± 0.99 ka, 6.40 ± 0.77 ka and 4.50 ± 1.42 ka. Based on this analysis, SRSF activity was relatively low following deglaciation in the early Holocene and attained a maximum towards the end of the mid Holocene (~4.5 ka). Peak SRSF activity lagged behind the Holocene Thermal Maximum by at least ~2.2 ka and declined thereafter with a very low frequency of events during the last millennium.

(3) Using change detection and discreet Meyer wavelet analysis in combination with proxy temperature indicators and an existing permafrost depth model, we propose that enhanced SRSF activity was primarily controlled by permafrost degradation. As a result, the Holocene permafrost depth record is subdivided into five distinct periods and related to the SRSF chronology as follows:

- 10 - 8.1 ka – 'stable phase' – low SRSF activity; maximum Holocene permafrost depth.
- 8.1 - 4.8 ka – 'transition phase' – increasing susceptibility to SRSF activity; decreasing permafrost depth.
- 4.8 - 2.6 ka – 'peak phase' – maximum SRSF activity; minimum Holocene permafrost depth.
- 2.6 - 0.6 ka – 'exhaustion phase' – decreasing SRSF activity; little change in shallow permafrost depth.

- 0.6 - 0.1 ka – 'stabilization phase' – minimum SRSF activity; increasing permafrost depth.

(4) Long-term relative change in permafrost depth provides a compelling explanation for the high-magnitude departures from the SRSF background rate. In particular, the gradual change in permafrost depth during the 'transition phase', as opposed to a stochastic response to climate warming, accounts for the significant lag (~2.2 ka) between the Holocene Thermal Maximum and the SRSF frequency peak. Moreover, persistent shallow permafrost during the 'peak phase' may be the key driver behind SRSF occurrence by (a) actively destabilizing bedrock cliffs and causing slope failure and/or (b) weakening bedrock cliffs and making them more susceptible to other trigger factors.

(5) Conversely, declining SRSF frequency during the 'exhaustion phase' appears to reflect the diminished supply of potentially failable cliffs, even under a shallow permafrost depth scenario. Finally, low frequency of SRSF occurrence during the 'stabilization phase' likely reflects an increase in permafrost depth (permafrost aggradation) after ~0.6 ka; a change which would have been sufficient to stabilize slopes and decrease the susceptibility of bedrock cliffs to direct or indirect failure.

(6) This interpretation is supported by geomorphological evidence, given the consistent location of SRSF sites in relation to the local aspect-dependent lower altitudinal limit of permafrost in cliff faces. This new paraperiglacial model attributes enhanced SRSF activity to progressive and intermittent permafrost degradation during Holocene warm periods, including the possibility of renewed aggradation of permafrost during short-term cold periods and renewed degradation during the ensuing warm periods

(7) Our new thermally-driven, permafrost-degradation model of SRSF events in Jotunheimen bears little similarity to existing models of Holocene RSF activity. However, while aspects of this new model require further testing by other methods and in other regions, the results of this study have important implications for climate-change forcing of RSF activity. Projected mean annual global warming is predicted to decrease the area of mountain permafrost and raise lower altitudinal permafrost limits. This in turn will likely destabilize higher bedrock slopes and increase SRSF frequency there. The delayed response of peak SRSF frequency to warming climate, as modulated by permafrost depth, may therefore result in a long-lasting impact of current climate trends on mountain environments.

Acknowledgements – Fieldwork was carried out on the Swansea University Jotunheimen Research Expeditions of 2014-2017. We are grateful to Ole and Tove Grindvold (Leirvassbu) for continuing expedition support; to Atle Nesje and Anne E. Bjune for data and sources of information on uplift rates and climate in southern Norway; and to R.L. Hermanns for a very thorough critical review that led to significant improvement of the manuscript. Anna C. Ratcliffe prepared the figures for publication. This paper constitutes Jotunheimen Research Expeditions, Contribution No. 205 (see http://jotunheimenresearch.wixsite.com/home).

References

Aa, A.R. & Sjåstad, J.A. 2000: Schmidt hammer age evaluation of the moraine sequence in front of Bøyabreen, western Norway. *Norsk Geologiske Tidsskrift 80*, 27-32.

Aa, A.R., Sjåstad, J., Sønstegaard, E. & Blikra, L.H. 2007: Chronology of Holocene rock-avalanche deposits based on Schmidt-hammer relative dating and dust stratigraphy in nearby bog deposits, Vora, inner Nordfjord, Norway. *The Holocene* 17, 955-964.

Ahlmann, H.W. 1922: Glaciers in Jotunheimen and their physiography. *Geografiska Annaler 4*, 1-57.

Allen, S. & Huggel, C. 2013: Extremely warm temperatures as a potential cause of recent high mountain rockfall. *Global and Planetary Change 107*, 59-69.

Allen, S., Cox, S. & Owens, I. 2010: Rock avalanches and other landslides in the central Southern Alps of New Zealand: a regional study considering possible climate change impacts. *Landslides 8*, 33-48.

Alley, R.B. 2004: *GISP2 Ice Core Temperature and Accumulation Data. IGBP PAGES/World Data Center for Paleoclimatology Data Contribution Series #2004-013.* NOAA/NGDC Paleoclimate Program, Boulder, CO.

André, M.F. 1996: Rock weathering rates in Arctic and subarctic environments (Abisko Mts, Swedish Lappland). *Zeitschrift für Geomorphology NF 40*, 499-517.

André, M.F. 2002: Rates of postglacial rock weathering on glacially scoured outcrops (Abisko-Riksgränsen area, 68°N). *Geografiska Annaler Series A Physical Geography 64*, 139-150.

Andreassen, L.M. & Winsvold, H., 2012. *Inventory of Norwegian Glaciers.* Norwegian Water Resources and Energy Directorate (NVE), Oslo.

Antinao, J.L. & Gosse, J. 2009: Large rockslides in the southern central Andes of Chile (32–34°S): tectonic control and significance for Quaternary landscape evolution. *Geomorphology 104*, 117-133.

Arsenault, A.M. & Meigs, A.J. 2005: Contribution of deep-seated bedrock landslides to erosion of a glaciated basin in southern Alaska. *Earth Surface Processes and Landforms 30*, 1111-1125.

Aune, B. 1993: *Temperatur Normaler, Normalperiode 1961–1990.* Den Norske Meterorologiske Institutt, Oslo (Rapport 02/93, in Norwegian).

Bakke, J., Lie, Ø., Dahl, S.O., Nesje, A. & Bjune, A.E. 2008: Strength and spatial patterns of the Holocene wintertime westerlies in the NE Atlantic region. *Global and Planetary Change 60*, 28-41.

Ballantyne, C.K. 2002: Paraglacial geomorphology. *Quaternary Science Reviews 21*, 1035-2017.

Ballantyne, C.K. & Stone, J.O. 2013: Timing and periodicity of paraglacial rock-slope failures in the Scottish Highlands. *Geomorphology 186*, 150-161.

Ballantyne, C.K., Wilson, P., Schnabel, C. & Xu, S. 2013: Lateglacial rock slope failures in north-west Ireland: age, causes and implications. *Journal of Quaternary Science 28*, 789-802.

Ballantyne, C.K., Sandeman, G.F., Stone, J.O. & Wilson, P. 2014a: Rock-slope failure following Late Pleistocene deglaciation on tectonically stable mountainous terrain. *Quaternary Science Reviews 86*: 144-157.

Ballantyne, C.K., Wilson, P., Gheorghiu, D. & Rodés, À. 2014b: Enhanced rock-slope failure following ice-sheet deglaciation: timing and causes. *Earth Surface*

Processes and Landforms 39, 900-913.
Barnett, C., Dumayne-Peaty, L. & Matthews, J.A. 2000: Holocene climatic change and tree-line response in Leirdalen, central Jotunheimen. *Review of Palaeobotany and Palynology 117*, 119-137.
Barr, I.D., Roberson, S., Flood, R. & Dortch, J.M. 2017: Younger Dryas glaciers and climate in the Mourne Mountains, Northern Ireland. *Journal of Quaternary Science 32*, 104-115.
Bates, R.L. & Jackson, J.A. (eds) 1987: *Glossary of Geology, 3rd edition*, 573. American Geological Institute: Alexandria, VA.
Battey, M.H. & McRitchie, W.D. 1973: A geological traverse across the pyroxene-granulites of Jotunheimen in the Norwegian Caledonides. *Norsk Geologiske Tidsskrift 53*, 237-265.
Battey, M.H. & McRitchie, W.D. 1975: The petrology of the pyroxene-granulite facies rocks of Jotunheimen. *Norsk Geologiske Tidsskrift 55*, 1-49.
Benestad, R.E. 2005: Climate change scenarios for northern Europe from multi-modal IPCC AR4 climate simulations. *Geophysical Research Letters 32*, L17704.
Betts, M.W. & Latta, M.A. 2000: Rock surface hardness as an indication of exposure age: an archaeological application of the Schmidt hammer. *Archaeometry 42*, 209-223.
Blikra, L.H. & Christiansen, H.H. 2014: A field-based model of permafrost-controlled rockslide deformation in northern Norway. *Geomorphology 208*, 34-49.
Blikra, L.H., Longva, O., Braathen, A., Anda, E., Dehls, J.F. & Stalsberg, K. 2006: Rock slope failures in Norwegian fjord areas: examples, spatial distribution and temporal patterns. In Evans, S.G., Mugnozza, G.S., Strom, A. and Hermanns, R.L. (eds), *Landslides from Massive Rock Slope Failures*, 475-496. Springer: Dordrecht.
Böhme, M., Oppikofer, T., Longva, O., Jaboyedorff, M, Hermanns, R.L. & Derron, M.-H. 2015. Analyses of past and present rock slope instabilities in a fjord valley: imlications for hazard estimation. *Geomorphology 248*, 464-474.
Bond, G., Kromer, B., Beer, J., Muscheler, R., Evans, M.N., Showers, W., Hoffmann, S., Lotti-Bond, R.,Hajdas, R. & Bonani, G. 2001: Persistent solar influence on North Atlantic climate dring the Holocene. *Science 278*, 1257-1266.
Borgatti, L. & Soldati, M. 2010: Landslides and climatic change. In Alcántara-Ayala, I. & Goudie, A. (eds) *Geomorphological Hazards and Disaster Prevention*, 87-95. Cambridge University Press, Cambridge.
Braathen, A., Blikra, L.H., Berg, S.S. & Karlsen, F. 2004: Rock-slope failures in Norway: type, geometry, deformation mechanisms and stability. *Norwegian Journal of Geology 84*, 67-88.
Brideau, M.-A. & Roberts, N.J. 2015: Mass movement in bedrock. In Davies, T. (ed.) *Landslide Hazards, Risks, and Disasters, 43-90.* Elsevier, Amsterdam.
Briner, J.P., Kaufman, D.S., Manley, W.F., Finkel, R.C., & Caffee, M.W. 2005: Cosmogenic exposure dating of late Pleistocene moraine stabilization in Alaska. *Geological Society of America Bulletin 117*, 1108-1120.
Brunsden, D. & Prior, D.B. (eds) 1984: *Slope Instability*. Wiley, Chichester.
Bungum, H., Lindholm, C.D., Dahle, A., Woo, G., Nadim, F., Holme, J.K., Gudmestad, O.T., Hagberg, T. & Karthisgeyan, K. 2000: New seismic zoning maps for Norway, the North Sea, and the United Kingdom. *Seismological Research Letters 71*, 687-697.
Černá, B. & Engel, Z. 2011: Surface and sub-surface Schmidt hammer rebound value variation for a granite outcrop. *Earth Surface Processes and Landforms 36*,

170-170.
Clague, J.J. & Stead, D. (eds) 2012: *Landslides: Types, Mechanisms and Modeling*, Cambridge University Press: Cambridge.
Collins, B.D. & Stock, G.M. 2016: Rockfall triggering by cyclic thermal stressing of exfoliation fractures. *Nature Geoscience 9*, 395-399.
Colman, S.M. 1981: Rock-weathering rates as functions of time. *Quaternary Research 15*, 250-264.
Colman, S.M. & Dethier, D.P. (eds.) 1986: *Rates of Chemical Weathering of Rocks and Minerals*. Academic Press, Orlando, FL.
Colman, S.M., Pierce, K.L. & Birkeland, P.W. 1987: Suggested terminology for Quaternary dating methods. *Quaternary Research 28*, 314-319.
Cossart, E., Braucher, R., Fort, M., Bourlès, D.L. & Carcaillet, J. 2008: Slope instability in relation to glacial debuttressing in alpine areas (Upper Durance catchment, southeastern France): evidence fromm field data and ^{10}Be cosmic ray exposure ages. *Geomorphology 85*, 3-26.
Cossart, E., Mercier, D., Decaulne, A., Feuillet, T, Jónsson, H.P. & Þorsteinn Sæmundsson 2014: Impacts of post-glacial rebound on landslide spatial distribution at a regional scale in northern Iceland (Skagafjörður). *Earth Surface Processes and Landforms 39*, 336-353.
Crosta, G.B. & Clague, J.J. 2009: Dating, triggering, modelling, and hazard assessment of large landslides. *Geomorphology 103*, 1-4. [Introduction to the Special Issue.]
Crozier, M.J. 2010: Deciphering the effect of climate change on landslide activity: a review. *Geomorphology 124*, 260-267.
Cruden, D.M. & Varnes, D.J. 2009: Landslide types and processes. In: Turner, A.K. & Schuster, R.L. (eds) *Landslides Investigation and Mitigation*. Transportation Research Board, US National Research Council: Washington, DC: Transportation Research Board, US National Research Council, pp. 36-75. [Special Report 247.]
Dahl, S.-O. & Nesje, A. 1996: A new approach to calculating Holocene winter precipitation by combining glacier equilibrium-line altitudes and pine-tree limits: A case study from Hardangerjøkulen, central-southern Norway. *The Holocene 6*, 381-398.
Dahl, S,-O., Nesje, A., Lie, Ø., Fjordheim, K. & Matthews, J.A. 2002: Timing, equilibrium-line altitudes and climatic implications of two early-Holocene glacial re-advances during the Erdalen Event at Jostedalsbreen, western Norway. *The Holocene 12*, 17-25.
Dann, R., Close, M., Flintoft, M., Hector, R., Barlow, H., Thomas, S. & Francis, G. 2009: Characterization and estimation of hydraulic properties in an alluvial gravel vadose zone. *Vadose Zone Journal* 8, 651-663.
Dapples, F., Oswald, D, Raetzo, H., Landelli, T. & Zwahlen, P., 2003: New records of Holocene landslide activity in the Western and Eastern Swiss Alps: implications of climate and vegetation changes. *Eclogae Geologicae Helvetiae 96*, 1-9.
Davies, T. (ed.) 2015: *Landslide Hazards, Risks, and Disasters.* Elsevier, Amsterdam.
Decaulne, A., Cossart, E., Mercier, D., Feuillet, T., Coquin, J. & Jónsson, H. 2016: An early Holocene age for the Vatn landslide (Skagafjörður, central northern Iceland): insights into the role of postglacial landsliding on slope development. *The Holocene 26*, 1304-1318.

Deline, P. & Kirkbride, M.P. 2009: Rock avalanches on a glacier and morainic complex in Haut Val Ferret (Mont Blanc Massif, Italy). *Geomorphology 103*, 80-92.

Deline, P., Gruber, S., Delaloye, R., Fischer, L., Geertseema, M., Giardino, M., Hasler, A., Kirkbride, M., Krautblatter, M., Magnin, F., NcColl, S., Ravanel, L. & Schoeneich, P. 2015: Ice loss and slope stability in high-mountain regions. In Haeberli, W. & Whitman, C. (eds), *Snow and Ice-Related Hazards, Risks and Disasters*, 521-561. Elsevier, Amsterdam.

Dera, Z.A. & Shumwayb, R.H. 1999: Phase onset time estimation at regional distances using the CUSUM algorithm. *Physics of the Earth and Planetary Interiors 113*, 227-246.

Dortch, J.M., Owen, L.A., Haneberg, WC., Caffee, M.W., Dietsch, C. & Kamp, U. 2009: Nature and timing of large landslides in the Himalaya and Transhimalaya of northern India. *Quaternary Science Reviews 28*, 1037-1054.

Dortch, J.M., Owen, L.A. & Caffee, M.W. 2013: Timing and climatic drivers for glaciation across semi-arid western Himalayan-Tibetan orogen. *Quaternary Science Reviews 78*, 188–208.

Draebing, D., Krautblatter, M. & Dikau, R. 2014: Interaction of thermal and mechanical processes in steep permafrost rock walls: a conceptual approach, *Geomorphology 226*, 226-235.

Eberhardt, E., Stead, D. & Coggan, J.S. 2004: Numerical analysis of initiation and progressive failure in natural rocks slopes: the 1991 Randa rockslide. *International Journal of Rock Mechanics and Mining Sciences 41*, 69-87.

Eisbacher, G.H. & Clague, J.J. 1984: Destructive mass movements in high mountains: hazards and management. *Geological Survey of Canada, Paper 84/16*, 1-230.

Eldevik, T., Risebrobakken, B., Bjune, A.E., Andersson, C., Birks, H.J.B., Dokken, T.M., Drange, H., Glessmer, M.S., Li, C., Nilsen, J.E.Ø., Ottera, O.H., Richter, K. & Skagseth, Ø. 2014: A brief history of climate – the northern seas from the Last Glacial Maximum to global warming. *Quaternary Science Reviews 106*, 225-246.

Etzelmüller, B., Berthling, I. & Sollid, J.L. 2003: Aspects and concepts on the geomorphological significance of Holocene permafrost in southern Norway. *Geomorphology 52*, 87-104.

Evans, S.G. & Clague, J.J. 1994: Recent climate change and catastrophic geomorphic processes in mountain environments. *Geomorphology* 10, 107-128.

Evans, S.G., Mugnozza, G.S., Strom, A. & Hermanns, R.L. (eds) 2006: *Landslides from Massive Rock Slope Failures*. Springer, Dordrecht.

Farbrot, H., Hipp, T.F., Etzelmüller, B., Isaksen, K., Ødegård, R.S., Schuler, T.V. & Humlum, O. 2009: Air and ground temperature variations observed along elevation and continentality gradients in southern Norway. *Permafrost and Periglacial Processes 22*, 343–360.

Fischer, L., Kääb, A., Huggel, C. & Noetzli, J. 2006: Geology, glacier retreat and permafrost degradation as controlling factors of slope stability in a high mountain rock wall. *Natural Hazards and Earth System Sciences 6*, 761-772.

Fjeldskaar, W., Lindholm, C., Dehls, J.F. & Fjeldskaar, I. 2000: Postglacial uplift, neotectonics and seismicity in Fennoscandia. *Quaternary Science Reviews 19*, 1413-1422.

Førland, E.J. 1993: *Nedbørnormaler, Normalperiode 1961–1990.* Den Norske Meterorologiske Institutt, Oslo (Rapport 39//93, in Norwegian).

Frattini, P., Crosta G.B. & Agliardi, F. 2012: Rockfall characterization and modeling.

In Clague, J.J. & Stead, D. (eds), *Landslides: Types, Mechanisms and Modeling*, 267-271. Cambridge University Press: Cambridge.

Gibbs, A.D. & Banham, P.H. 1979: *Sygnefjell Berggrunnsgeologisk kart 1518 III*, 1:50,000. Norges Geologiske Undersøkelse, Trondheim.

Ginås, K., Etzelmüller, B., Lussana, C., Hjort, J., Sannel, A.B.K., Isaksen, K., Westermann, S., Kuhry, P., Christiansen, H., Frampton, A. & Åkerman, J. 2017: Permafrost map for Norway, Sweden and Finland. *Permafrost and Periglacial Processes 28*, 359–378.

Gjessing, J. 1967: Norway's paleic surface. *Norsk Geografisk Tidsskrift 21*, 69-132.

Goehring, B.M., Brook, E.J., Linge, H., Raisbeck, G.M. & Yiou, F. 2008: Beryllium-10 exposure ages of erratic boulders in southern Norway and implications for the history of the Fennoscandian Ice Sheet. *Quaternary Science Reviews 27*, 320-336.

Goudarzi, M.A., Cocard, M., Santerre, R. & Woldai, T. 2013: GPS interactive time series analysis software. *GPS Solutions 17*, 595-603.

Gruber, S. & Haeberli, W. 2007: Permafrost in steep bedrock slopes and its temperature-related destabilization following climate change. *Journal of Geophysical Research – Earth Surface 112*, F02S18. DOI: 10.1029/2006JF000547.

Gruber, S., Hoelzle, M. & Haeberli, W. 2004: Permafrost thaw and destabilization of Alpine rock walls in the hot summer of 2003. *Geophysical Research Letters 31*, L13504. doi:10.1029/2004GL020051

Hall, K., Thorn, C.E., Matsuoka, N. & Prick, A. 2002: Weathering in cold regions: some thoughts and perspectives. *Progress in Physical Geography 26*, 577-603.

Hallet, B., & Putknonen, J. 1996: Surface dating of dynamic landforms: young boulders on aging moraines. *Science 26*, 937-940.

Hallet, B., Walder, J.S. & Stubbs, C.W. 1991: Weathering by segregation ice growth in microcracks at sustained sub-zero temperatures: verification from an experimental study using acoustic emissions. *Permafrost and Periglacial Processes* 2, 283-300.

Hermanns, R.L. & Longva, O. 2012: Rapid rock-slope failures. In Clague, J.J. & Stead, D. (eds): *Landslides: Types, Mechanisms and Modeling*, 59-70. Cambridge University Press: Cambridge.

Hermanns, R.L., Trauth, M.H., Niedermann, S., McWilliams, M. & Strecker, M.R. 2000: Tephrochronological constraints on temporal distribution of large landslides in Northwest Argentina. *Journal of Geology 108*, 35-52.

Hermanns, R.L., Niedermann, S., Garcia, A.V., Gomez, J.S. & Strecker, M.R. 2001: Neotectonics and catastrophic failure of mountain fronts in the southern intra-Andean Puna Plateau, Argentina. *Geology 29*, 619-623.

Hermanns, R.L., Niedermann, S., Ivy-Ochs, S. & Kubik, P.W. 2004: Rock avalanching into a landslide-dammed lake causing multiple dam failure in Las Conchas valley (NW Argentina) – evidence from surface exposure dating and stratigraphic analysis. *Landslides 1*, 113-122.

Hermanns, R.L., Blikra, L.H., Naumann, M., Nilsen, B., Panthi, K.K. & Stromeyer, D. 2006: Examples from multiple rock-slope collapses from Köfels (Ötz valley, Austria) and western Norway. *Engineering Geology 83*, 94-108.

Hermanns, R.L., Schleier, M., Böhme, M., Blikra, L.H., Gosse, J., Ivy-Ochs, S. & Hilger, P. 2017: Rock-avalanche activity in W and S Norway peaks after the retreat of the Scandinavian Ice Sheet. In Mikoš, M., Vílímek, V., Yin, Y. & Sassa, K. (eds): *Advancing Culture of Living with Landslides, Volume 5:*

Landslides in Different Environments, 331-338. Springer: Berlin.

Hewitt, K., Clague, J.J. & Orwin, J.F. 2008: Legacies of catastrophic rock slope failures in mountain landscapes. *Earth-Science Reviews 87*, 1-38.

Heyman, J., Stroeven, A.P., Harbor, J.M., & Caffee, M.W. 2011: Too young or too old: Evaluating cosmogenic exposure dating based on an analysis of compiled boulder exposure ages. *Earth and Planetary Science Letters 302*, 71-80.

Hick, E.C., Bungum. H. & Lindholm, C.D. 2000: Seismic activity, inferred crustal stresses and seismotectonics in the Rana region, Northern Norway. *Quaternary Science Reviews 19*, 1423-1436.

Hipp, T., Etzelmüller, B. & Westermann, S. 2014: Permafrost in alpine rock faces from Jotunheimen and Hurrungane, southern Norway. *Permafrost and Periglacial Processes 25*, 1-13.

Holm, K., Bovis, M. & Jakob, M. 2004: The landslide response of alpine basins to post-Little Ice Age glacial thinning and retreat in southwestern British Columbia. *Geomorphology 57*, 201-216.

Hormes, A., Blaauw, Dahl, S.O., Nesje, A. & Possnert, G. 2009: Radiocarbon wiggle-match dating of proglacial lake sediments – implications for the 8.2 ka event. *Quaternary Geochronology 4*, 267-277.

Huggel, C., Salzmann, N., Allen, S., Caplan-Auerbach, J., Fischer, L., Haeberli, W., Larsen, C., Schneider, D. & Wessel, R. 2010: Recent and future warm extreme events and high-mountain slope stability. *Philosophical Transactions of the Royal Society A 368*, 2435-2459.

Huggel, C., Clague, J.J. & Korup, O. 2012: Is climate change responsible for changing landslide activity in high mountains? *Earth Surface Processes and Landforms 37*, 77-91.

Hughes, A.L.C., Gyllencreutz, R., Lohne, Ø., Mangerud, J. & Svendsen, J.L. 2016: The last Eurasian ice sheets – a chronological database and time-slice reconstruction, DATED-1. *Boreas 45*, 1-45.

Hungr, O. & Evans, S.G. 2004: Entrainment of debris in rock avalanches: analysis of a long run-out mechanism. *Geological Society of America Bulletin 116*, 1240-1252.

Isaksen, K., Hauck, C., Gudevang, E., Ødegård, R.S. & Sollid, J.L. 2002: Mountain permafrost distribution in Dovrefjell and Jotunheimen, southern Norway, based on BTS and DC restivity tomography data. *Norsk Geografisk Tidsskrift 56*, 122-136.

Ivy-Ochs, S., Poschinger, A.v., Synal, H. & Maisch, M. 2009: Surface exposure dating of the Flims landslide, Graubünden, Switzerland. *Geomorphology 103*, 104-112.

Jansen, E., Andersson, C., Moros, M., Nisancioglu, K.H., Nyland, B.F. & Telford, R.J. 2008: The early to mid-Holocene thermal optimum in the North Atlantic. In Battarbee, R.W. & Binney, H.A. (eds): *Natural Climate Variability and Global Warming: a Holocene Perspective*, 128-137. Wiley-Blackwell: Chichester.

Jarman, D. 2006: Large rock slope failures in the Highlands of Scotland: characterization, causes and spatial distribution. *Engineering Geology 83*, 161-182.

Johnson, B.G., Smith, J.A. & Diemer, J.A. 2017: A chronology of post-glacial landslides suggests that slight increases in precipitation could trigger a disproportionate geomorphic response. *Earth Surface Processes and Landforms 42*, 2223-2239.

Karlén, W. & Matthews, J.A. 1992: Reconstructing Holocene glacier variations from glacial lake sediments: studies from Nordvestlandet and Jostedalsbreen-Jotunheimen, southern Norway. *Geografiska Annaler Series A Physical Geography 74*, 327-348.

Keefer, D.K. 2002: Investigating landslides caused by earthquakes – a historical review. *Surveys in Geophysics 23*, 473-510.

Keefer, D.K. 2015: Landslides generated by earthquakes: immediate and long-term effects. In Owen, L.A. (ed.) *Tectonic Geomorphology*, 250-266. Elsevier, Amsterdam. [Treatise on Geomorphology, Volume 5]

Korup, O., Clague, J.J., Hermanns, R.L., Hewitt, K., Strom, A.L., & Weidinger, J.T. 2007: Giant landslides, topography, and erosion. *Earth and Planetary Science Letters 261*, 578-589

Krautblatter, M. & Leith, K. 2015: Glacier- and permafrost-related slope instabilities. In Huggel, C., Carey, M., Clague, J.J. & Kääb, A. (eds): *The High-Mountain Cryosphere: Environmental Changes and Human Risks*, 147-165. Cambridge University Press, Cambridge.

Krautblatter, M., Funk, D. & Guenzel, F. 2013: Why permafrost rocks become unstable: a rock-ice-mechanical model in time and space. *Earth Surface Processes and Landforms 38*, 876-887.

Kukkonen, I.T., & Šafanda, J. 2001: Numerical modelling of permafrost in bedrock in northern Fennoscandia during the Holocene. *Global and Planetary Change 29*, 259-273.

Lang, A., Moya, J. Corominas, J., Schrott, L. & Dikau, R. 1999: Classic and new dating methods for assessing the temporal occurrence of mass movements. *Geomorphology 30*, 33-52.

Lau, K.-M., & Weng, H. 1995: Climate signal detection using wavelet transform: How to make a time series sing. *Bulletin of the American Meteorological Society 76*, 2391-2402.

Lidmar-Bergström, K., Ollier, C. & Sulebak, J.R. 2000: Landforms and uplift history of southern Norway. *Global and Planetary Change 24*, 211-231.

Lilleøren, K.S., Etzelmüller, B., Schuler, T.V., Ginås, K. & Humlum, O. 2012: The relative age of permafrost – estimation of Holocene permafrost limits in Norway. *Global and Planetary Change 92–93*, 209–223.

Lu, M., Pebesma, E., Sanchez, A. & Verbesselt, J. 2016: Spatio-temporal change detection from multidimensional arrays: Detecting deforestation from MODIS time series. *ISPRS Journal of Photogrammetry and Remote Sensing 117*, 227-236.

Luckman, B.L. 2004: Rockfall. In Goudie, A.S. (ed.): *Encyclopedia of Geomorphology, Volume 2*, 882. Routledge: London.

Lutro, O. & Tveten, E. 1996: *Geologiske kart over Norge, bergrunnskart Årdal,* 1:250,000. Norges Geologiske Undersøkelse, Trondheim.

Lysså A., Knies, J. & Larsen E. 2008: Kunskap om istider og landformer – nøkkelen til forståelsen av klimavariasjoner. *Gråsteinen 12*, 41-57. [Norges geologiske undersøkelse]

Mangerud, J., Gyllencreutz, R., Lohne, Ø. & Svendsen, J.I. 2011: Glacial history of Norway. In: Ehlers, J., Gibbard, P.L. & Hughes, P.D. (eds): *Quaternary glaciations – extent and chronology: a closer look*, 279-298. Elsevier: Amsterdam.

Marc, O., Hovius, N., Meunier, P., Uchida, T. & Hayashi, S. 2015: Transient changes of landslide rates after earthquakes. *Geology 43*, 883-886.

MATLAB 2015. *MATLAB Version 8.5,* The MathWorks, Inc., Natick MA.

Matsuoka, N. & Murton, J. 2008: Frost weathering: recent advances and future directions. *Permafrost and Periglacial Processes 19*, 195-210.

Matthews, J.A. 1991: The late Neoglacial ('Little Ice Age') glacier maximum in southern Norway: new ^{14}C-dating evidence and climatic implications. *The Holocene 1*, 219-133.

Matthews, J.A. 2005: 'Little Ice Age' glacier variations in Jotunheimen, southern Norway: a study in regionally-controlled lichenometric dating of recessional moraines with implications for climate and lichen growth rates. *The Holocene 15*, 1-19.

Matthews, J.A. & Dresser, P.Q. 2008: Holocene glacier variation chronology of the Smørstabbtindan massif, Jotunheimen, southern Norway, and the recognition of century- to millennial-scale European Neoglacial events. *The Holocene 18*, 181-201.

Matthews, J.A. & McEwen, L.J. 2013: High-precision Schmidt-hammer exposure-age dating (SHD) of flood berms, Vetlestølsdalen, alpine southern Norway: first application and some methodological issues. *Geografiska Annaler Series A Physical Geography* 95, 185-194.

Matthews, J.A. & Owen, G. 2008: Endolithic lichens, rapid biological weathering and Schmiodt hammer R-values on recently exposed rock surfaces: Storbreen glacier foreland, Jotunheimen, Norway. *Geografiska Annaler Series A Physical Geography* 90, 287-297.

Matthews, J.A & Owen, G. 2010: Schmidt-hammer exposure-age dating: developing linear age-calibration curves using Holocene bedrock surfaces from the Jotunheimen–Jostedalsbreen regions of southern Norway. *Boreas 39*, 105-115.

Matthews, J.A. & Owen, G. 2011: Holocene chemical weathering, surface lowering and rock weakening rates on glacially eroded bedrock surfaces in an alpine periglacial environment, Jotunheimen, Norway. *Permafrost and Periglacial Processes 22*, 279-290.

Matthews, J.A. & Shakesby, R.A., 1984: The status of the 'Little Ice Age' in southern Norway: relative-age dating of Neoglacial moraines with Schmidt hammer and lichenometry. *Boreas 13*, 333-346.

Matthews, J.A. & Shakesby, R.A. 2004: A twentieth-century neoparaglacial rock topple on a glacier foreland, Ötztal Alps, Austria. *The Holocene 14*, 454-458.

Matthews, J.A. & Seppålå, M. 2005: Holocene colluvial chronology in the sub-arctic esker landscape at Kuttanen, Finnisj Lapland: kettleholes as geo-ecological archives of interactions amongst fire, vegetation, soil, climate and geomorphological instability. *Boreas 44*, 343-367.

Matthews, J.A. & Vater, A.E. 2015: Pioneer zone geo-ecological change: observations from a chronosequence on the Storbreen glacier foreland, Jotunheimen, southern Norway. *Catena 135*, 219-230.

Matthews, J.A. & Wilson, P. 2015: Improved Schmidt-hammer exposure ages for active and relict pronival ramparts in southern Norway, and their palaeoenvironmental implications. *Geomorphology 246*, 7-21.

Matthews, J.A. & Winkler, S. 2011: Schmidt-hammer exposure-age dating (SHD): application to early Holocene moraines and a reappraisal of the reliability of terrestrial cosmogenic-nuclide dating (TCND) at Austanbotnbreen, Jotunheimen, Norway. *Boreas 40*, 256-270.

Matthews, J.A., Brunsden, D., Frenzel, B., Gläser, B. & Weiss, M.M. (eds) 1997: *Rapid Mass Movement as a Source of Climatic Evidence for the Holocene.* Gustav

Fisher Verlag, Stuttgart, 446 pp. [*Paläoklimaforschung* Volume 19]

Matthews J.A., Berrisford, M.S., Dresser, P.Q., Nesje, A., Dahl, S.O., Bjune, A.E., Bakke, J., Birks, H.J.B., Lie, Ø., Dumayne-Peaty, L. & Barnett, C. 2005: Holocene glacier history of Bjørnbreen and climatic reconstruction in central Jotunheimen, southern Norway, based on proximal glaciofluvial stream-bank mires. *Quaternary Science Reviews 24*, 67-90.

Matthews, J.A., Dahl, S.O., Dresser, P.Q., Berrisford, M.S., Lie, Ø., Nesje, A. & Owen, G. 2009: Radiocarbon chronology of Holocene colluvial (debris-flow) activity at Sletthamn, Jotunheimen, southern Norway: a window on the changing frequency of extreme climatic events and their landscape impact. *The Holocene 19*, 1107-1129.

Matthews, J.A., Nesje, A. & Linge, H. 2013: Relict talus-foot rock glaciers at Øyberget, upper Ottadalen, southern Norway: Schmidt hammer exposure ages and palaeoenvironmental implications. *Permafrost and Periglacial Processes 24*, 336-346.

Matthews, J.A., Winkler, S. & Wilson, P. 2014: Age and origin of ice-cored moraines in Jotunheimen and Breheimen, southern Norway: insights from Schmidt-hammer exposure-age dating. *Geografiska Annaler Series A Physical Geography 96*, 531-548.

Matthews, J.A., McEwen, L.J. & Owen, G. 2015: Schmidt-hammer exposure-age dating (SHD) of snow-avalanche impact ramparts in southern Norway: approaches, results and implications for landform age, dynamics and development. *Earth Surface Processes and Landforms 40*, 1705–1718.

Matthews, J.A., Owen, G., Winkler, S., Vater, A.E., Wilson, P., Mourne, R.W. & Hill, J.L. 2016: A rock-surface microweathering index from Schmidt hammer R-values and its preliminary application to some common rock types in southern Norway. *Catena 143*, 35-44.

Matthews, J.A., Wilson, P. & Mourne, R.W. 2017: Landform transitions from pronival ramparts to moraines and rock glaciers: a case study from the Smørbotn cirque, Romsdalsalpane, southern Norway. *Geografiska Annaler Series A Physical Geography 96*, 15-37.

McCarroll, D. 1987: The Schmidt hammer in geomorphology: five sources of instrument error. *British Geomorphological Research Group Technical Bulletin 36,* 16-27.

McCarroll, D. 1994: The Schmidt hammer as a measure of degree of rock surface weathering and terrain age. In Beck, C. (ed.) *Dating in Exposed and Surface Contexts*, 29-45. University of New Mexico Press, Albuquerque.

McColl, S.T. 2012: Paraglacial rock-slope stability. *Geomorphology 153-154*, 1-16.

McColl, S.T. & Davies T.R.H. 2012: Large ice-contact slope movements, glacial buttressing, deformation and erosion. *Earth Surface Processes and Landforms 38*, 1102-1115.

McPhillips, D., Bierman, P.R. & Rood, D.H. 2014: Millennial-scale record of landslides in the Andes consistent with earthquake trigger. *Nature Geoscience 7*, 925-930.

Mercier, D. 2008: Paraglacial and paraperiglacial land systems: concepts, temporal scales and spatial distribution. *Géomorphologie: Relief, Processus, Environnement 14*, 223-233.

Mercier, D., Coquin, J., Feuillet, T., Decaulne, A., Cossart, E., PallJónsson, H. & Sæmundsson, Þ. 2017: Are Icelandic rock-slope failures paraglacial? Age evaluation of seventeen rock-slope failures in the Skagafjörður area based on

geomorphological stacking, radiocarbon dating and tephrochronology. *Geomorphology 296*, 45-58.

Messenzehl, K. & Dikau, R. 2017: Structural and thermal controls of rockfall frequency and magnitude within rockwall-talus systems (Swiss Alps). *Earth Surface Processes and Landforms 42*, 1963-1981.

Moen, A. 1999: *National Atlas of Norway: Vegetation*. Norwegian Mapping Authority, Hønefoss.

Moreiras, S.M., Hermanns, R.L. & Fauqué, L. 2015: Cosmogenic dating of rock avalanches constraining Quaternary stratigraphy and regional neotectonics in the Argentine Central Andes (32°S). *Quaternary Science Reviews 112*, 45-58.

Moses, C., Robinson, D. & Barlow, J. 2014: Methods for measuring rock surface weathering and erosion: a critical review. *Earth-Science Reviews 135*, 141-161.

Murari, M.K., Owen, L.A., Dortch, J.M., Caffee, M.W., Dietsch, C., Fuchs, M., Haneberg, W.C., Sharma, M.C. & Townsend-Small, A. 2014: Timing and climatic drivers for glaciation across monsoon-influenced regions of the Himalayan-Tibetan orogen. *Quaternary Science Reviews 88*, 159-182.

Murphy, B. 2015: Coseismic landslides. In Davies, T. (ed.) *Landslide Hazards, Risks, and Disasters,* 91-129. Elsevier, Amsterdam.

Murton, J. B., Peterson & Ozouf, J.-C. 2006: Bedrock fracture in cold regions. *Science 314*, 1127-1129.

Nesje, A. 2009: Late Pleistocene and Holocene alpine glacier fluctuations in Scandinavia. *Quaternary Science Reviews 28*, 2119-2136.

Nesje, A. & Dahl, S.O. 2001: The Greenland 8200 cal. yr BP event detected in loss-on-ignition profiles in Norwegian lacustrine sediment sequences. *Journal of Quaternary Science 16*, 155-166.

Nesje, A., Bakke, J., Dahl, S.O., Lie, Ø. & Matthews, J.A. 2008: Norwegian glaciers in the past, present and future. *Global and Planetary Change 60*, 10-27.

Nesje, A., Blikra, L. & Anda, E. 1994: Dating rockfall-avalanche deposits from degree of rock-surface weathering by Schmidt-hammer tests: a study from Norangsdalen, Sunnmøre, Norway. *Norsk Geologiske Tidsskrift 74,* 108-113.

Nicholson, D.T. 2008: Rock control inmicroweathering of bedrock surfaces in a periglacial environment. *Geomorphology 101*, 655-665.

Nicholson, D.T. 2009: Holocene microweathering rates and processes on ice-eroded bedrock, Røldal area, Hardangervidda, southern Norway. In: Knight, J. & Harrison, S. (eds.): *Periglacial and Paraglacial Processes and Environments*, 29-49. Geological Society, Special Publication 320. Geological Society of London, Bath.

Ødgård, R.S., Sollid, J.L. & Liestøl, O. 1992: Ground temperature measurements in mountain permafrost, Jotunheimen, southern Norway. *Permafrost and Periglacial Processes 3*, 231-234.

Ødgård, R.S., Nesje, A., Isaksen, K., Andreassen, L.M., Eiken, T., Scwikowski, M. & Uglietti, C. 2017: Climate change threatens archaeologically significant ice patches: insights into their age, internal structure, mass balance and climate sensitivity. *The Cryosphere 11*, 17-32.

Oerlemans, J. 2005: Extracting a climate signal from 169 glacier records. *Science 308*, 675-677.

Olesen,O., Dehls, J., Bugum, H., Riis, F., Hicks, E., Lindholm, C., Blikra, L.H., Fjeldskaar, W., Olsen, L., Longva, O., Faleide, J.I., Bockmann, L., Rise, L.,

Roberts, D., Braathen, A. & Brekke, H. 2000: *NEONOR: Neotectonics in Norway, Final Report.* Norges Geologiske Undersøkelse, Trondheim. [Report 2000.002]

Owen, G., Hiemstra, J.F., Matthews, J.A. and McEwen, L.J. 2010: Landslide-glacier interaction in a neoparaglacial setting at Tverrbytnede, Jotunheimen, southern Norway. *Geografiska Annaler Series A Physical Geography 92*, 421-436.

Pánek, T. 2014: Recent progress in landslide dating: a global overview. *Progress in Physical Geography 39*, 168-198.

Paus, A. & Haugland, V. 2017: Early- to mid-Holocene forest-line and climate dynamics in southern Scandes mountains inferred from contrasting megafossil and pollen data. *The Holocene 27*, 361-383.

Penna, I.M., Hermanns, R.L., Niedermann, S & Folguera, A. 2011: Multiple slope failures associated with neotectonic activity in the Southern Central Andes (37°-37° 30'S), Patagonia, Argentina. *Geological Society of America Bulletin 123*, 1880-1895.

Phillips, M., Wolter, A., Lüthi, R., Amann, F., Kenner, R. & Bühler, Y. 2017: Rock slope failure in a recently deglaciated permafrost rock wall at Piz Kesch (Eastern Swiss Alps), February 2014. *Earth Surface Processes and Landforms 42*, 426-438.

Prager, C., Zangerl, C., Patzelt, G. & Brandner, R. 2008: Age distribution of fossil landslides in the Tyrol (Austria) and its surrounding areas. *Natural Hazards and Earth System Sciences 8*, 377-407.

Prager, C., Ivy-Ochs, S., Ostermann, M., Synal, H.-A. & Patzelt, G. 2009: Geology and radiometric ^{14}C-, ^{36}Cl- and Th/U-dating of the Fernpass rockslide (Tyrol, Austria). *Geomorphology 103*, 93-103.

Proceq 2004: *Operating instructions. Betonprüfhammer N/NR-L/LR.* Proceq SA: Schwerzenbach.

Rapp, A. 1960a: Talus slopes and mountain walls at Templefjorden, Spitzbergen. *Norsk Polarinstitutt Skrifter 119*, 1-96.

Rapp, A. 1960b: Recent development of mountain slopes in Kärkevagge and surroundings, northern Scandinavia. *Geografiska Annaler 42*, 65-200.

Reimer, P.J., Bard, E., Bayliss, A., Beck, J.W., Blackwell, P.G., Ramsey, C.B., Buck, C.E., Cheng, H., Edwards, R.L., Friedrich, M. & Grootes, P.M. 2013: IntCal13 and Marine13 radiocarbon age calibration curves 0–50,000 years cal BP. *Radiocarbon 55*, 1869-1887.

Renssen, H., Seppä, H., Crosta, X., Goose, H. & Roche, D.M. 2012: Global characterization of the Holocene Thermal Maximum. *Quaternary Science Reviews 48*, 7-19.

Sánchez, S.J., Mosquera, D.F & Vidal Romaní, J.R. 2009: Assessing the age-weathering correspondence of cosmogenic ^{21}Ne dated Pleistocene surfaces by the Schmidt hammer. *Earth Surface Processes and Landforms 34*, 1121-1125.

Sandøy, G., Oppikofer, T. & Nilsen, B. 2017: Why did the 1756 Tjellefonna rockslide occur? A back-analysis of the largest historic rockslide in Norway. *Geomorphology 289*, 78-95.

Sass, O. & Wollny, K. 2001: Investigations regarding alpine talus slopes using ground-penetrating radar (GPR) in the Bavarian Alps, Germay. *Earth Surface Processes and Landforms 26*, 1071-1086.

Scarpozza, C. 2016: Evidence of paraglacial and paraperiglacial crisis in Alpine sediment transfer since the last glaciation (Tincino, Switzerland). *Quaternaire 27*, 139-155.

Schleier, M., Hermanns, R.L., Rohn, J. & Gosse J.C. 2015: Diagnostic characteristics and paleodynamics of supraglacial rock avalanches, Innerdalen, Western Norway. *Geomorphology 245*, 23-39.

Schleier, M., Hermanns, R.L., Goose, J.C., Oppikofer, T., Rohn, J. & Tønnesen, J.F. 2017: Subaqueous rock-avalanche deposits exposed by post-glacial isostatic rebound, Innfjorddalen, Western Norway. *Geomorphology 289*, 117-133.

Seppä, H., Bjune, A.E., Telford, R.J., Birks, H.J.B. Birks & Veski, S. 2009: Last nine-thousand years of temperature variability in Northern Europe. *Climate Past 5*, 523-535.

Shakesby, R.A. 2014: Rockfall. In Matthews, J.A., Barrow, C.J., Boyd, D.S., Caseldine, C.J., Ficken, K.J., Innes, J.L., Nortcliff, S., Owen, G., Pike, J., Shakesby, R.A., Walsh, R.P.D. & Wheeler, D.A. (eds): *Encyclopedia of Environmental Change, Volume 3*, 939-940. SAGE, London.

Shakesby, R.A., Matthews, J.A. & Owen, G. 2006: The Schmidt hammer as a relative-age dating tool and its potential for calibrated-age dating in Holocene glaciated environments. *Quaternary Science Reviews 25*, 2846-2867.

Shakesby, R.A., Matthews, J.A., Karlén, W. & Los, S. 2011: The Schmidt hammer as a Holocene calibrated-age dating technique: testing the form of the R-value–age relationship and defining predicted errors. *The Holocene 21*, 615-628.

Soldati, M., Corsini, A. & Pasuto, A. 2004: Landslides and climate change in the Italian Dolomites since the Late Glacial. *Catena 55*, 141-161.

Stahl, T., Winkler, S., Quigley, M., Bebbington, M., Duffy, B. & Duke, D. 2013: Schmidt hammer exposure-age dating (SHD) of late Quaternary fluvial terraces in New Zealand. *Earth Surface Processes and Landforms 38*, 1838-1850.

Stock, G.M. & Uhrhammer, R.A. 2010: Catastrophic rock avalanche 3600 BP from El Capitan, Yosemite Valley, California. *Earth Surface Processes and Landforms 35*, 941-951.

Stoffel, M. & Huggel, C. 2012: Effects of climate change on mass movements in mountain environments. *Progress in Physical Geography 36*, 421-439.

StormTech 2012: *Tech Sheet 1: porosity of structural backfill.* [http://www.stormtech.com/download_files/pdf/techsheet1.pdf]

Stroeven, A.P., Hättestrand, C., Kleman, J., Heyman, J., Fabel, D., Fredin, O., Goodfellow, B.W., Harbor, J.M., Jansen, J.D., Olsen, L., Caffee, M.W., Fink, D., Lundqvist, J., Rosqvist, G.C., Strömberg, B. & Jansson, K.N. 2016: Deglaciation of Fennoscandia. *Quaternary Science Reviews 147*, 91-121.

Tomkins, M.D., Dortch, J.M., & Hughes, P.D. 2016: Schmidt Hammer exposure dating (SHED): Establishment and implications for the retreat of the last British Ice Sheet. *Quaternary Geochronology 33*, 46-60.

Tomkins, M.D., Huck, J.J., Dorch, J.M., Hughes, P.D., Kirkbride, M.P. & Barr, I.D. 2018a: Schmidt hammer exposure dating (SHED): calibration procedures, new exposure age data and an online calculator. *Quaternary Geochronology 44*, 55-62.

Tomkins, M.D., Dortch, J.M., Hughes, P.D., Huck, J.J., Stimson, A.G., Delmas, M., Calvet, M. & Pallàs, R. 2018b: Schmidt hammer exposure dating (SHED): rapid age assessment of glacial landforms in the Pyrenees. *Quaternary Research* (in press).

Tomkins, M.D., Dortch, J.M., Hughes, P.D., Huck, J.J., Tonkin, T., & Barr, I.D. 2018c: Timing of glacial retreat in the Wicklow Mountains, Ireland,

conditioned by glacier size and topography. *Journal of Quaternary Science* (in press).

Torrence, C., & Compo, G.P. 1998: A Practical Guide to Wavelet Analysis. *Bulletin of the American Meteorological Society 79*, 61-78

Trauth. M.H., Alonso, R.A., Haselton, K.R., Hermanns, R.L. & Strecker, M.R. 2000: Climate change and mass movements in the NW Argentine Andes. *Earth and Planetary Science Letters 179*, 243-256.

Trauth, M.H., Bookhagen, B., Marwan, N. & Strecker, M.R. 2003. Multiple landslide clusters record Quaternary climate changes in the northwestern Argentine Andes. *Palaeogeography, Palaeoclimatology, Palaeoecology 194*, 109-121.

Väliranta, M., Salonen, J.S., Heikkilä, M., Amon, L., Helmens, K., Klimaschewski, A., Kuhry, P., Kultti, S., Paska, A., Shala, S., Veski, S. & Birks, H.H. 2015: Plant macrofossil evidence for an early onset of the Holocene summer thermal maximum in northernmost Europe. *Nature Comunications* doi:10.1038/ncomms7809.

Velle, G., Bjune, A.E., Larsen, J & Birks, H.J.B. 2010: Holocene climate and environmental history of Brurskardstjørni, a lake in the catchment of Øvre Heimdalsvatnet, south-central Norway. *Hydrobiologia 642*, 13–34.

Viles, H., Goudie, A., Grabb, S. & Lalley, J. 2011: The use of the Schmidt hammer and Equotip for rock hardness assessment in geomorphology and heritage science: a comparative analysis. *Earth Surface Processes and Landforms 36*, 320-333.

Walker, M.J.C., Berkelhammer, M., Björk, S., Cwynar, L.C., Fisher, D.A., Long, A.J., Lowe, J.J., Newnham, R.M., Rasmussen, S.O. & Weiss, H. 2012: Formal subdivision of the Holocene Series/Epoch: a discussion paper by a Working Group of INTIMATE (Integration of ice-core, marine and terrestrial records) and the Subcommission on Quaternary Stratigraphy (International Commission on Stratigraphy). *Journal of Quaternary Science 27*, 649-659.

Wanner, H., Solomina, O., Grosjean, M., Ritz, S. & Jetel, M. 2011: Structure and origin of Holocene cold events. *Quaternary Science Reviews 30*, 3109-3123.

Wilson, P. 2009: Storurdi: a late Holocene rock-slope failure (Sturzstrom) in the Jotunheimen, southern Norway. *Geografiska Annaler Series A Physical Geography 91*, 47-58.

Wilson, P. & Matthews, J.A. 2016: Age assessment and implications of late Quaternary periglacial and paraglacial landforms on Muckish Mountain, northwest Ireland, based on Schmidt-hammer exposure-age dating (SHD). *Geomorphology 270*, 134-144.

Wilson, P., Matthews, J.A. & Mourne, R.W. 2017: Relict blockstreams at Insteheia, Valldalen-Tafjorden, southern Norway: their nature and Schmidt-hammer exposure age. *Permafrost and Periglacial Processes 28*: 286-297.

Winkler, S. 2009: First attempt to combine terrestrial cosmogenic nuclide (^{10}Be) and Schmidt hammer relative-age dating: Strauchon Glacier, Southern Alps, New Zealand. *Central European Journal of Geosciences 1*, 274-290.

Winkler, S. & Matthews, J.A. 2010: Holocene glacial chronologies: are 'high resolution' global and interhemispherical comparisons possible? *The Holocene 20*, 1137-1147.

Winkler, S. & Matthews, J.A. 2014: Comparison of electronic and mechanical Schmidt hammers in the context of exposure-age dating: are Q- and R-values interconvertible? *Earth Surface Processes and Landforms 39*, 1128-1136.

Winkler S. & Matthews, J.A. 2016: Inappropriate instrument calibration for Schmidt-

hammer exposure-age dating (SHD) – A comment on Dorch et al., Quaternary Geochronology 35 (2016), 67-68. *Quaternary Geochronology 36*, 102-103.

Winkler, S., Chinn, T., Gärtner-Roer, I., Nussbaumer, U., Zemp, M. & Zumbühl, H.J. 2010: An introduction to mountain glaciers as climatic indicators with spatial and temporal diversity. *Erdkunde 64*, 97-118.

Winkler, S., Matthews, J.A., Mourne, R.W. & Wilson, P. 2016: Schmidt-hammer exposure ages from periglacial patterned ground (sorted circles) in Jotunheimen, Norway, and their interpretive problems. *Geografiska Annaler Series A Physical Geography 98*, 265-285.

Zerathe, S., Lebourg, T., Braucher, R. & Bourlès, D. 2014: Mid-Holocene cluster of large-scale landslides revealed in the Southwestern Alps by ^{36}Cl dating. Insight on an Alpine-scale landslide activity. *Quaternary Science Reviews 90*, 106-127.

FIGURE CAPTIONS

Fig. 1. Location map: numbers and open circles identify the studied SRSFs; sites of control points are shown by crosses.

Fig. 2. Photographs of selected small rock-slope failures (SRSFs): (A) No. 23, Gravdalen; (B) Nos 7 and 8, Leirdalen; (C) Nos 34-36, Bjørndalen; (D) No. 7, Sognefjell; (E) and (F) No. 22, Gravdalen (also the site of a young control point).

Fig. 3. Schematic of the fan-scar-cliff comparison tests with expected differences in mean R-values between fan boulders, scar bedrock surfaces, unfailed cliffs, and rock surfaces used as younger and older control-point surfaces. Expectations apply to single-event SRSF events without the possible complications discussed in the text.

Fig. 4. Frequency distributions of four SRSF characteristics: (A) fan volume; (B) altitude; (C) aspect; (D) mean R-value. Eight sites in gabbroic gneiss (Sognefjell) are differentiated by solid black shading from 84 sites in pyroxene-granulite gneiss.

Fig. 5. Calibration curves and calibration equations for (A) pyroxene-granulite gneiss and (B) gabbroic gneiss. Note that both calibration curves are based on two control points of known age (25 years and 9700 years) using data presented in Table 3.

Fig. 6. Holocene SHD chronologies of SRSF activity for Jotunheimen: (A) individual SHD dates with their 95% confidence intervals in the different subregions; (B) age-frequency distributions of SRSF events at the regional level using 2000-yr, 1000-yr, 500-yr and 200-yr time intervals; (C) weighted age-frequency distribution with age-frequency curve defined by binomial smoothing; (D) variation in the magnitude of SRSF events based on rock volume using 200-year time intervals. Vertical bands (numbered) are the 4 modes in the weighted age-frequency distribution suggesting phases of enhanced regional SRSF activity.

Fig. 7. Probability density function analysis of SRSF activity for Jotunheimen: (A) histogram and KS density PDE; (B) individual Gaussian age distributions (n = 5), the sum of which integrates to the cumulative PDE with a model fit that is graphically indistinguishable from from the PDE model. The number of ages listed for each Gaussian age distribution (#) exceeds the total number of SRSF events identified in Jotunheimen as some ages contribute to >1 Gaussian distribution; (C) peak Gaussian numerical ages and 1σ uncertainties for the five individual Gaussian age distributions plotted against the peak probability density (PPD). The PPD scales with the number and spatial clustering of individual ages. Reported RSF volumes are based on the sum of individual SRSF volumes (m^3) which comprise each Gaussian age distribution; (D) distribution of SRSF ages, sorted by oldest to youngest. The 42 SRSF events which account for the dominant mode at 4.50 ± 1.42 ka (within 1σ) are highlighted.

Fig. 8. Change detection and related analyses: (A) Cumulative sum change detection graph showing positive (blue) and negative (orange) changes and statistically significant departures (> 2σ) from the background SRSF frequency; (B) modelled permafrost depth in Fennoscandia (5% porosity) from Kukkonen & Šafanda (2001), subdivided into five distinct phases; (C) results of discreet Meyer wavelet analysis, showing the lowest frequency decomposed signal (d_6).

Fig. 9. Models for different patterns and causes of Holocene variations in RSF frequency and/or magnitude: (1) continuity-of-activity; (2) intermittent-earthquakes; (3) deglaciation-close-tracking; (4) deglaciation-lagging; (5) cool/wet-climate-response; and (6) the new thermally-driven permafrost-degradation model proposed in this study for SRSFs in Jotunheimen. The subdivisions of the Holocene shown are those proposed by Walker et al. (2012).

Fig. 10. Relationships between SRSF frequency in Jotunheimen and proxy climatic records: (A) temporal variations in SRSF frequency from Fig. 6C; (B) pollen-based reconstruction of annual air temperature for Northern Europe expressed as deviations from the mean (Seppä et al., 2009); (C) mean summer air temperature deviations from present in the Scandes Mountains based on pine tree-limit variations (Dahl and Nesje, 1996); (D) pollen-based July air temperature variations at Øvre Heimdalsvatnet, eastern Jotunheimen (Velle et al., 2010); (E) periods of above average air temperature (shaded) based on the GISP 2 Greenland ice core $\delta^{18}O$ record (Alley, 2004; Wanner et al., 2011); (F) periods of above average sea-surface temperatures in the North Atlantic Ocean (shaded) based on standardized stacked ice-rafted debris (IRD) records (Bond et al., 2001; Wanner, et al., 2011); (G) periods when glaciers in the Smørstabbtindan massif, Jotunheimen, were smaller than today (shaded) based on glaciolacustrine and glaciofluvial stratigraphy (Matthews and Dresser, 2008). Vertical bands indicate phases of enhanced regional SRSF frequency (as in Fig. 6).

SUPPLEMENTARY MATERIAL

(Caption to be included with figure)

Supplementary Fig.1: Full results of discreet Meyer wavelet analysis, showing all six decomposed signals (green), ranging from high (d_1) to low frequency (d_6), of which the latter represents the only single event structure of Holocene SRSF activity. The blue curves (a_1 - a_5) represent the cumulative aggregation of the decomposed signals (d_1 - d_6) where a_6 represents the mean background rate of SRSF occurrence (0.92 ± 0.20), which is identical to the Holocene mathematical mean. The sum of all decomposed signals results in a model (S_m) that is identical to the 100 yr bin histogram data (S_d).

Table 1. Data on the 92 small rock-slope failures (SRSFs) located in Jotunheimen: Leirdalen (Nos 1-29); Bjørndalen (30-40); Gravdalen (41-68); Høgvaglura (69-72); Visdalen (73-80); Veodalen (81-84); Sognefjell (85-92).
Abbreviations: L = fan length; W = fan width; V = fan volume; SD = standard deviation of R-values; C_s = error associated with the dated surface; C_c = error associated with the calibration equation; CI = confidence interval for the SHD age based on the total error (C_t).

No.	L (m)	W (m)	V (m^3)	Altitude (m a.s.l.)	Aspect	Mean R-value	SD	C_s (yr)	C_c (yr)	SHD age (yr ± 95% CI)	Sub-region
1	70	25	1050	1420	West	45.0	9.90	1047	513	7018 ± 1124	Leirdalen
2	80	20	960	1440	West	44.51	8.80	930	414	7277 ± 1018	
3	15	9	81	1400	West	39.69	9.47	1001	458	9833 ± 1101	
4	90	40	2160	1160	West	41.53	9.57	1012	445	8857 ± 1105	
5	15	8	72	1030	West	43.26	10.03	1060	426	7940 ± 1143	
6	90	20	1080	1160	West	43.62	10.23	1081	423	7749 ± 1161	
7	8	25	120	1140	West	44.69	9.41	995	412	7182 ± 1077	
8	30	25	450	1140	West	46.59	10.35	1094	392	6175 ± 1162	
9	8	8	38	1135	West	47.28	8.63	912	385	5809 ± 990	
10	15	25	225	1135	West	44.68	8.85	936	412	7187 ± 1022	
11	30	20	360	1200	North	52.38	10.07	1064	333	3105 ± 1115	
12	50	25	750	1425	North	46.49	8.63	912	394	6228 ± 994	
13	15	25	225	960	East	51.50	8.34	882	342	3572 ± 946	
14	50	25	750	955	East	49.79	10.74	1135	360	4478 ± 1191	
15	70	60	2520	950	East	49.28	8.73	923	365	4749 ± 992	
16	50	25	750	1290	West	48.29	9.98	1055	375	5273 ± 1120	
17	20	40	480	1320	West	54.10	9.90	1047	315	2193 ± 1093	
18	20	15	180	1320	West	57.53	10.15	1073	280	375 ± 1109	
19	30	40	720	1320	West	55.95	8.61	910	296	1213 ± 957	
20	18	14	151	1120	East	48.79	8.43	891	370	5008 ± 965	
21	16	8	77	1120	East	44.40	8.29	876	415	7336 ± 970	
22	25	14	210	1130	East	48.93	9.11	963	368	4934 ± 1031	
23	40	13	312	1170	East	41.30	9.14	966	447	8979 ± 1065	
24	25	15	225	1180	East	40.82	9.16	968	296	9233 ± 1012	
25	15	13	117	1180	East	43.37	9.49	1003	426	7882 ± 1090	
26	20	4	48	1190	East	44.86	8.70	920	410	7092 ± 1007	
27	12	8	58	1240	East	49.28	10.53	1113	365	4749 ± 1171	
28	20	4	48	1240	East	45.92	10.98	1160	399	6530 ± 1227	
29	22	4	53	1200	East	47.15	8.24	871	387	5878 ± 953	
30	90	16	864	1370	East	44.27	10.65	1126	416	7405 ± 1200	Bjørndalen
31	30	15	270	1380	East	44.62	10.10	1068	413	7219 ± 1145	
32	30	10	180	1380	East	52.60	8.62	911	331	2989 ± 922	
33	75	30	1350	1360	East	54.91	8.30	877	307	1764 ± 930	
34	30	15	270	1380	East	49.87	7.53	796	359	4436 ± 873	
35	30	12	216	1380	East	49.46	7.84	829	363	4653 ± 905	
36	20	30	360	1380	East	50.19	8.61	910	355	4266 ± 977	
37	80	35	1680	1330	South	50.23	9.57	960	355	4245 ± 1024	
38	25	15	225	1300	North	54.07	6.73	711	316	2209 ± 778	
39	50	30	900	1305	North	55.37	7.95	840	302	1520 ± 893	
40	25	25	375	1300	North	53.30	8.20	867	323	2617 ± 925	
41	55	20	660	1480	West	49.43	8.11	857	363	4669 ± 931	Gravdalen
42	15	35	315	1480	West	55.49	6.69	707	301	1456 ± 769	
43	65	15	585	1480	West	51.11	8.40	888	346	3778 ± 953	
44	60	15	540	1470	West	50.84	7.05	745	349	3922 ± 823	
45	65	25	975	1470	West	50.01	8.85	936	357	4362 ± 1001	
46	30	15	270	1460	West	52.57	7.97	843	331	3004 ± 905	
47	75	20	900	1460	West	53.03	6.27	663	326	2761 ± 739	
48	25	30	450	1430	South	50.01	7.00	740	357	4362 ± 822	
49	17	8	82	1440	South	49.10	8.45	893	367	4844 ± 964	
50	40	15	360	1440	South	49.71	7.72	816	360	4521 ± 892	
51	15	10	90	1440	South	50.38	7.78	822	356	4165 ± 896	
52	15	6	54	1400	South	56.21	7.38	780	293	1075 ± 834	
53	10	5	30	1400	South	57.99	6.22	658	275	131 ± 713	
54	7	8	34	1360	South	47.32	8.00	846	385	5788 ± 929	
55	10	6	36	1280	South	40.31	10.14	1072	457	9504 ± 1165	
56	12	5	36	1440	South	48.82	8.12	858	370	4992 ± 935	
57	6	5	18	1440	South	47.43	7.72	816	384	5729 ± 902	
58	8	8	38	1440	South	51.63	7.70	814	341	3503 ± 882	
59	4	5	12	1440	South	51.12	6.62	700	346	3773 ± 781	
60	7	4	17	1480	South	48.02	7.43	785	378	5416 ± 872	

61	20	5	60	1480	South	52.10	11.98	1266	336	3254 ± 1310	
62	14	8	67	1480	South	46.17	9.02	953	399	6397 ± 1033	
63	6	12	43	1430	South	48.74	8.09	855	370	5035 ± 932	
64	10	5	30	1430	South	46.99	7.65	809	388	5963 ± 897	
65	14	3	25	1460	South	49.91	8.38	886	358	4415 ± 956	
66	15	4	36	1520	South	51.92	8.34	882	338	3349 ± 944	
67	6	4	14	1540	South	49.95	9.74	1030	358	4393 ± 1090	
68	10	5	30	1540	South	49.37	7.08	748	364	4701 ± 832	
69	20	15	180	1550	East	50.13	7.74	818	356	4298 ± 892	Høgvaglura
70	50	12	360	1550	East	45.16	10.05	1062	407	6933 ± 1138	
71	20	10	120	1540	East	46.35	8.94	945	395	6302 ± 1024	
72	20	10	120	1540	East	42.10	11.92	1260	439	8555 ± 1334	
73	15	4	36	1420	East	47.03	11.08	1171	388	5941 ± 1234	Visdalen
74	15	9	81	1420	East	50.70	10.47	1107	350	3996 ± 1161	
75	10	4	24	1420	East	54.42	9.47	1001	312	2024 ± 1049	
76	25	10	150	1260	West	49.96	10.20	1078	358	4388 ± 1136	
77	40	20	480	1200	East	51.37	10.30	1089	343	3641 ± 1142	
78	70	30	1260	1200	East	52.98	8.86	937	327	2787 ± 992	
79	35	20	420	1200	East	51.57	7.93	838	341	3535 ± 905	
80	60	8	288	1190	East	50.31	10.75	1136	354	4202 ± 1190	
81	55	40	1320	1350	South	53.33	8.72	922	323	2601 ± 977	Veodalen
82	45	12	324	1340	South	54.33	9.34	987	313	2071 ± 1036	
83	50	25	750	1330	South	51.56	10.15	1073	341	3540 ± 1126	
84	45	40	1080	1330	South	49.46	10.60	1121	363	4653 ± 1178	
85	6	10	36	1375	East	37.17	11.29	900	239	9412 ± 931	Sognefjell
86	7	5	21	1425	South	38.53	8.82	703	244	8868 ± 744	
87	6	6	22	1425	South	39.42	10.43	831	247	8513 ± 868	
88	10	5	30	1430	South	41.38	9.86	786	255	7729 ± 826	
89	6	5	18	1430	South	40.73	9.47	755	253	7989 ± 796	
90	16	10	96	1450	South	38.26	8.83	704	243	8976 ± 745	
91	9	5	27	1435	West	42.33	10.03	800	259	7349 ± 840	
92	10	7	42	1370	East	36.95	9.14	729	238	9500 ± 766	

Table 2. Radiocarbon age control for deglaciation in the study area.

Location	Altitude (m. a.s.l.)	^{14}C age ± 1σ (years BP)	Calibrated age* (cal. years BP)	Reference
Leirdalen/Bjørndalen				
Lower Leirdalen	920	9089 ± 61	10426 – 10170 (94.8%)	Barnett et al. 2000
Bøverkinnhalsen	1020	8570 ± 60	9677 – 9475 (95.4%)	Nesje & Dahl 2001
Bjørndalen	1250	8760 ± 100	10066 – 9547 (77.1%)	Matthews et al. 2005
Sognefjell				
Nedre Hervavatnet	1287	8695 ± 75	9921 – 9530 (94.6%)	Hormes et al. 2009
Gjuvvatnet	1248	8885 ± 140	10247 – 9557 (95.4%)	Karlén & Matthews 1992

* Most probable range with probability in brackets

Table 3. Control point data: values used for calibration equations are indicated in bold. *Abbreviations:* Gneiss = pyroxene-granulite gneiss; Gabbro = gabbroic gneiss; Combined = data combined from two replicate sites; SD = standard deviation; CI = confidence interval; n = sample size.

Control point	Geology	Type	Age (years)	Mean R-value	SD	95% CI	n
Gravdalen	Gneiss	SRSF	25	58.22	6.29	0.72	300
Gravdalen	Gneiss	Road cut	25	58.15	6.56	0.75	300
Gravdalen	**Gneiss**	**Combined**	**25**	**58.19**	**6.42**	**0.52**	**600**
Sognefjell	**Gabbro**	**Road cut**	**25**	**60.65**	**7.26**	**0.83**	**300**
Gravdalen	Gneiss	Bedrock	9700	39.71	4.80	1.25	60
Leirdalen	Gneiss	Bedrock	9700	40.19	4.69	1.22	60
SE Smørstabbtindan	**Gneiss**	**Combined**	**9700**	**39.94**	**4.79**	**0.87**	**120**
Leirbreen	Gabbro	Bedrock	9700	35.78	2.84	0.74	60
Bøverbreen	Gabbro	Bedrock	9700	37.12	3.53	0.92	60
W Smørstabbtindan	**Gabbro**	**Combined**	**9700**	**36.45**	**3.25**	**0.59**	**120**

Table 4. Comparative R-values from fans, scars and unfailed cliffs associated with selected SRSFs. Further information on these six SRSFs are provided in Table 1.

No.	Fan	Scar	Unfailed cliff

	Mean	SD	95% CI	Mean	SD	95% CI	Mean	SD	95% CI
5	43.26	10.03	2.00	41.34	7.75	1.55	42.20	7.86	1.57
46	51.63	7.70	1.54	51.32#	8.10	1.62	41.63†	9.20	1.83
47	51.12	6.62	1.32	54.05#	8.05	1.69	43.26†	10.19	2.03
51	37.17*	11.29	2.25	42.89	9.73	1.94	38.54	10.37	2.07
58	36.95*	9.14	1.82	43.99	10.44	2.08	40.68	12.30	2.45
81	49.96*	10.20	2.03	54.47#	8.07	1.60	43.38†	10.78	2.15

* Fan significantly different from scar ($p<0.05$)
# Scar significantly different from unfailed cliff ($p<0.05$)
† Unfailed cliff significantly different from fan ($p<0.05$)

Small rock-slope failures conditioned by Holocene permafrost degradation: a new approach and conceptual model based on Schmidt-hammer exposure-age dating, Jotunheimen, southern Norway

JOHN A. MATTHEWS[1*], STEFAN WINKLER[2], PETER WILSON[3], MATT D. TOMKINS[4], JASON M. DORTCH[5], RICHARD W. MOURNE[6], JENNIFER L. HILL[6], GERAINT OWEN[1] AND AMBER E. VATER[1]

[1] *Department of Geography, College of Science, Swansea University, Singleton Park, Swansea SA2 8PP, Wales, UK*
[2] *Department of Geography and Geology, Julius-Maximilians-University Würzburg, Am Hubland, 97070 Würzburg, Germany*
[3] *School of Geography and Environmental Sciences, Ulster University, Cromore Road, Coleraine BT52 1SA, Northern Ireland, UK*
[4] *Cryosphere Research at Manchester, Department of Geography, University of Manchester, Manchester M13 9PL, UK*
[5] *Kentucky Geological Survey, 228 Mining and Mineral Resources Building, University of Kentucky, Lexington, Kentucky 40506, USA*
[6] *Department of Geography and Environmental Management, University of the West of England, Coldharbour Lane, Bristol BS16 1QY, UK*

* corresponding author: J.A.Matthews@Swansea.ac.uk

Rock-slope failures (RSFs) constitute significant natural hazards but the geophysical processes which control their timing are poorly understood. However, robust chronologies can provide valuable information on the environmental controls on RSF occurrence: information which can inform models of RSF activity in response to climatic forcing. This paper uses Schmidt-hammer exposure-age dating (SHD) of boulder deposits to construct a detailed regional Holocene chronology of the frequency and magnitude of small rock-slope failures (SRSFs) in Jotunheimen, Norway. By focusing on the depositional fans of SRSFs ($\leq 10^3$ m^3), rather than on the corresponding features of massive RSFs (~10^8 m^3), 92 single-event RSFs are targeted for chronology building. A weighted SHD age-frequency distribution and probability density function analysis indicate four centennial- to millennial-scale periods of enhanced SRSF frequency, with a dominant mode at ~4.5 ka. Using change detection and discreet Meyer wavelet analysis, in combination with existing permafrost depth models, we propose that enhanced SRSF activity was primarily controlled by permafrost degradation. Long-term relative change in permafrost depth provides a compelling explanation for the high-magnitude departures from the SRSF background rate and accounts for (1) the timing of peak SRSF frequency, (2) the significant lag (~2.2 ka) between the Holocene Thermal Maximum and the SRSF frequency peak and (3) the marked decline in frequency in the late-Holocene. This interpretation is supported by geomorphological evidence, as the spatial distribution of SRSFs is strongly correlated with the aspect-dependent lower altitudinal limit of mountain permafrost in cliff faces. Results are indicative of a causal relationship between episodes of relatively warm climate, permafrost degradation and the transition to a seasonal-freezing climatic regime. This study highlights permafrost degradation as a conditioning factor for cliff collapse, and hence the importance of paraperiglacial processes; a result with implications for slope instability in glacial and periglacial environments under global warming scenarios.

Key words: small rock-slope failures (SRSFs), Schmidt-hammer exposure-age dating (SHD), permafrost degradation, Holocene Thermal Maximum, climate-change impacts, paraperiglacial processes, southern Norway

Rock-slope failures (RSFs) are indicative of instability in the landscape and reflect several geophysical processes and potential trigger factors related to rock mechanics, geomorphology, hydrology and environmental change. Moreover, RSFs constitute significant natural hazards. As a result, understanding the environmental controls on RSF occurrence provides crucial information which can inform modelling of future RSF activity in response to climate forcing (Rapp 1960a, 1960b; Brunsden & Prior 1984; Evans et al. 2006; Clague & Stead 2012; Davies 2015).

Numerous RSFs have been investigated in regions of high relief and, in some cases, RSF deposits have been dated (e.g. Korup et al. 2007; Ballantyne et al. 2014a, 2014b). However, previous research has primarily focused on modern examples, spectacular cases or small numbers of massive rock-slope failures (MRSFs; ~10^8 m^3) which, in combination with uncertainty associated with current geochronological approaches, limits our understanding of the fundamental geophysical processes and environmental controls that determine RSF occurrence. Particular studies of RSFs have used a variety of techniques and, on some occasions, a combination of geochronological methods (Lang et al. 1999; Hermanns et al. 2000; Crosta & Clague 2009; Deline & Kirkbride 2009; Prager et al. 2009; Pánek 2014; Böhme et al. 2015; Moreiras et al. 2015; Mercier et al. 2017), but the opportunities for accurate dating are relatively rare.

The primary method for numerical-age dating of RSF deposits is terrestrial cosmogenic nuclide dating (TCND; ^{10}Be, ^{26}Al, ^{36}Cl) as this technique permits direct sampling and age determination of the exposed rock surfaces associated with RSFs (Hermanns et al. 2001, 2004, 2017; Cossart et al. 2008; Dortch et al. 2009; Ivy-Ochs et al. 2009; Penna et al. 2011; Ballantyne & Stone 2013; Ballantyne et al. 2013, 2014a, 2014b; Böhme et al. 2015; Schleier et al. 2015, 2017). However, the high financial cost of this technique limits its routine application which, in turn, often prevents statistically robust identification and rejection of erroneous results (Tomkins et al. 2018b). Consequently, there are still few reliable chronologies of RSFs which limits our understanding of the environmental factors determining their spatial and temporal occurrence.

In this paper we develop a methodology for the investigation and dating of RSFs, with targeted study of 'small rock-slope failures' (SRSFs; < 10^3 m^3). This focus has the advantage over MRSFs of permitting the dating and study of a relatively large sample of simple, likely single-event RSFs within a specified region. The methodology has been developed in conjunction with the relatively new calibrated-age dating technique of Schmidt-hammer exposure-age dating (SHD) (Shakesby et al. 2006, 2011; Matthews & Owen 2011; Matthews et al. 2015; Matthews & Wilson 2015; Winkler et al. 2010, 2016; Wilson et al. 2017). SHD has the potential to estimate the numerical age of rock-surface exposure at low cost with comparable accuracy and precision, and greater representativeness, than TCND over the Late

Glacial and Holocene (cf. Winkler 2009; Winkler & Matthews 2010; Matthews & Winkler 2011; Matthews et al. 2013; Wilson & Matthews 2016; Tomkins et al. 2016, 2018a, 2018b, 2018c).

Specific objectives of this paper are three-fold:

- To establish a Holocene chronology of SRSF events in the alpine zone of Jotunheimen, southern Norway and identify any phases of instability;
- To explore relationships between the timing of Holocene SRSF events and regional environmental changes, including climatic changes; and
- To develop further the potential of SHD as a calibrated-age dating technique in the context of RSFs.

Study area and environmental context

SRSFs were investigated in a broad area of northern Jotunheimen, the highest mountain massif in southern Norway, which culminates in Galdhøpiggen (2469 m above sea level; a.s.l.). The study area extends from Sognefjell in the west to Veodalen in the east (Fig. 1). Most SRSFs were found in Leirdalen, Bjørndalen (a western tributary valley to upper Leirdalen) and Gravdalen. The SRSFs occurred over an altitudinal range of 600 m (950-1550 m a.s.l.), mainly above the tree line, which lies at ~1000-1100 m a.s.l., in the alpine zone, and mainly in the low- and mid-alpine belts (Moen 1999). Examples of SRSFs from the study area are shown in Fig. 2.

Climatic data from the Sognefjell meteorological station (1413 m a.s.l.) indicate a mean annual air temperature of +3.1 ºC (mean July temperature +13.4 ºC; mean January temperature –10.7 ºC), and a mean annual precipitation of 860 mm, much of which occurs as snow (climatic normals AD 1961-1990; Aune 1993; Førland 1993). These data are consistent with a lower altitudinal limit of discontinuous permafrost at ~ 1450 m a.s.l. in the Galdhøpiggen massif (Ødgård et al. 1992; Isaksen et al. 2002; Farbrot et al. 2009; Lilleøren et al. 2012) with permafrost limits rising eastwards as continentality increases (Etzelmüller et al. 2003; Ginås et al. 2017). However, Hipp et al. (2014) have demonstrated a large difference of several hundred metres in the lower limits of permafrost between north- and south-facing rock walls. In the Galdhøpiggen massif, the lower altitudinal limit of rock-wall permafrost is located at 1500-1700 m a.s.l. in south-facing rock walls but only 1200-1300 m a.s.l. in shaded, north-facing rock walls (Hipp et al. 2014). Small valley glaciers, cirque glaciers and ice caps are common at and above these altitudes on the surrounding mountain peaks and plateaux (Andreassen & Winsvold 2012).

The metamorphic geology of the region consists primarily of pyroxene-granulite gneiss with peridotite intrusions and quartzitic veins (Battey & McRitchie 1973, 1975; Lutro & Tveten 1996), and gabbroic gneiss in the area investigated on Sognefjell (Gibbs & Banham 1979). Only boulders and bedrock of pyroxene-granulite gneiss and gabbroic gneiss were used in this study, as described below. Although these broad lithological categories include quite variable mineralogy, any differences in surface R-values due to lithology will likely be significantly smaller than the effect of variable exposure age given the relatively long Holocene timescales of exposure and limited climatic variability within the study region.

Topographically, most of the valley-side slopes have experienced a considerable degree of glacial erosion, although elements of ancient palaeic surfaces are preserved in the landscape (Ahlmann 1922; Gjessing 1967; Lidmar-Bergström et al. 2000) due, at least in part, to non-erosive, cold-based conditions during glaciations.

Jotunheimen was located near the position of the main ice-divide and ice-accumulation area of the Scandinavian ice-sheet at the maximum of the Last (Weichselian) Glaciation. Deglaciation of the main valleys is likely to have occurred by ~9.7 ka, following the Erdalen Event, late in the Preboreal chronozone (Dahl et al. 2002; Matthews & Dresser 2008; Velle et al. 2010). Most glaciers appear to have melted away during the Holocene Thermal Maximum (Nesje 2009) when permafrost limits were also higher than today (Lilleøren et al. 2012), but regenerated during neoglaciation, certainly by 5.5 ka and possibly as early as 7.6 ka (Ødgård et al. 2017). Both neoglaciation and lowering of permafrost limits occurred as a result of climatic deterioration (cooler and wetter) in the late Holocene, culminating in the Little Ice Age glacier maximum of the eighteenth century (Matthews 1991, 2005; Matthews & Dresser 2008). Future predicted mean annual warming of 0.3-0.4 ºC per decade in Scandinavia (Benestad 2005) is likely to lead to unprecedented glacier retreat (Nesje et al. 2008) and a continuing rise in permafrost limits (Lilleøren et al. 2012).

Methodology

Definitions and criteria for recognition of SRSFs

The term 'rock-slope failure' (RSF) refers to both (1) a mass-movement process involving the deformation and loss of integrity of a volume of intact bedrock followed by its *en masse* collapse and downslope movement under gravity and (2) the resulting landform. This definition is used here to distinguish RSF from 'rockfall' – the smaller-scale process involving the piecemeal detachment and free fall of individual rock particles – even though the term rockfall is commonly used at all scales, including the largest landslides and rock avalanches (MRSFs), which are often complex and multiphase (cf. Bates & Jackson 1987; Cruden & Varnes 1996; Braathen et al. 2004; Luckman 2004; Evans et al. 2006; Hermanns et al. 2006; Jarman 2006; Frattini et al. 2012; Hermanns & Longva 2012; Shakesby 2014; Brideau & Roberts 2015).

Fundamental to this study was the selection of SRSF landforms that represented, as far as it was possible to ascertain, the product of single events. Criteria for recognition of such SRSFs were as follows:

- a compact and coherent depositional fan of predominantly angular boulders located close to a bedrock cliff.
- a simple erosional scar in the cliff, immediately upslope of the fan, which is comparable in scale to the fan and therefore represents the likely source of the failed rock material;
- an absence of alternative sources of boulders up-slope of the scar.

Although no upper limit was placed on the size of the SRSFs recognized in this study, these criteria become less easily satisfied as RSFs increase in size. The lower size limit was the practical one of sufficient boulders for reliable Schmidt hammer measurement. Thus, the size range included in the study was determined by the RSFs in the region. Furthermore, the 92 investigated cases represent the whole population of SRSFs that satisfied the above criteria in the study area.

Measurement of SRSF characteristics

Estimates were made in the field of the length and average width of the depositional fan of each SRSF. Aspect and the altitude of the fan apex were estimated from topographic maps at a scale of 1:50,000 with a contour interval of 20 m, supplemented by altimeter and GPS measurements in the field. Fan volume was calculated from the length and average width measurements, assuming an average fan thickness of 1 m and a voids fraction (volume of voids/total fan volume) of 40%. Although some of the largest fans are thicker than 1 m in places, all are thinly spread across and down slope and rarely involve piles of debris. Lower voids fractions have generally been used for MRSFs, rock avalanches, talus and other mass movement types involving mixed particle sizes, fine matrix and/or compacted material (Owen et al. 2010; Sass & Wollny 2001; Hungr & Evans 2004; Wilson 2009; Stock & Uhrhammer 2010; Sandøy et al. 2017). The value of 40% is justified given the absence of fine matrix (Fig. 2) and lack of compaction, and its compatibility with similar values for clean, open-graded, angular aggregate material used as backfill in foundation engineering (StormTech 2012; cf. Dann et al. 2009).

Measurement of Schmidt-hammer R-values

N-type mechanical Schmidt hammers (Proceq 2004; Winkler & Matthews 2014) were used to measure rebound (R-) values from 100 boulders in each depositional fan. R-values reflect lithologically-determined rock hardness and the compressive strength of the rock surface: hence, R-values decline following exposure of a rock surface to subaerial weathering. For boulder surfaces of the same lithology but differing age, R-values therefore reflect the exposure age (time elapsed since exposure) of the rock surface. Use of one impact per boulder from a large sample of boulders ensures that the R-value frequency distribution can be used to approximate the boulder-age distribution (Matthews et al. 2014, 2015).

Precautions taken to eliminate or reduce possible sources of uncertainties and errors in Schmidt-hammer measurement included avoiding unstable or small boulders, boulder or bedrock edges, joints or cracks, unusual lithologies and lichen-covered or wet surfaces (cf. Shakesby et al. 2006; Matthews & Owen 2010; Viles et al. 2011). Rock surfaces were not cleaned or artificially abraded prior to impact with the Schmidt hammer (cf. the carborundum treatment of Viles et al. 2011) because such treatment would likely remove age-related weathering effects. However, there is continued debate as to whether rock surfaces should be abraded prior to testing (Moses et al. 2014) although a consistent sampling approach may enable age-related information to be retained (c.f. Tomkins et al. 2018b).Where possible, horizontal boulder surfaces were impacted but only vertical rock faces were available on cliffs. The two hammers used had been recently re-calibrated at a recognised service centre and were tested frequently on the manufacturer's test anvil throughout the study to

ensure there had been no deterioration in instrument performance following large numbers of impacts (cf. McCarroll 1987, 1994; Winkler & Matthews 2016). Measurements at 84 sites were restricted to rock surfaces of pyroxene-granulite gneiss. At the 8 sites on Sognefjell, gneissic rocks with gabbroic textures were used, which necessitated a separate calibration equation (see below).

Testing the validity of the approach

In order to test the validity of our approach, and especially whether the boulders comprising the depositional fans actually represent single rock-failure events and whether the local source of the boulders had been correctly identified, R-value distributions associated with six fans and their corresponding scars were investigated. Two separate tests of validity were conducted.

First, in the *fan-scar comparison test,* a comparable sample of R-values (n = 100) from the surface of the corresponding scar was compared with the R-value distribution of the fan to identify whether or not the scar was the likely source of the boulders in the fan. If the scar was indeed the source of the boulders, the expectation would be no significant difference in the R-values derived from the scar and its corresponding fan because both would have experienced exposure over the same period of time.

Second, the *unfailed-cliff test* required a comparable sample of R-values (n = 100) from the adjacent intact (unfailed) bedrock cliff and also aimed to establish that the cliff was the bedrock source for the fan boulders. If this was the case, it would be expected that R-values from the unfailed cliff would be similar to or lower than the R-values of both the scar and the fan. Any departure from these expectations would indicate possible flaws in our approach.

The principles behind the fan-scar comparison test and the unfailed-cliff test are illustrated in Fig. 3, which also shows the expected relationships between R-values from the fans and R-values from the rock surfaces used as control points in the calibration equations.

Calibrated-age dating using SHD

Although there was earlier use of the Schmidt hammer for dating purposes (e.g. Matthews & Shakesby 1984; Nesje et al. 1994; Aa & Sjåstad 2000; Aa et al. 2007), SHD has been developed more recently as a calibrated-age dating technique (Colman et al., 1987) incorporating measures of uncertainty based on statistical confidence intervals (cf. Shakesby et al. 2006; Matthews & Owen 2011; Matthews & Winkler 2011; Matthews & McEwen 2013). Critically, this involves the derivation of a calibration equation and confidence limits for age.

The calibration equation is based on linear regression of surface age (Y) on mean R-value (X):

$$Y = a + bX \quad (1)$$

A linear relationship can be justified on both theoretical and empirical grounds. Although chemical weathering rates are likely to decline over longer timescales (Colman 1981; Colman & Dethier 1986; Stahl et al. 2013; Tomkins et al. 2018a, 2018b), near-linear rates can be expected over the Holocene timescale, especially where relatively resistant lithologies are subject to relatively slow rates of chemical weathering in a periglacial environment (André 1996, 2002; Nicholson 2008, 2009; Matthews & Owen 2011; Matthews et al. 2016). Although physical (freeze-thaw) weathering is well known in periglacial environments, it is highly dependent on moisture availability for ice-lens growth (Hallet et al. 1991; Hall et al. 2002; Murton et al. 2006; Matsuoka & Murton 2008) and there is no evidence that it has affected the well-drained surfaces used in this study (neither boulders in the dated depositional fans nor bedrock control surfaces).

Furthermore, Shakesby et al. (2011) specifically tested the linearity assumption in relation to granite boulders on independently-dated staircases of raised beaches deposited since 10.4 ka in northern Sweden, with the conclusion that the relationship between mean R-value and age was best described by a linear function. The same conclusion can be reached from age-calibration curves in the British Isles (Tomkins et al. 2018a) and the Pyrenees (Tomkins et al. 2018b), which are based on 54 and 52 ^{10}Be TCND-dated granitic surfaces respectively, all associated with glacial depositional or erosional landforms (moraine boulders or ice-sculpted bedrock). While the Pyrenean age-calibration curve is clearly non-linear over the full age range of ~50 ka, both age-calibration curves evidence linearity over the last ~20 ka. Other studies that have suggested non-linear relationships have involved long timescales and/or have had insufficient control points to test the linearity assumption rigorously over the Holocene timescale (e.g. Betts & Latta 2000; Sánchez et al. 2009; Černá & Engel 2011; Stahl et al. 2013).

Based on two control points, the b coefficient can be defined as:

$$b = (y_1 - y_2) / (x_1 - x_2) \quad (2)$$

where x_1 and x_2 are the mean R-values of the older and younger control points, respectively, and y_1 and y_2 are their respective ages. Once the b coefficient is known, the a coefficient is found by substitution in equation (1). Only two control points of widely differing age are available from Jotunheimen (see below). Provided they are of good quality, however, two control points are sufficient for accurate R-value calibration provided the underlying relationship between R-value and age is approximately linear.

For a landform produced by a single event, the SHD age resulting from this calibration is the average age of the surface boulders and hence the landform age (Matthews et al. 2015). Confidence intervals for the SHD age (95%) are calculated as the total error (C_t) by combining the error associated with the calibration equation (C_c) with the sampling error associated with the surface to be dated (C_s):

$$C_t = \sqrt{(C_c^2 + C_s^2)} \quad (3)$$

$$C_c = C_o - [(C_o - C_y)(R_s - R_o) / (R_y - R_o)] \quad (4)$$

$$C_s = b[ts / \sqrt{(n-1)}] \quad (5)$$

where C_o and C_y are the 95% confidence intervals of the older and younger control points (in years); and R_o, R_y and R_s are the mean R-values of the older control point, the younger control point and the surface to be dated, respectively. C_s depends on the number of R-value impacts on the surface to be dated (sample size, n), the standard deviation of those impacts (s), and Student's t statistic. Thus, the confidence interval (C_t) associated with any SHD age depends not only on the sample sizes used to establish the calibration equation and characterize the surface to be dated but also the natural variability exhibited by all the rock surfaces involved.

Control points for calibration equations

For this study, we constructed separate calibration equations for rock surfaces composed of pyroxene-granulite gneiss and gabbroic gneiss (each equation based on two control points). Data for the older control points, which relate to glacially-scoured bedrock surfaces, were taken from Matthews & Owen (2010). Their data from four sites in Leirdalen and Gravdalen (S and E Smørstabbtindan) were used for the pyroxene-granulite gneiss calibration equation: four sites near Leirbreen and Bøverbreen, close to Sognefjell (W Smørstabbtindan) supplied the data for the gabbroic gneiss calibration equation (Fig. 1).

Evidence for deglaciation of these sites is provided by basal ^{14}C dates from peat bogs and lakes in Leirdalen, Bjørndalen, and on Sognefjell (Table 2). These ^{14}C dates were recalibrated to calendar age ranges with the OxCal online program (v.4.3) using the IntCal13 calibration dataset (Reimer et al. 2013). Although one of the calibrated age ranges is significantly older, 9.7 ka is the only date for deglaciation that is compatible with the other four ^{14}C dates. Use of 9.7 ka as the age of the old control points for SHD calibration can be justified on the further grounds that it is the expected date for termination of the Erdalen Event in neighbouring regions (Dahl et al. 2002) and is consistent with empirical evidence for and large-scale modeling of deglaciation in southern Norway (Dahl et al. 2002; Goehring et al. 2008; Nesje 2009; Mangerud et al. 2011; Hughes et al. 2016; Stroeven et al. 2016). Thus, the potential errors in the old control points appear to be small in relation to the calibration errors (C_c and C_s) that are taken fully into account in this study.

Calibration equations given in Matthews & Owen (2010) for these rock types could not be used because their younger control points were derived from glacially-abraded surfaces from glacier forelands. Such smooth surfaces are not appropriate as a source of young control points for dating the exposure-age of boulders originating from SRSFs, which are rougher in texture yielding lower R-values than abraded surfaces of the same age (Shakesby et al. 2006; Matthews & McEwen 2013; Matthews et al. 2015). In contrast, after prolonged weathering, originally smooth surfaces are expected to yield similar R-values, and hence SHD ages, to initially rough surfaces.

Young control points with similar roughness properties to fresh boulder surfaces derived from SRSFs were therefore sought. These included: (1) boulders and bedrock surfaces produced by a recent rock-slope failure in Gravdalen and (2) bedrock exposed recently in road cuts in Gravdalen and on Sognefjell (Fig. 1). Both types of surfaces have been shown in previous studies to yield R-values that are

statistically indistinguishable from each other provided sufficient care is taken to impact only truly fresh rock surfaces (Matthews & Wilson 2015; Matthews et al. 2016). Furthermore, both types of recent rock surfaces used as young control points in this study were lichen-free and hence were assigned a maximum exposure age of 25 years based on various estimates of the time required for the establishment (ecesis) of crustose lichens on bedrock surfaces in this environment (Matthews 2005; Matthews & Owen 2008; Matthews & Vater 2015). Errors in the age of the young control point are therefore considered to be negligible in the context of this study.

Chronology construction and analysis

Holocene chronologies of SRSF events were constructed from the SHD ages of the 92 SRSF fans using a number of statistical approaches. First, graphical analysis of age-frequency distributions used 2000-yr, 1000-yr, 500-yr and 200-yr time intervals to define major clusters of SHD ages and hence possible multi-centennial to millennial phases of enhanced SRSF frequency (Matthews et al. 2009; Matthews & Seppälä 2015). Based on the same events weighted according to their rock volume, a second chronology was constructed showing the changing magnitude of SRSF events through the Holocene.

In order to take account of dating uncertainty, a weighted age-frequency distribution was constructed in which each SHD age was plotted over five 200-yr age classes: a weight of 4 was used for the central class; the second and fourth classes were weighted 2. Thus, the SHD age was plotted over a range of 1000 yr, consistent with the average 95% confidence interval of ± 991 yr calculated for the 92 SRSF fans (see below). One-sample χ^2 tests were used to test the hypothesis that the dated events were sampled from an underlying population of events with an even distribution through time.

To support weighted age-frequency analysis, the distribution of calculated SRSF ages was analysed using probability density function analysis. Probability density estimates (PDEs) were produced and modelled to separate out individual Gaussian distributions using the KS density kernel in MATLAB (2015) and a dynamic smoothing window based on age uncertainty (cf. Dortch et al. 2013). The sum of individual Gaussian distributions integrates to the cumulative PDE at 1000 iterations to obtain a good model fit. The goodness of fit between the re-integrated PDE, which is derived from individual Gaussian distributions, and the cumulative PDE, which is derived from the full age dataset, is indicated graphically. PDE analysis was repeated using a number of individual Gaussian distributions (n = 1-10). To avoid over-interpretation of SRSF modes, the PDE model with the minimum number of individual Gaussian distributions, which also achieved a good model fit, was selected. This analytical method has primarily been employed in studies using ^{10}Be (cf. Dortch et al. 2013; Murari et al. 2014) or SHD (Barr et al. 2017; Tomkins et al. 2018a; 2018b; 2018c) to account for negative or positive skew of moraine boulder datasets and to identify and reject ages that are compromised by moraine degradation (Briner et al. 2005; Heyman et al. 2011) or nuclide inheritance (Hallet & Putknonen 1996). In these applications, PDE analysis and interpretation of individual Gaussian distributions (cf. Fig. 3 in Dortch et al. 2013) is based on the assumption that analysed ages relate to a single event e.g. moraine deposition. This assumption is clearly not applicable to the analysis of SRSF ages, as each numerical age relates to a distinct

event and an individual landform. As a result, individual Gaussian distributions are interpreted as reflecting the temporal clustering of events. The characteristics of individual Gaussian distributions, i.e. the peak probability density, width of PDE tails, 1σ uncertainties and the number of contributing ages (Fig. 7), were used to assess the significance and temporal clustering of SRSF events in Jotunheimen over the last ~10 ka.

The individual distributions resulting from the PDE analysis indicated that further analysis was necessary. Thus, a change detection analysis approach was undertaken in MATLAB (2015) to identify statistically unique events. Change detection analysis utilizes the cumulative sum algorithm (cusum), which is commonly used to detect abrupt change in time series data in fields ranging from seismology (Dera & Shumwayb 1999), remote sensed imagery (Lu et al. 2016), and GPS monitoring (Goudarzi et al. 2013). Parameters were set by using the average frequency and occurrence (~1 occurrence per 100 years) of SRSFs throughout the Holocene to filter out 'background' SRSF occurrence. The alarm limit was set at ≥2 standard errors above background. To further explore the temporal pattern of SRSFs, discreet Meyer wavelet analysis was undertaken in MATLAB (2015) to decompose SRSF occurrence through time. Wavelets are discreet oscillations in both time and amplitude and, as such, are useful for identifying discreet events. Wavelet analysis has been used to identify climate signals from various records including δO^{18} (Lau & Weng 1995), and sea surface temperature (Torrence & Compo 1998). The 100 yr binned SRSF age data was passed though the discreet Meyer wavelet with six levels of deconvolution.

Major and minor changes in SRSF activity were then compared with changes in regional Holocene climatic and other geo-environmental indicators to infer possible causes. Specific analyses were performed to investigate relationships between the occurrence of SRSF events and the lower altitudinal limits of discontinuous permafrost using aspect-dependent limits determined for rock walls in the Galdhøpiggen massif by Hipp et al. (2014). The current (AD 2010-2013) lower limits that were used for rock walls facing north, east, south and west were 1250 m, 1450 m, 1600 m and 1450 m, respectively.

Results

Data on the SRSFs

Data on the size and environmental characteristics of the SRSFs are summarized in Table 1 and Fig. 4. The volume of the fans (Fig. 4A) ranges from 12 to 2520 m^3, with 90% <1000 m^3, 40% <100 m^3 and a median size of only 180 m^3. The altitudinal range is 960 to 1550 m a.s.l. (Fig. 4B), with a mean altitude of 1340 m a.s.l. There is a preferred aspect with 43% facing east, 34% facing south and 17% facing west, but only 5% facing north (Fig. 4C).

Schmidt-hammer R-values vary widely between SRSFs (Table 1) and the frequency distribution of mean R-values reveals several important features (Fig. 4D). Mean R-values exhibit a very wide range of >20 units from 37.0 to 57.5. The overall mean R-value across the 92 SRSFs is 48.2 but those R-values associated with

gabbroic gneiss (overall mean R-value 39.4, n = 8) are appreciably lower than the remainder involving pyroxene-granulite gneiss (overall mean R-value 49.1, n = 84). The latter value corresponds closely with the 49-50 modal class for the distribution.

Control-point data and calibration equations

Data from the control points (Table 3) indicate widely different mean R-values (differing by at least 20 units) for surfaces that differ in age by ~9700 years. It should also be noted that the overlapping 95% confidence intervals associated with each pair of replicates for particular control points indicate that their mean R-values do not differ significantly from each other. Control surfaces of the same age on different lithologies are, however, characterized by non-overlapping confidence intervals, and thus show significantly different mean R-values and justify the use of separate calibration equations for SRSFs developed in pyroxene-granulite gneiss and gabbroic gneiss. The calibration equations derived from these data for the two lithologies are shown in Figure 5 alongside the linear relationships they represent.

Fan-scar-cliff comparison tests

Mean R-values for three of the six fans tested did not differ significantly from the mean R-values of the corresponding scars, in accordance with expectation (Fig. 3 and Table 4). However, three fans (Nos 51, 58 and 81) are characterized by mean R-values that are significantly lower than the mean R-values from their scars. This suggests one or more of four possible explanations: (1) rock surfaces of some boulders in these fans are more weathered because they include the products of older rock failures than those that produced the measured bedrock faces of the scars; (2) some of the measured R-values from boulders in the fans reflect the incorporation of bedrock surfaces that were pre-weathered on the cliff face before the failures occurred; (3) some of the R-values from boulders in the fans reflect the incorporation of inherited structures (e.g. joint planes) that were pre-weathered at depth before the failures occurred; and (4) at least part of the cliff bedrock is more resistant to weathering than the boulder surfaces measured in the fans. Interestingly, no fan exhibits a mean R-value that is significantly greater than that of its corresponding scar. This shows that even where more than one phase of activity seems possible, any blocks that were later removed from the scars were insufficient in number to affect appreciably the mean R-values of the fans.

Comparisons between scars and unfailed cliffs or between fans and unfailed cliffs are entirely in agreement with expectation. In three cases (fan Nos 5, 51 and 58) neither the mean R-values for scars and unfailed cliffs nor the mean R-values for fans and unfailed cliffs differ significantly, suggesting that all the exposed surfaces are of the same age (and relatively old). In the other three cases (fan Nos 46, 47 and 81) the mean R-values of the scars and the fans are both significantly higher than the mean R-values of the unfailed cliffs, confirming the SRSFs are younger than the exposure age of the unfailed cliffs.

Comparison of the mean R-values from unfailed cliffs with the values from the older control points given in Table 3 indicates that unfailed cliff surfaces were exposed during or immediately after deglaciation at ~9700 cal. BP. As all surfaces yielded mean R-values lower than those characteristic of the younger control points

(Table 4), it appears that fan deposition and scar exposure occurred throughout the Holocene and, in some cases, thousands of years after regional deglaciation. As a result, the temporal distribution of fan mean-R-values likely reflects the timing of single-event SRSF activity.

Temporal variations in SRSF activity

The age of each SRSF event, including its 95% confidence interval, is summarized graphically in Fig. 6A. Although there is some evidence of differences in the age distributions between the different valleys, there is no statistically significant correlation between SRSF age and altitude and no significant difference in age between aspects. The overall mean age of all 92 SRSF events is 5124 years, which equates with an average regional frequency of 1 in 105 years.

Simple age-frequency distributions of the SRSF events within the region as a whole are shown in Fig. 6B. Although these events occurred without any prolonged break in activity, their frequency varied considerably over the last ~10,000 years. The distribution based on 2000-yr time intervals has a single mode indicating an increase in the frequency of events through the early Holocene, a distinct peak in activity in the 6.0-4.0 ka time interval, and a consistent decline in activity thereafter. The use of 1000-year time intervals reveals two modes – at 8.0-7.0 and 5.0-4.0 ka, respectively. At least three modes can be recognized when 500-yr time intervals are used (at 9.0-8.5, 7.5-7.0 and 4.5-4.0 ka) and many more can possibly be discerned in the distribution based on 200-year time intervals. However, analysis of SRSF modes based on 200-year time intervals is not advisable, as this time interval (0.2 ka) is significantly smaller than the typical uncertainty of SRSF ages (~1 ka). Despite this, the hypothesis of an even distribution of SRSF events through time can be rejected at $p<0.01$ irrespective of the age classes used.

The weighted age-frequency distribution (Fig. 6C) has four modes (at ~ 8.9, 7.3, 5.9 and 4.5 ka), which suggests that only four minor phases of enhanced SRSF frequency are meaningful. Furthermore, according to the weighted distribution, the frequency of events declines steadily after ~4.5 ka with no marked fluctuations.

The temporal pattern in the magnitude of the SRSFs (rock volume), as shown in in Fig. 6D, is substantially the same as the frequency distribution (compare with use of a 200-yr interval in Fig. 6B). In particular, the age-volume distribution has a similar major peak between 4.8 and 4.2 ka, and relatively little activity before 9.0 ka or after 1.0 ka.

Probability density function analysis indicates that the spread of SRSF ages does not conform to a normal distribution (Fig. 7A) and, instead, is best explained by 5 individual Gaussian age distributions (Fig. 7B). The sum of individual Gaussian distributions produces a re-integrated PDE which achieves a good model fit with the cumulative PDE. PDE analysis using < 5 individual Gaussian age distributions returns a poor ($n \leq 3$) or sub-optimal ($n = 4$) model fit. PDE analysis using > 5 individual Gaussian age distributions does not therefore significantly improve the model fit and instead risks over-interpretation of the number of SRSF modes. PDE analysis returns peak Gaussian ages (Fig. 7C) of 9.00 ± 1.13 ka (n = 14), 7.38 ± 0.99 ka (n = 17), 6.40 ± 0.77 ka (n = 14), 4.50 ± 1.42 ka (n = 42) and 1.90 ± 1.42 ka (n = 18). Although

these modes overlap with adjacent modes within 1σ, statistically significant differences between sequential Gaussian age distributions are revealed by two-sample Students t-tests ($p < 0.01$).

These Gaussian age distributions closely match the four modes identified in weighted age-frequency analysis, with a dominant mode at ~4.5 ka (Fig. 7B). This mode is the highest probability Gaussian distribution, comprises a significant number of SRSF events (n = 42; Fig. 7D) and accounts for a large proportion of total SRSF volume over the last ~10 ka (18,744 m^3). In contrast to weighted age-frequency analysis, PDE analysis returns an additional Gaussian age distribution during the late Holocene at ~1.9 ka. However, this is unlikely to reflect a period of enhanced SRSF activity as there is no clear clustering of SRSF ages (Fig. 7A), as evidenced by weighted age-frequency analysis. Instead, late Holocene ages likely reflect declining SRSF activity after the mid-Holocene peak.

The combined results of the age-frequency analyses and the Gaussian separation achieved for PDEs demonstrate that SRSF occurrence through time is non-uniform and multi-modal. Most notable is the high level of occurrence during the mid Holocene, the clear statistical significance of which is confirmed by the results of change detection analysis. The cumulative sum change detection graph (Fig. 8A) shows a clear peak in the rate of SRSF intensity between 4.8 and 2.6 ka, significantly exceeding the 2σ threshold, with the largest departure from background occurring at 4.3 ka. Conversely, SRSF intensity is significantly reduced beyond the negative 2σ threshold during the late Holocene at 0.6–0.1 ka. These peaks are a significant departure from the normal rate of occurrence during the Holocene. The three other modes identified above as statistically significant must be regarded as relatively small departures from background SRSF periodicity.

Meyer wavelet analysis was used to explore the two statistically significant departures (> 2σ) from the background SRSF rate, as identified by change detection analysis. The lowest frequency decomposed signal (d_6) is shown in Fig. 8C. The full analysis record is provided in Supplementary Fig. 1.

Discussion

Previous models of the timing of RSFs

Widely different conceptual models can be proposed to describe and explain the temporal distribution of Late Pleistocene and Holocene RSFs. A schematic representation of several models, each of which links a distinctive pattern of change in the frequency and/or magnitude of RSFs to one or more specific causes or triggers, is shown in Fig. 9. Although they have been based mainly on MRSFs, these models are introduced here as a basis for discussion of our Holocene SRSFs. It should be emphasised, moreover, that RSFs may be multicausal and that most if not all of the models have yet to be rigorously tested against data sets with a large number of consistently dated RSFs.

Model 1. – The 'continuity-of-activity model' proposes that there are no significant temporal variations in the frequency and/or magnitude of RSFs throughout the

Holocene. Despite the small number of dated RSFs available in most studies, few authors have advocated this model. However, the model does appear to be consistent with the temporal distribution of about 60 RSFs located in an extensive area of the Alps centred on the Austrian Tyrol (Prager et al. 2008), which exhibits only limited evidence of temporal clustering at ~10.5-9.4 ka and 4.2-3.0 ka. Prager et al. (2008) attributed the continuity of activity to complex interactions between the processes characterizing models 2-5 together with rock-strength degrading processes such as time-dependent progressive fracture propagation that can both prepare and trigger slope instabilities.

Model 2. – The 'intermittent-earthquakes model' is applicable to tectonically active regions and assumes that RSFs are triggered directly by large-magnitude earthquakes generated by tectonically-driven uplift or other crustal stresses. Such earthquakes are essentially randomly distributed in time and therefore bear little or no relationship to deglaciation, climate or any of the other potential causative factors in models 3-5 that are effective in tectonically stable regions (see, for example, Fjeldskaar et al. 2000; Hermanns et al. 2001; Keefer 2002, 2015; Hewitt et al. 2008; Antinao & Gosse 2009; Stock & Uhrhammer 2010; Penna et al. 2011; McPhillips et al. 2014; Marc et al. 2015; Murphy 2015).

Model 3. – The 'deglaciation-close-tracking model' is characterised by a dominant peak in RSF activity immediately (i.e. within the first millennium) following regional deglaciation, with subsequent asymptotic decline in activity. The temporal pattern of activity is therefore a typical paraglacial response (cf. Ballantyne 2002). Causal factors that may account for such a pattern include glacial unloading, glacial debuttressing, stress-release fracturing, enhanced groundwater pressure in rock joints and permafrost degradation, all closely associated in time with deglaciation (Fischer et al. 2006; Cossart et al. 2008; McColl 2012; McColl & Davies 2012; Ballantyne et al. 2014a, 2014b; Böhme et al. 2015; Deline et al. 2015; Mercier et al. 2017). Hermanns et al. (2017) found nearly half of 22 dated rock avalanches in southwest Norway occurred within the first millennium following local deglaciation. Although the majority of RSF events occur shortly after deglaciation, some occur much later, due to time-dependent fracture propagation and progressive failure (e.g. Eberhardt et al. 2004; Krautblatter et al. 2013; Phillips et al. 2017). The occurrence of recent RSFs on glacier forelands following the retreat of mountain glaciers from their Little Ice Age maximum limits provides some support for this model (Evans & Clague 1994; Holm et al. 2004; Matthews & Shakesby 2004; Arsenault & Meigs 2005; Allen et al. 2010; Stoffel & Huggel 2012).

Model 4. – The 'deglaciation-lagging model' features a significantly delayed response to deglaciation. Peak RSF activity typically occurs within a few millennia of deglaciation and corresponds with maximum glacio-isostatic rebound (Hicks et al. 2000; Ballantyne & Stone 2013; Ballantyne et al. 2013, 2014a, 2014b; Cossart et al. 2014; Decaulne et al. 2016). The cause of RSF events is seen as fault reactivation and fracture propagation triggered by earthquakes, the frequency of earthquakes and RSFs generally diminishing through the Holocene as the rate of glacio-isostatic uplift declines.

Model 5. – The 'cool/wet-climate-response model' applies particularly to the Holocene, reflecting several possible effects of climatic variations on RSF activity.

Field monitoring, historical documentation and palaeo-studies indicate that precipitation variations can be a dominant trigger factor in the timing of RSFs but both cooler conditions and indirect effects such as variations in cleft water pressure, frost shattering and permafrost degradation have also been implicated in rock-slope instability (Eisbacher & Clague 1984; Matthews et al. 1997; Trauth et al. 2000, 2003; Dapples et al. 2003; Soldati et al. 2004; Prager et al. 2008; Crozier 2010; Borgatti & Soldati 2010; Blikra & Christiansen 2014; Zerathe et al. 2014; Johnson et al. 2017). Furthermore, Evans & Clague (1994), Huggel et al. (2010, 2012) and Stoffel & Huggel (2012) highlighted the possible effects of recent climate warming on RSFs, and direct solar heating of rock faces has also been examined as a possible trigger (cf. Allen & Huggel 2013; Collins & Stock 2016). In Fig. 7, model 5 assumes cool/wet conditions produce an increase in RSF activity, resulting in a strong rising trend through the late Holocene with fluctuations culminating in a Little Ice Age maximum of RSF activity.

A new model of Holocene SRSF activity in Jotunheimen

Based on analysis of Holocene SRSF activity in Jotunheimen and comparison with regional climatic and geo-environmental indicators, a new thermally-driven, permafrost-degradation model is proposed (Fig. 7, model 6). This model is characterized by several key elements:

- minimal activity following deglaciation in the early Holocene;
- maximum activity late in the mid Holocene on the multi-millennial timescale;
- declining activity through the late Holocene with a second minimum close to the present;
- secondary fluctuations on multi-centennial to millennial timescales throughout the Holocene;

This pattern of change bears little relationship to any of the previous models, which are clearly inappropriate in the context of these data. Model 1 can be rejected for Jotunheimen on the basis of the χ^2 tests in Table 5. Although there is an element of randomness in our data, and earthquakes do occasionally occur in this part of southern Norway, their magnitudes tend to be too low to be effective in triggering SRSFs inland from the seismically more active coastal and off-shore areas (cf. Bungum et al. 2000; Fjeldskaar et al. 2000; Hicks et al. 2000; Olesen et al. 2000; Blikra et al. 2006). Moreover, there is no sign of a dominant early-Holocene activity peak in our histogram or change detection analysis, which is the characteristic feature of the two deglaciation-related models (3 and 4). Absence of an early peak may well be accounted for by considerable thinning of the Late Weichselian Ice Sheet prior to final deglaciation in Jotunheimen (Goehring et al. 2008; Mangerud et al. 2011; Hughes et al. 2016; Stroeven et al. 2016), which is likely to have reduced the scale of any paraglacial effects on RSFs after ~10.0 ka. For example, over half (56%) of the estimated glacio-isostatic rebound of 160 m that has taken place in Jotunheimen since 12.0 ka was completed prior to 10.0 ka and a further quarter (26%) by 6.0 ka (Lysså et al. 2008). Finally, the temporal pattern of SRSF activity in Jotunheimen is negatively correlated with model 5, which indicates that cool/wet conditions should be rejected as the major cause of enhanced SRSF activity. Instead, this inverse pattern points to the counterintuitive conclusion that enhanced activity is linked to relatively warm climatic conditions.

Association of SRSF activity with the thermal climate record

The possible associations between enhanced Holocene SRSF activity and relatively warm climatic conditions can be explored with reference to proxy temperature records and reconstructions of temperature-sensitive geo-environmental indicators (Fig. 10A-G).

The long-term annual air temperature trend for Northern Europe shown in Fig. 10B is a stacked pollen-based reconstruction expressed as deviations from the mean (Seppä et al. 2009). The Holocene Thermal Maximum (HTM) is clearly expressed in this figure from ~8.0 to 4.0 ka by mean annual temperatures consistently >0.5 °C higher than today. Alkenone-based temperature reconstruction similarly documents warmest sea-surface temperatures in the North Atlantic at this time (Eldevik et al. 2014; see also Jansen et al. 2008; Renssen et al. 2012). However, other reconstructions based on chironomids (Velle et al. 2010), aquatic macrofossils (Väliranta et al. 2015) and megafossils (Dahl & Nesje 1996; Paus & Haugland 2017), which are not dependent on tree-pollen production or ocean temperatures, indicate that the highest temperatures probably occurred at 10.0–8.0 ka. Mean summer temperatures estimated from pine-tree limits in the Scandes Mountains (Dahl & Nesje 1996), for example, peak at ~1.5 °C above present temperatures around 9.0 ka (Fig. 10C). An early temperature maximum at ~9.0 ka is also shown in the pollen-based reconstruction of July air temperature from Øvre Heimdalsvatnet in the low-alpine belt of eastern Jotunheimen (Fig. 10D, Velle et al. 2010). At this location, a temperature of at least 3.5 °C higher than present was attained by 9.0 ka, falling to the long-term Holocene average by 4.0 ka. Comparison with these reconstructions indicates that (1) SRSF frequency increased during the HTM and (2) maximum activity was not reached until late in the HTM.

Three other palaeorecords can be used to focus on shorter-term warm intervals comparable in scale with our minor phases of enhanced SRSF frequency (Fig. 10E-G). The first of these (Fig. 10E), based on a standardized temperature reconstruction derived from the record of $\delta^{18}O$ in the GISP 2 Greenland ice core (Alley 2004; Wanner et al. 2011, their Fig. 1a), shows periods of above average air temperature. Fig. 10F, based on the North Atlantic standardized stacked ocean ice-rafted debris (IRD) record (Bond et al. 2001; Wanner et al. 2011, their Fig. 3a), shows periods between IRD events, when sea-surface temperatures are likely to have been above the long-term average. Both sets of warm periods demonstrate only moderate agreement between themselves and with our minor phases of enhanced SRSF frequency. There is poorer agreement (particularly in the late Holocene after ~3.0 ka) with the final record, which relates to variations in the size of mountain glaciers in the study area (Fig. 10G). Glacier variations are widely accepted as climate indicators that reflect, in part, temporal variations in summer temperature, especially in the case of glaciers in continental locations where winter precipitation variations tend to be less effective than in maritime regions (Oerlemans 2005; Bakke et al. 2008; Nesje et al. 2008; Winkler et al. 2010). Local glacier variations in the Smørstabbtindan massif, Jotunheimen, which is centrally located in relation to the sites of our SRSF events in a relatively continental region of southern Norway, exhibit at least nine Holocene time intervals when the glaciers were smaller than they are today, including a prolonged period from ~7.8 to 4.8 ka, which includes most of the HTM (Fig. 10G; Matthews &

Dresser 2008).

Thus, overall, a strong case can be made for linking millennial-scale variations in SRSF activity to the thermal environment. However, causal mechanisms are required to answer the following questions: (1) why was maximum SRSF activity attained late in the mid-Holocene, rather than earlier in the HTM when temperatures were at a maximum; and (2) why was there not a closer relationship between the minor phases of enhanced SRSF activity and shorter-term warm periods, such as the Mediaeval, Roman and Bronze Age warm periods, in particular during the late-Holocene? We propose that permafrost degradation, and climate-dependent variation in permafrost depth, can explain the temporal pattern of SRSF activity and, in particular, the departure of the temporal pattern of SRSF activity from a simple 'warm-climate' model.

Conditionality of SRSF activity on permafrost degradation

To interpret the results of both the change detection analysis and Meyer wavelet analysis, a modelled permafrost record for Fennoscandia (Kukkonen & Šafanda 2001) is used (Fig. 8B). This provides a basis for attributing SRSF activity in Jotunheimen to permafrost degradation by focusing on relative changes to permafrost depth in bedrock over the last ~10 ka. The 5% porosity model was selected for comparison as this is more representative than the 0% porosity model given the numerous fractures that lead to slope instability and SRSFs. The permafrost model shows a significant decrease in depth beginning at ~8 ka and reaching a steady 'shallow' equilibrium by ~5 ka. Permafrost is relatively stable from 5 ka until ~0.6 ka when permafrost depth increases. This permafrost model is subdivided into five distinct periods and is related to the SRSF record as follows:

Phase 1: 10.0–8.1 ka ('stable phase'). – SRSF frequency is in equilibrium with permafrost with no alarms detected in the change detection analysis and no low-order oscillations in the Meyer wavelet record. Bedrock permafrost is stable throughout this period and is used to define background Holocene depth. In this phase, persistent bedrock permafrost acts to stabilize slopes and limit major SRSF activity.

Phase 2: 8.1–4.8 ka ('transition phase'). – Progressive warming throughout the mid-Holocene, as recorded in palaeo-climate reconstructions, acts to decrease permafrost depth. In response, there is a minor progressive decrease in negative change detection rates and increase in positive change detection within 2σ. This trend is matched by Meyer wavelet analysis, with a progressive increase in SRSF frequency above the Holocene background rate. In this phase, a gradual (~3 ka) but clear transition from 'deeper' to 'shallower' permafrost (~28% depth change) is matched by a minor increase in SRSF frequency and may explain the minor phases of enhanced SRSF activity identified during this period. Moreover, this gradual change in permafrost depth, as opposed to a stochastic response to climate warming, provides a compelling explanation for the significant lag between SRSF activity and the HTM.

Phase 3: 4.8–2.6 ka ('peak phase'). – Permafrost depth is more-or-less stable and remains close to its minimum Holocene depth for ~2 ka. This period is matched by SRSF activity, as change detection analysis records a significant, sustained and positive rate of change (> 2σ) for ~2.2 ka, with a maximum attained at ~4.3 ka and

with SRSF frequency significantly exceeding the average frequency until ~3.3 ka (> 6σ). This change is matched by the Meyer wavelet record, with a peak at ~4.6 ka and a gradual decline to the Holocene background rate at ~2.5 ka. In this phase, persistent shallow permafrost may directly influence SRSF occurrence by (1) actively destabilizing bedrock cliffs and causing slope failure and/or (2) weakening bedrock cliffs and making them more susceptible to other trigger factors.

Phase 4: 2.6–0.6 ka ('exhaustion phase'). – Permafrost depth remains relatively stable and shallow for ~2 ka, with no significant deviation from modelled depths during the 'peak phase'. However, there is a clear decrease in SRSF frequency after the mid-Holocene peak with a return to the Holocene background rate, as revealed by both change detection and Meyer wavelet analysis. In this phase, we propose that bedrock cliffs have reached a new equilibrium with permafrost, as the majority of slopes that can fail under these permafrost conditions have failed by this time; that is, the supply of 'potentially failable' cliffs is exhausted. As a result, SRSF occurrence returns to an average frequency comparable with the 'stable phase' of the early Holocene.

Phase 5: 0.6 - 0.1 ka ('stabilization phase). – Contrary to the dominant Holocene trend, this short-term late-Holocene phase shows a clear increase in permafrost depth after ~0.6 ka. This transition is coeval with a statistically significant decrease in SRSF frequency (> 2σ) while Meyer wavelet analysis records the continued decrease in frequency below the Holocene background level. These data suggest that an increase in bedrock permafrost depth directly controls SRSF activity by stabilizing slopes and decreasing the susceptibility of bedrock cliffs to direct or indirect failure.

The correlation between SRSF frequency and permafrost depth in bedrock as modeled by Kukkonen & Šafanda (2001) provides a compelling explanation for the low-frequency variations in SRSF activity during the Holocene and, in particular, for:

- the significant departure from mean Holocene SRSF frequency at the end of the mid Holocene;
- the lag between the HTM and the SRSF frequency peak;
- the low SRSF frequency in the early Holocene; and
- the marked decline in SRSF frequency near the end of the late Holocene (after ~0.6 ka).

These explanations are supported by change detection analysis and (d_6) Meyer wavelet analysis. A causal link between SRSF frequency and regional permafrost degradation is also supported by the close match between the altitudinal distribution of the 92 SRSFs and the current aspect-dependent lower altitudinal limit of permafrost in rock faces in the Galdhøpiggen massif (Hipp et al. 2014). Approximately 87% (n = 80) of SRSFs occur within ± 300 m of the limit and ~62% (n = 57) are ≤ 200 m below this limit. A small number of SRSFs are found above the permafrost limit (~16%; n = 15) but the majority are restricted to within ≤ 50 m above this limit. These data imply a causal relationship between SRSF occurrence and the time-dependent degradation and aggradation of bedrock permafrost during the Holocene, as driven by climate and locally controlled by aspect. Based on an altitudinal lapse rate of 0.6 °C per 100 m in mean annual air temperatures (MAAT), this implies that all SRSF sites would have been in the permafrost zone when temperatures were 3.0 °C lower than today. It is likely, therefore, that much of the permafrost that had survived or developed in SRSF

cliffs following deglaciation would have degraded during the HTM when MAAT is likely to have reached 2.0–3.0 °C warmer than at present and when permafrost limits would have been correspondingly higher (Lilleøren et al. 2012).

Higher-frequency changes in SRSF activity as reflected by weighted age-frequency (Fig. 6C) and (d_1-d_5) wavelet analysis (Supplementary Fig. 1) can be interpreted as represent Holocene background SRSF frequency after removal of the mid-Holocene positive peak and the late-Holocene negative peak of the change detection analysis (Fig. 8A). These higher frequency changes are more challenging to interpret, given the limited availability of palaeo-environmental records (e.g. seasonal paleo-precipitation data, storm-event chronologies, palaeoseismic and groundwater flux records) and the inherent SHD age uncertainties. The conceptual models related to deglaciation and characterized by early-Holocene peak activity (Fig. 9) can be discounted as these bear limited resemblance to the chronology of SRSF events.

Changes in permafrost depth might be expected to play a role in explaining the higher-frequency changes. However, we cannot preclude a contribution to higher-frequency variability from the continuity, earthquake, and cool/wet climate conceptual models (Fig.9). Thawing permafrost may be a direct trigger factor for SRSF events due, for example, to loss of strength or elevated hydrostatic pressure, or it may render the rock slope susceptible to other triggers involving meltwater from spring snow melt or extreme rainfall events in summer (Gruber et al. 2004; Gruber & Haeberli 2007; Krautblatter et al. 2013; Blikra & Christiansen 2014; Draebing et al. 2014; Krautblatter & Leith 2015; Messenzehl & Dikau 2017). Extreme summer rainfall events, which are likely to have been more frequent during warm periods, have been implicated in triggering debris-flow events in Leirdalen (Matthews et al. 2009) and might have triggered some SRSFs.

Further conceptual and methodological implications

Thus, the timing of SRSFs in this study, with fluctuating SRSF activity rising to a sustained peak at the transition from the mid- to late-Holocene, suggests the importance of progressive but intermittent permafrost degradation lagging behind the highest temperatures of the Holocene. Subsequent declining SRSF frequencies, in contrast, appear to signal exhaustion of the supply of failable cliffs and/or renewed aggradation of permafrost.

These fundamental findings recognize that Holocene SRSF activity in Jotunheimen essentially reflects paraperiglacial processes: that is, it is a conditional response to the transition from a permafrost to a seasonal-freezing climatic regime as permafrost depth decreases (cf. Mercier 2008; Scarpozza 2016; Matthews et al. 2017). While this model is primarily applicable to the SRSFs sampled in this study, it could be tested in comparable mountain regions. In particular, links between permafrost degradation and enhanced slope failure may explain SRSF frequency in regions with comparable seismotectonics, glaciation and deglaciation histories or climatic trends. Robust SRSF chronologies would need to be constructed to test the model, either using radiometric methods (e.g. ^{10}Be) or calibrated-age dating techniques (e.g. SHD).

Our new SRSF chronology indicates, moreover, that SHD can be used to generate reliable SRSF chronologies, although further work is necessary to verify this

technique by directly comparing age estimates for individual landforms derived from both SHD and radiometric methods.

Finally, the recognition of a causal link between climate, permafrost degradation and enhanced slope instability may have important implications for glacial and periglacial environments under global warming scenarios. In particular, while widespread retreat of mountain ice caps and valley glaciers may trigger initial slope instability, our data suggest that the geomorphological impact of current climatic and deglacial trends and, in particular, the slow transition from glacial to periglacial, and to seasonal-freezing climatic regimes, may have a long-lasting impact on mountain environments.

Conclusions

(1) We have developed an approach to the exposure-age dating of a large sample of rock-slope failures, which involves adapting Schmidt-hammer exposure-age dating (SHD) as a calibrated-age dating technique to the specific characteristics of small rock-slope failures (SRSFs). SHD has provided an effective and low-cost method for constructing a regional Holocene chronology of SRSFs (12 to 2520 m^3) in the alpine zone of Jotunheimen.

(2) Focusing on a large sample of SRSFs enables the detection of temporal variations in the frequency and magnitude of events through the Holocene. Modes in a weighted age-frequency distribution at ~8.9, 7.3, 5.9 and 4.5 ka were substantiated by probability density function analysis, which produced individual Gaussian age distributions of 9.00 ± 1.13 ka, 7.38 ± 0.99 ka, 6.40 ± 0.77 ka and 4.50 ± 1.42 ka. Based on this analysis, SRSF activity was relatively low following deglaciation in the early Holocene and attained a maximum towards the end of the mid Holocene (~4.5 ka). Peak SRSF activity lagged behind the Holocene Thermal Maximum by at least ~2.2 ka and declined thereafter with a very low frequency of events during the last millennium.

(3) Using change detection and discreet Meyer wavelet analysis in combination with proxy temperature indicators and an existing permafrost depth model, we propose that enhanced SRSF activity was primarily controlled by permafrost degradation. As a result, the Holocene permafrost depth record is subdivided into five distinct periods and related to the SRSF chronology as follows:

- 10 - 8.1 ka – 'stable phase' – low SRSF activity; maximum Holocene permafrost depth.
- 8.1 - 4.8 ka – 'transition phase' – increasing susceptibility to SRSF activity; decreasing permafrost depth.
- 4.8 - 2.6 ka – 'peak phase' – maximum SRSF activity; minimum Holocene permafrost depth.
- 2.6 - 0.6 ka – 'exhaustion phase' – decreasing SRSF activity; little change in shallow permafrost depth.
- 0.6 - 0.1 ka – 'stabilization phase' – minimum SRSF activity; increasing permafrost depth.

(4) Long-term relative change in permafrost depth provides a compelling explanation for the high-magnitude departures from the SRSF background rate. In particular, the gradual change in permafrost depth during the 'transition phase', as opposed to a stochastic response to climate warming, accounts for the significant lag (~2.2 ka) between the Holocene Thermal Maximum and the SRSF frequency peak. Moreover, persistent shallow permafrost during the 'peak phase' may be the key driver behind SRSF occurrence by (a) actively destabilizing bedrock cliffs and causing slope failure and/or (b) weakening bedrock cliffs and making them more susceptible to other trigger factors.

(5) Conversely, declining SRSF frequency during the 'exhaustion phase' appears to reflect the diminished supply of potentially failable cliffs, even under a shallow permafrost depth scenario. Finally, low frequency of SRSF occurrence during the 'stabilization phase' likely reflects an increase in permafrost depth (permafrost aggradation) after ~0.6 ka; a change which would have been sufficient to stabilize slopes and decrease the susceptibility of bedrock cliffs to direct or indirect failure.

(6) This interpretation is supported by geomorphological evidence, given the consistent location of SRSF sites in relation to the local aspect-dependent lower altitudinal limit of permafrost in cliff faces. This new paraperiglacial model attributes enhanced SRSF activity to progressive and intermittent permafrost degradation during Holocene warm periods, including the possibility of renewed aggradation of permafrost during short-term cold periods and renewed degradation during the ensuing warm periods

(7) Our new thermally-driven, permafrost-degradation model of SRSF events in Jotunheimen bears little similarity to existing models of Holocene RSF activity. However, while aspects of this new model require further testing by other methods and in other regions, the results of this study have important implications for climate-change forcing of RSF activity. Projected mean annual global warming is predicted to decrease the area of mountain permafrost and raise lower altitudinal permafrost limits. This in turn will likely destabilize higher bedrock slopes and increase SRSF frequency there. The delayed response of peak SRSF frequency to warming climate, as modulated by permafrost depth, may therefore result in a long-lasting impact of current climate trends on mountain environments.

Acknowledgements – Fieldwork was carried out on the Swansea University Jotunheimen Research Expeditions of 2014-2017. We are grateful to Ole and Tove Grindvold (Leirvassbu) for continuing expedition support; to Atle Nesje and Anne E. Bjune for data and sources of information on uplift rates and climate in southern Norway; and to R.L. Hermanns for a very thorough critical review that led to significant improvement of the manuscript. Anna C. Ratcliffe prepared the figures for publication. This paper constitutes Jotunheimen Research Expeditions, Contribution No. 205 (see http://jotunheimenresearch.wixsite.com/home).

References

Aa, A.R. & Sjåstad, J.A. 2000: Schmidt hammer age evaluation of the moraine

sequence in front of Bøyabreen, western Norway. *Norsk Geologiske Tidsskrift 80*, 27-32.

Aa, A.R., Sjåstad, J., Sønstegaard, E. & Blikra, L.H. 2007: Chronology of Holocene rock-avalanche deposits based on Schmidt-hammer relative dating and dust stratigraphy in nearby bog deposits, Vora, inner Nordfjord, Norway. *The Holocene* 17, 955-964.

Ahlmann, H.W. 1922: Glaciers in Jotunheimen and their physiography. *Geografiska Annaler 4*, 1-57.

Allen, S. & Huggel, C. 2013: Extremely warm temperatures as a potential cause of recent high mountain rockfall. *Global and Planetary Change 107*, 59-69.

Allen, S., Cox, S. & Owens, I. 2010: Rock avalanches and other landslides in the central Southern Alps of New Zealand: a regional study considering possible climate change impacts. *Landslides 8*, 33-48.

Alley, R.B. 2004: *GISP2 Ice Core Temperature and Accumulation Data. IGBP PAGES/World Data Center for Paleoclimatology Data Contribution Series #2004-013*. NOAA/NGDC Paleoclimate Program, Boulder, CO.

André, M.F. 1996: Rock weathering rates in Arctic and subarctic environments (Abisko Mts, Swedish Lappland). *Zeitschrift für Geomorphology NF 40*, 499-517.

André, M.F. 2002: Rates of postglacial rock weathering on glacially scoured outcrops (Abisko-Riksgränsen area, 68°N). *Geografiska Annaler Series A Physical Geography 64*, 139-150.

Andreassen, L.M. & Winsvold, H., 2012. *Inventory of Norwegian Glaciers.* Norwegian Water Resources and Energy Directorate (NVE), Oslo.

Antinao, J.L. & Gosse, J. 2009: Large rockslides in the southern central Andes of Chile (32–34°S): tectonic control and significance for Quaternary landscape evolution. *Geomorphology 104*, 117-133.

Arsenault, A.M. & Meigs, A.J. 2005: Contribution of deep-seated bedrock landslides to erosion of a glaciated basin in southern Alaska. *Earth Surface Processes and Landforms 30*, 1111-1125.

Aune, B. 1993: *Temperatur Normaler, Normalperiode 1961–1990*. Den Norske Meterorologiske Institutt, Oslo (Rapport 02/93, in Norwegian).

Bakke, J., Lie, Ø., Dahl, S.O., Nesje, A. & Bjune, A.E. 2008: Strength and spatial patterns of the Holocene wintertime westerlies in the NE Atlantic region. *Global and Planetary Change 60*, 28-41.

Ballantyne, C.K. 2002: Paraglacial geomorphology. *Quaternary Science Reviews 21*, 1035-2017.

Ballantyne, C.K. & Stone, J.O. 2013: Timing and periodicity of paraglacial rock-slope failures in the Scottish Highlands. *Geomorphology 186*, 150-161.

Ballantyne, C.K., Wilson, P., Schnabel, C. & Xu, S. 2013: Lateglacial rock slope failures in north-west Ireland: age, causes and implications. *Journal of Quaternary Science 28*, 789-802.

Ballantyne, C.K., Sandeman, G.F., Stone, J.O. & Wilson, P. 2014a: Rock-slope failure following Late Pleistocene deglaciation on tectonically stable mountainous terrain. *Quaternary Science Reviews 86*: 144-157.

Ballantyne, C.K., Wilson, P., Gheorghiu, D. & Rodés, À. 2014b: Enhanced rock-slope failure following ice-sheet deglaciation: timing and causes. *Earth Surface Processes and Landforms 39*, 900-913.

Barnett, C., Dumayne-Peaty, L. & Matthews, J.A. 2000: Holocene climatic change and tree-line response in Leirdalen, central Jotunheimen. *Review of*

Palaeobotany and Palynology 117, 119-137.
Barr, I.D., Roberson, S., Flood, R. & Dortch, J.M. 2017: Younger Dryas glaciers and climate in the Mourne Mountains, Northern Ireland. *Journal of Quaternary Science 32*, 104-115.
Bates, R.L. & Jackson, J.A. (eds) 1987: *Glossary of Geology, 3rd edition*, 573. American Geological Institute: Alexandria, VA.
Battey, M.H. & McRitchie, W.D. 1973: A geological traverse across the pyroxene-granulites of Jotunheimen in the Norwegian Caledonides. *Norsk Geologiske Tidsskrift 53*, 237-265.
Battey, M.H. & McRitchie, W.D. 1975: The petrology of the pyroxene-granulite facies rocks of Jotunheimen. *Norsk Geologiske Tidsskrift 55*, 1-49.
Benestad, R.E. 2005: Climate change scenarios for northern Europe from multi-modal IPCC AR4 climate simulations. *Geophysical Research Letters 32*, L17704.
Betts, M.W. & Latta, M.A. 2000: Rock surface hardness as an indication of exposure age: an archaeological application of the Schmidt hammer. *Archaeometry 42*, 209-223.
Blikra, L.H. & Christiansen, H.H. 2014: A field-based model of permafrost-controlled rockslide deformation in northern Norway. *Geomorphology 208*, 34-49.
Blikra, L.H., Longva, O., Braathen, A., Anda, E., Dehls, J.F. & Stalsberg, K. 2006: Rock slope failures in Norwegian fjord areas: examples, spatial distribution and temporal patterns. In Evans, S.G., Mugnozza, G.S., Strom, A. and Hermanns, R.L. (eds), *Landslides from Massive Rock Slope Failures*, 475-496. Springer: Dordrecht.
Böhme, M., Oppikofer, T., Longva, O., Jaboyedorff, M, Hermanns, R.L. & Derron, M.-H. 2015. Analyses of past and present rock slope instabilities in a fjord valley: imlications for hazard estimation. *Geomorphology 248*, 464-474.
Bond, G., Kromer, B., Beer, J., Muscheler, R., Evans, M.N., Showers, W., Hoffmann, S., Lotti-Bond, R.,Hajdas, R. & Bonani, G. 2001: Persistent solar influence on North Atlantic climate dring the Holocene. *Science 278*, 1257-1266.
Borgatti, L. & Soldati, M. 2010: Landslides and climatic change. In Alcántara-Ayala, I. & Goudie, A. (eds) *Geomorphological Hazards and Disaster Prevention*, 87-95. Cambridge University Press, Cambridge.
Braathen, A., Blikra, L.H., Berg, S.S. & Karlsen, F. 2004: Rock-slope failures in Norway: type, geometry, deformation mechanisms and stability. *Norwegian Journal of Geology 84*, 67-88.
Brideau, M.-A. & Roberts, N.J. 2015: Mass movement in bedrock. In Davies, T. (ed.) *Landslide Hazards, Risks, and Disasters, 43-90.* Elsevier, Amsterdam.
Briner, J.P., Kaufman, D.S., Manley, W.F., Finkel, R.C., & Caffee, M.W. 2005: Cosmogenic exposure dating of late Pleistocene moraine stabilization in Alaska. *Geological Society of America Bulletin 117*, 1108-1120.
Brunsden, D. & Prior, D.B. (eds) 1984: *Slope Instability*. Wiley, Chichester.
Bungum, H., Lindholm, C.D., Dahle, A., Woo, G., Nadim, F., Holme, J.K., Gudmestad, O.T., Hagberg, T. & Karthisgeyan, K. 2000: New seismic zoning maps for Norway, the North Sea, and the United Kingdom. *Seismological Research Letters 71*, 687-697.
Černá, B. & Engel, Z. 2011: Surface and sub-surface Schmidt hammer rebound value variation for a granite outcrop. *Earth Surface Processes and Landforms 36*, 170-170.
Clague, J.J. & Stead, D. (eds) 2012: *Landslides: Types, Mechanisms and Modeling*, Cambridge University Press: Cambridge.

Collins, B.D. & Stock, G.M. 2016: Rockfall triggering by cyclic thermal stressing of exfoliation fractures. *Nature Geoscience 9*, 395-399.

Colman, S.M. 1981: Rock-weathering rates as functions of time. *Quaternary Research 15*, 250-264.

Colman, S.M. & Dethier, D.P. (eds.) 1986: *Rates of Chemical Weathering of Rocks and Minerals*. Academic Press, Orlando, FL.

Colman, S.M., Pierce, K.L. & Birkeland, P.W. 1987: Suggested terminology for Quaternary dating methods. *Quaternary Research 28*, 314-319.

Cossart, E., Braucher, R., Fort, M., Bourlès, D.L. & Carcaillet, J. 2008: Slope instability in relation to glacial debuttressing in alpine areas (Upper Durance catchment, southeastern France): evidence fromm field data and ^{10}Be cosmic ray exposure ages. *Geomorphology 85*, 3-26.

Cossart, E., Mercier, D., Decaulne, A., Feuillet, T, Jónsson, H.P. & Þorsteinn Sæmundsson 2014: Impacts of post-glacial rebound on landslide spatial distribution at a regional scale in northern Iceland (Skagafjörður). *Earth Surface Processes and Landforms 39*, 336-353.

Crosta, G.B. & Clague, J.J. 2009: Dating, triggering, modelling, and hazard assessment of large landslides. *Geomorphology 103*, 1-4. [Introduction to the Special Issue.]

Crozier, M.J. 2010: Deciphering the effect of climate change on landslide activity: a review. *Geomorphology 124*, 260-267.

Cruden, D.M. & Varnes, D.J. 2009: Landslide types and processes. In: Turner, A.K. & Schuster, R.L. (eds) *Landslides Investigation and Mitigation*. Transportation Research Board, US National Research Council: Washington, DC: Transportation Research Board, US National Research Council, pp. 36-75. [Special Report 247.]

Dahl, S.O. & Nesje, A. 1996: A new approach to calculating Holocene winter precipitation by combining glacier equilibrium-line altitudes and pine-tree limits: A case study from Hardangerjøkulen, central-southern Norway. *The Holocene 6*, 381-398.

Dahl, S.-O., Nesje, A., Lie, Ø., Fjordheim, K. & Matthews, J.A. 2002: Timing, equilibrium-line altitudes and climatic implications of two early-Holocene glacial re-advances during the Erdalen Event at Jostedalsbreen, western Norway. *The Holocene 12*, 17-25.

Dann, R., Close, M., Flintoft, M., Hector, R., Barlow, H., Thomas, S. & Francis, G. 2009: Characterization and estimation of hydraulic properties in an alluvial gravel vadose zone. *Vadose Zone Journal* 8, 651-663.

Dapples, F., Oswald, D, Raetzo, H., Landelli, T. & Zwahlen, P., 2003: New records of Holocene landslide activity in the Western and Eastern Swiss Alps: implications of climate and vegetation changes. *Eclogae Geologicae Helvetiae 96*, 1-9.

Davies, T. (ed.) 2015: *Landslide Hazards, Risks, and Disasters.* Elsevier, Amsterdam.

Decaulne, A., Cossart, E., Mercier, D., Feuillet, T., Coquin, J. & Jónsson, H. 2016: An early Holocene age for the Vatn landslide (Skagafjörður, central northern Iceland): insights into the role of postglacial landsliding on slope development. *The Holocene 26*, 1304-1318.

Deline, P. & Kirkbride, M.P. 2009: Rock avalanches on a glacier and morainic complex in Haut Val Ferret (Mont Blanc Massif, Italy). *Geomorphology 103*, 80-92.

Deline, P., Gruber, S., Delaloye, R., Fischer, L., Geertseema, M., Giardino, M., Hasler, A., Kirkbride, M., Krautblatter, M., Magnin, F., NcColl, S., Ravanel, L. & Schoeneich, P. 2015: Ice loss and slope stability in high-mountain regions. In Haeberli, W. & Whitman, C. (eds), *Snow and Ice-Related Hazards, Risks and Disasters*, 521-561. Elsevier, Amsterdam.

Dera, Z.A. & Shumwayb, R.H. 1999: Phase onset time estimation at regional distances using the CUSUM algorithm. *Physics of the Earth and Planetary Interiors 113*, 227-246.

Dortch, J.M., Owen, L.A., Haneberg, WC., Caffee, M.W., Dietsch, C. & Kamp, U. 2009: Nature and timing of large landslides in the Himalaya and Transhimalaya of northern India. *Quaternary Science Reviews 28*, 1037-1054.

Dortch, J.M., Owen, L.A. & Caffee, M.W. 2013: Timing and climatic drivers for glaciation across semi-arid western Himalayan-Tibetan orogen. *Quaternary Science Reviews 78*, 188–208.

Draebing, D., Krautblatter, M. & Dikau, R. 2014: Interaction of thermal and mechanical processes in steep permafrost rock walls: a conceptual approach, *Geomorphology 226*, 226-235.

Eberhardt, E., Stead, D. & Coggan, J.S. 2004: Numerical analysis of initiation and progressive failure in natural rocks slopes: the 1991 Randa rockslide. *International Journal of Rock Mechanics and Mining Sciences 41*, 69-87.

Eisbacher, G.H. & Clague, J.J. 1984: Destructive mass movements in high mountains: hazards and management. *Geological Survey of Canada, Paper 84/16*, 1-230.

Eldevik, T., Risebrobakken, B., Bjune, A.E., Andersson, C., Birks, H.J.B., Dokken, T.M., Drange, H., Glessmer, M.S., Li, C., Nilsen, J.E.Ø., Ottera, O.H., Richter, K. & Skagseth, Ø. 2014: A brief history of climate – the northern seas from the Last Glacial Maximum to global warming. *Quaternary Science Reviews 106*, 225-246.

Etzelmüller, B., Berthling, I. & Sollid, J.L. 2003: Aspects and concepts on the geomorphological significance of Holocene permafrost in southern Norway. *Geomorphology 52*, 87-104.

Evans, S.G. & Clague, J.J. 1994: Recent climate change and catastrophic geomorphic processes in mountain environments. *Geomorphology* 10, 107-128.

Evans, S.G., Mugnozza, G.S., Strom, A. & Hermanns, R.L. (eds) 2006: *Landslides from Massive Rock Slope Failures*. Springer, Dordrecht.

Farbrot, H., Hipp, T.F., Etzelmüller, B., Isaksen, K., Ødegård, R.S., Schuler, T.V. & Humlum, O. 2009: Air and ground temperature variations observed along elevation and continentality gradients in southern Norway. *Permafrost and Periglacial Processes 22*, 343–360.

Fischer, L., Kääb, A., Huggel, C. & Noetzli, J. 2006: Geology, glacier retreat and permafrost degradation as controlling factors of slope stability in a high mountain rock wall. *Natural Hazards and Earth System Sciences 6*, 761-772.

Fjeldskaar, W., Lindholm, C., Dehls, J.F. & Fjeldskaar, I. 2000: Postglacial uplift, neotectonics and seismicity in Fennoscandia. *Quaternary Science Reviews 19*, 1413-1422.

Førland, E.J. 1993: *Nedbørnormaler, Normalperiode 1961–1990.* Den Norske Meterorologiske Institutt, Oslo (Rapport 39//93, in Norwegian).

Frattini, P., Crosta G.B. & Agliardi, F. 2012: Rockfall characterization and modeling. In Clague, J.J. & Stead, D. (eds), *Landslides: Types, Mechanisms and Modeling*, 267-271. Cambridge University Press: Cambridge.

Gibbs, A.D. & Banham, P.H. 1979: *Sygnefjell Berggrunnsgeologisk kart 1518 III*,

1:50,000. Norges Geologiske Undersøkelse, Trondheim.
Ginås, K., Etzelmüller, B., Lussana, C., Hjort, J., Sannel, A.B.K., Isaksen, K., Westermann, S., Kuhry, P., Christiansen, H., Frampton, A. & Åkerman, J. 2017: Permafrost map for Norway, Sweden and Finland. *Permafrost and Periglacial Processes 28*, 359–378.
Gjessing, J. 1967: Norway's paleic surface. *Norsk Geografisk Tidsskrift 21*, 69-132.
Goehring, B.M., Brook, E.J., Linge, H., Raisbeck, G.M. & Yiou, F. 2008: Beryllium-10 exposure ages of erratic boulders in southern Norway and implications for the history of the Fennoscandian Ice Sheet. *Quaternary Science Reviews 27*, 320-336.
Goudarzi, M.A., Cocard, M., Santerre, R. & Woldai, T. 2013: GPS interactive time series analysis software. *GPS Solutions 17*, 595-603.
Gruber, S. & Haeberli, W. 2007: Permafrost in steep bedrock slopes and its temperature-related destabilization following climate change. *Journal of Geophysical Research – Earth Surface 112*, F02S18. DOI: 10.1029/2006JF000547.
Gruber, S., Hoelzle, M. & Haeberli, W. 2004: Permafrost thaw and destabilization of Alpine rock walls in the hot summer of 2003. *Geophysical Research Letters 31*, L13504. doi:10.1029/2004GL020051
Hall, K., Thorn, C.E., Matsuoka, N. & Prick, A. 2002: Weathering in cold regions: some thoughts and perspectives. *Progress in Physical Geography 26*, 577-603.
Hallet, B., & Putknonen, J. 1996: Surface dating of dynamic landforms: young boulders on aging moraines. *Science 26,* 937-940.
Hallet, B., Walder, J.S. & Stubbs, C.W. 1991: Weathering by segregation ice growth in microcracks at sustained sub-zero temperatures: verification from an experimental study using acoustic emissions. *Permafrost and Periglacial Processes* 2, 283-300.
Hermanns, R.L. & Longva, O. 2012: Rapid rock-slope failures. In Clague, J.J. & Stead, D. (eds): *Landslides: Types, Mechanisms and Modeling*, 59-70. Cambridge University Press: Cambridge.
Hermanns, R.L., Trauth, M.H., Niedermann, S., McWilliams, M. & Strecker, M.R. 2000: Tephrochronological constraints on temporal distribution of large landslides in Northwest Argentina. *Journal of Geology 108*, 35-52.
Hermanns, R.L., Niedermann, S., Garcia, A.V., Gomez, J.S. & Strecker, M.R. 2001: Neotectonics and catastrophic failure of mountain fronts in the southern intra-Andean Puna Plateau, Argentina. *Geology 29*, 619-623.
Hermanns, R.L., Niedermann, S., Ivy-Ochs, S. & Kubik, P.W. 2004: Rock avalanching into a landslide-dammed lake causing multiple dam failure in Las Conchas valley (NW Argentina) – evidence from surface exposure dating and stratigraphic analysis. *Landslides 1*, 113-122.
Hermanns, R.L., Blikra, L.H., Naumann, M., Nilsen, B., Panthi, K.K. & Stromeyer, D. 2006: Examples from multiple rock-slope collapses from Köfels (Ötz valley, Austria) and western Norway. *Engineering Geology 83*, 94-108.
Hermanns, R.L., Schleier, M., Böhme, M., Blikra, L.H., Gosse, J., Ivy-Ochs, S. & Hilger, P. 2017: Rock-avalanche activity in W and S Norway peaks after the retreat of the Scandinavian Ice Sheet. In Mikoš, M., Vílímek, V., Yin, Y. & Sassa, K. (eds): *Advancing Culture of Living with Landslides, Volume 5: Landslides in Different Environments*, 331-338. Springer: Berlin.
Hewitt, K., Clague, J.J. & Orwin, J.F. 2008: Legacies of catastrophic rock slope failures in mountain landscapes. *Earth-Science Reviews 87*, 1-38.

Heyman, J., Stroeven, A.P., Harbor, J.M., & Caffee, M.W. 2011: Too young or too old: Evaluating cosmogenic exposure dating based on an analysis of compiled boulder exposure ages. *Earth and Planetary Science Letters 302*, 71-80.

Hicks, E.C., Bungum. H. & Lindholm, C.D. 2000: Seismic activity, inferred crustal stresses and seismotectonics in the Rana region, Northern Norway. *Quaternary Science Reviews 19*, 1423-1436.

Hipp, T., Etzelmüller, B. & Westermann, S. 2014: Permafrost in alpine rock faces from Jotunheimen and Hurrungane, southern Norway. *Permafrost and Periglacial Processes 25*, 1-13.

Holm, K., Bovis, M. & Jakob, M. 2004: The landslide response of alpine basins to post-Little Ice Age glacial thinning and retreat in southwestern British Columbia. *Geomorphology 57*, 201-216.

Hormes, A., Blaauw, Dahl, S.O., Nesje, A. & Possnert, G. 2009: Radiocarbon wiggle-match dating of proglacial lake sediments – implications for the 8.2 ka event. *Quaternary Geochronology 4*, 267-277.

Huggel, C., Salzmann, N., Allen, S., Caplan-Auerbach, J., Fischer, L., Haeberli, W., Larsen, C., Schneider, D. & Wessel, R. 2010: Recent and future warm extreme events and high-mountain slope stability. *Philosophical Transactions of the Royal Society A 368*, 2435-2459.

Huggel, C., Clague, J.J. & Korup, O. 2012: Is climate change responsible for changing landslide activity in high mountains? *Earth Surface Processes and Landforms 37*, 77-91.

Hughes, A.L.C., Gyllencreutz, R., Lohne, Ø., Mangerud, J. & Svendsen, J.L. 2016: The last Eurasian ice sheets – a chronological database and time-slice reconstruction, DATED-1. *Boreas 45*, 1-45.

Hungr, O. & Evans, S.G. 2004: Entrainment of debris in rock avalanches: analysis of a long run-out mechanism. *Geological Society of America Bulletin 116*, 1240-1252.

Isaksen, K., Hauck, C., Gudevang, E., Ødegård, R.S. & Sollid, J.L. 2002: Mountain permafrost distribution in Dovrefjell and Jotunheimen, southern Norway, based on BTS and DC restivity tomography data. *Norsk Geografisk Tidsskrift 56*, 122-136.

Ivy-Ochs, S., Poschinger, A.v., Synal, H. & Maisch, M. 2009: Surface exposure dating of the Flims landslide, Graubünden, Switzerland. *Geomorphology 103*, 104-112.

Jansen, E., Andersson, C., Moros, M., Nisancioglu, K.H., Nyland, B.F. & Telford, R.J. 2008: The early to mid-Holocene thermal optimum in the North Atlantic. In Battarbee, R.W. & Binney, H.A. (eds): *Natural Climate Variability and Global Warming: a Holocene Perspective*, 128-137. Wiley-Blackwell: Chichester.

Jarman, D. 2006: Large rock slope failures in the Highlands of Scotland: characterization, causes and spatial distribution. *Engineering Geology 83*, 161-182.

Johnson, B.G., Smith, J.A. & Diemer, J.A. 2017: A chronology of post-glacial landslides suggests that slight increases in precipitation could trigger a disproportionate geomorphic response. *Earth Surface Processes and Landforms 42*, 2223-2239.

Karlén, W. & Matthews, J.A. 1992: Reconstructing Holocene glacier variations from glacial lake sediments: studies from Nordvestlandet and Jostedalsbreen-

Jotunheimen, southern Norway. *Geografiska Annaler Series A Physical Geography 74*, 327-348.

Keefer, D.K. 2002: Investigating landslides caused by earthquakes – a historical review. *Surveys in Geophysics 23*, 473-510.

Keefer, D.K. 2015: Landslides generated by earthquakes: immediate and long-term effects. In Owen, L.A. (ed.) *Tectonic Geomorphology*, 250-266. Elsevier, Amsterdam. [Treatise on Geomorphology, Volume 5]

Korup, O., Clague, J.J., Hermanns, R.L., Hewitt, K., Strom, A.L., & Weidinger, J.T. 2007: Giant landslides, topography, and erosion. *Earth and Planetary Science Letters 261*, 578-589

Krautblatter, M. & Leith, K. 2015: Glacier- and permafrost-related slope instabilities. In Huggel, C., Carey, M., Clague, J.J. & Kääb, A. (eds): *The High-Mountain Cryosphere: Environmental Changes and Human Risks*, 147-165. Cambridge University Press, Cambridge.

Krautblatter, M., Funk, D. & Guenzel, F. 2013: Why permafrost rocks become unstable: a rock-ice-mechanical model in time and space. *Earth Surface Processes and Landforms 38*, 876-887.

Kukkonen, I.T., & Šafanda, J. 2001: Numerical modelling of permafrost in bedrock in northern Fennoscandia during the Holocene. *Global and Planetary Change 29*, 259-273.

Lang, A., Moya, J. Corominas, J., Schrott, L. & Dikau, R. 1999: Classic and new dating methods for assessing the temporal occurrence of mass movements. *Geomorphology 30*, 33-52.

Lau, K.-M., & Weng, H. 1995: Climate signal detection using wavelet transform: How to make a time series sing. *Bulletin of the American Meteorological Society 76*, 2391-2402.

Lidmar-Bergström, K., Ollier, C. & Sulebak, J.R. 2000: Landforms and uplift history of southern Norway. *Global and Planetary Change 24*, 211-231.

Lilleøren, K.S., Etzelmüller, B., Schuler, T.V., Ginås, K. & Humlum, O. 2012: The relative age of permafrost – estimation of Holocene permafrost limits in Norway. *Global and Planetary Change 92–93*, 209–223.

Lu, M., Pebesma, E., Sanchez, A. & Verbesselt, J. 2016: Spatio-temporal change detection from multidimensional arrays: Detecting deforestation from MODIS time series. *ISPRS Journal of Photogrammetry and Remote Sensing 117*, 227-236.

Luckman, B.L. 2004: Rockfall. In Goudie, A.S. (ed.): *Encyclopedia of Geomorphology, Volume 2*, 882. Routledge: London.

Lutro, O. & Tveten, E. 1996: *Geologiske kart over Norge, bergrunnskart Årdal,* 1:250,000. Norges Geologiske Undersøkelse, Trondheim.

Lysså A., Knies, J. & Larsen E. 2008: Kunskap om istider og landformer – nøkkelen til forståelsen av klimavariasjoner. *Gråsteinen 12*, 41-57. [Norges geologiske undersøkelse]

Mangerud, J., Gyllencreutz, R., Lohne, Ø. & Svendsen, J.I. 2011: Glacial history of Norway. In: Ehlers, J., Gibbard, P.L. & Hughes, P.D. (eds): *Quaternary glaciations – extent and chronology: a closer look*, 279-298. Elsevier: Amsterdam.

Marc, O., Hovius, N., Meunier, P., Uchida, T. & Hayashi, S. 2015: Transient changes of landslide rates after earthquakes. *Geology 43*, 883-886.

MATLAB 2015. *MATLAB Version 8.5,* The MathWorks, Inc., Natick MA.

Matsuoka, N. & Murton, J. 2008: Frost weathering: recent advances and future

directions. *Permafrost and Periglacial Processes 19*, 195-210.

Matthews, J.A. 1991: The late Neoglacial ('Little Ice Age') glacier maximum in southern Norway: new ^{14}C-dating evidence and climatic implications. *The Holocene 1*, 219-133.

Matthews, J.A. 2005: 'Little Ice Age' glacier variations in Jotunheimen, southern Norway: a study in regionally-controlled lichenometric dating of recessional moraines with implications for climate and lichen growth rates. *The Holocene 15*, 1-19.

Matthews, J.A. & Dresser, P.Q. 2008: Holocene glacier variation chronology of the Smørstabbtindan massif, Jotunheimen, southern Norway, and the recognition of century- to millennial-scale European Neoglacial events. *The Holocene 18*, 181-201.

Matthews, J.A. & McEwen, L.J. 2013: High-precision Schmidt-hammer exposure-age dating (SHD) of flood berms, Vetlestølsdalen, alpine southern Norway: first application and some methodological issues. *Geografiska Annaler Series A Physical Geography* 95, 185-194.

Matthews, J.A. & Owen, G. 2008: Endolithic lichens, rapid biological weathering and Schmiodt hammer R-values on recently exposed rock surfaces: Storbreen glacier foreland, Jotunheimen, Norway. *Geografiska Annaler Series A Physical Geography* 90, 287-297.

Matthews, J.A & Owen, G. 2010: Schmidt-hammer exposure-age dating: developing linear age-calibration curves using Holocene bedrock surfaces from the Jotunheimen–Jostedalsbreen regions of southern Norway. *Boreas 39*, 105-115.

Matthews, J.A. & Owen, G. 2011: Holocene chemical weathering, surface lowering and rock weakening rates on glacially eroded bedrock surfaces in an alpine periglacial environment, Jotunheimen, Norway. *Permafrost and Periglacial Processes 22*, 279-290.

Matthews, J.A. & Seppålå, M. 2005: Holocene colluvial chronology in the sub-arctic esker landscape at Kuttanen, Finnisj Lapland: kettleholes as geo-ecological archives of interactions amongst fire, vegetation, soil, climate and geomorphological instability. *Boreas 44*, 343-367.

Matthews, J.A. & Shakesby, R.A., 1984: The status of the 'Little Ice Age' in southern Norway: relative-age dating of Neoglacial moraines with Schmidt hammer and lichenometry. *Boreas 13*, 333-346.

Matthews, J.A. & Shakesby, R.A. 2004: A twentieth-century neoparaglacial rock topple on a glacier foreland, Ötztal Alps, Austria. *The Holocene 14*, 454-458.

Matthews, J.A. & Vater, A.E. 2015: Pioneer zone geo-ecological change: observations from a chronosequence on the Storbreen glacier foreland, Jotunheimen, southern Norway. *Catena 135*, 219-230.

Matthews, J.A. & Wilson, P. 2015: Improved Schmidt-hammer exposure ages for active and relict pronival ramparts in southern Norway, and their palaeoenvironmental implications. *Geomorphology 246*, 7-21.

Matthews, J.A. & Winkler, S. 2011: Schmidt-hammer exposure-age dating (SHD): application to early Holocene moraines and a reappraisal of the reliability of terrestrial cosmogenic-nuclide dating (TCND) at Austanbotnbreen, Jotunheimen, Norway. *Boreas 40*, 256-270.

Matthews, J.A., Brunsden, D., Frenzel, B., Gläser, B. & Weiss, M.M. (eds) 1997: *Rapid Mass Movement as a Source of Climatic Evidence for the Holocene.* Gustav Fisher Verlag, Stuttgart, 446 pp. [*Paläoklimaforschung* Volume 19]

Matthews J.A., Berrisford, M.S., Dresser, P.Q., Nesje, A., Dahl, S.O., Bjune, A.E., Bakke, J., Birks, H.J.B., Lie, Ø., Dumayne-Peaty, L. & Barnett, C. 2005: Holocene glacier history of Bjørnbreen and climatic reconstruction in central Jotunheimen, southern Norway, based on proximal glaciofluvial stream-bank mires. *Quaternary Science Reviews 24*, 67-90.

Matthews, J.A., Dahl, S.O., Dresser, P.Q., Berrisford, M.S., Lie, Ø., Nesje, A. & Owen, G. 2009: Radiocarbon chronology of Holocene colluvial (debris-flow) activity at Sletthamn, Jotunheimen, southern Norway: a window on the changing frequency of extreme climatic events and their landscape impact. *The Holocene 19*, 1107-1129.

Matthews, J.A., Nesje, A. & Linge, H. 2013: Relict talus-foot rock glaciers at Øyberget, upper Ottadalen, southern Norway: Schmidt hammer exposure ages and palaeoenvironmental implications. *Permafrost and Periglacial Processes 24*, 336-346.

Matthews, J.A., Winkler, S. & Wilson, P. 2014: Age and origin of ice-cored moraines in Jotunheimen and Breheimen, southern Norway: insights from Schmidt-hammer exposure-age dating. *Geografiska Annaler Series A Physical Geography 96*, 531-548.

Matthews, J.A., McEwen, L.J. & Owen, G. 2015: Schmidt-hammer exposure-age dating (SHD) of snow-avalanche impact ramparts in southern Norway: approaches, results and implications for landform age, dynamics and development. *Earth Surface Processes and Landforms 40*, 1705–1718.

Matthews, J.A., Owen, G., Winkler, S., Vater, A.E., Wilson, P., Mourne, R.W. & Hill, J.L. 2016: A rock-surface microweathering index from Schmidt hammer R-values and its preliminary application to some common rock types in southern Norway. *Catena 143*, 35-44.

Matthews, J.A., Wilson, P. & Mourne, R.W. 2017: Landform transitions from pronival ramparts to moraines and rock glaciers: a case study from the Smørbotn cirque, Romsdalsalpane, southern Norway. *Geografiska Annaler Series A Physical Geography 96*, 15-37.

McCarroll, D. 1987: The Schmidt hammer in geomorphology: five sources of instrument error. *British Geomorphological Research Group Technical Bulletin 36,* 16-27.

McCarroll, D. 1994: The Schmidt hammer as a measure of degree of rock surface weathering and terrain age. In Beck, C. (ed.) *Dating in Exposed and Surface Contexts*, 29-45. University of New Mexico Press, Albuquerque.

McColl, S.T. 2012: Paraglacial rock-slope stability. *Geomorphology 153-154*, 1-16.

McColl, S.T. & Davies T.R.H. 2012: Large ice-contact slope movements, glacial buttressing, deformation and erosion. *Earth Surface Processes and Landforms 38*, 1102-1115.

McPhillips, D., Bierman, P.R. & Rood, D.H. 2014: Millennial-scale record of landslides in the Andes consistent with earthquake trigger. *Nature Geoscience 7*, 925-930.

Mercier, D. 2008: Paraglacial and paraperiglacial land systems: concepts, temporal scales and spatial distribution. *Géomorphologie: Relief, Processus, Environnement 14*, 223-233.

Mercier, D., Coquin, J., Feuillet, T., Decaulne, A., Cossart, E., PallJónsson, H. & Sæmundsson, Þ. 2017: Are Icelandic rock-slope failures paraglacial? Age evaluation of seventeen rock-slope failures in the Skagafjörður area based on geomorphological stacking, radiocarbon dating and tephrochronology.

Geomorphology 296, 45-58.
Messenzehl, K. & Dikau, R. 2017: Structural and thermal controls of rockfall frequency and magnitude within rockwall-talus systems (Swiss Alps). *Earth Surface Processes and Landforms 42*, 1963-1981.
Moen, A. 1999: *National Atlas of Norway: Vegetation*. Norwegian Mapping Authority, Hønefoss.
Moreiras, S.M., Hermanns, R.L. & Fauqué, L. 2015: Cosmogenic dating of rock avalanches constraining Quaternary stratigraphy and regional neotectonics in the Argentine Central Andes (32°S). *Quaternary Science Reviews 112*, 45-58.
Moses, C., Robinson, D. & Barlow, J. 2014: Methods for measuring rock surface weathering and erosion: a critical review. *Earth-Science Reviews 135*, 141-161.
Murari, M.K., Owen, L.A., Dortch, J.M., Caffee, M.W., Dietsch, C., Fuchs, M., Haneberg, W.C., Sharma, M.C. & Townsend-Small, A. 2014: Timing and climatic drivers for glaciation across monsoon-influenced regions of the Himalayan-Tibetan orogen. *Quaternary Science Reviews 88*, 159-182.
Murphy, B. 2015: Coseismic landslides. In Davies, T. (ed.) *Landslide Hazards, Risks, and Disasters,* 91-129. Elsevier, Amsterdam.
Murton, J. B., Peterson & Ozouf, J.-C. 2006: Bedrock fracture in cold regions. *Science 314*, 1127-1129.
Nesje, A. 2009: Late Pleistocene and Holocene alpine glacier fluctuations in Scandinavia. *Quaternary Science Reviews 28*, 2119-2136.
Nesje, A. & Dahl, S.O. 2001: The Greenland 8200 cal. yr BP event detected in loss-on-ignition profiles in Norwegian lacustrine sediment sequences. *Journal of Quaternary Science 16*, 155-166.
Nesje, A., Bakke, J., Dahl, S.O., Lie, Ø. & Matthews, J.A. 2008: Norwegian glaciers in the past, present and future. *Global and Planetary Change 60*, 10-27.
Nesje, A., Blikra, L. & Anda, E. 1994: Dating rockfall-avalanche deposits from degree of rock-surface weathering by Schmidt-hammer tests: a study from Norangsdalen, Sunnmøre, Norway. *Norsk Geologiske Tidsskrift 74,* 108-113.
Nicholson, D.T. 2008: Rock control inmicroweathering of bedrock surfaces in a periglacial environment. *Geomorphology 101*, 655-665.
Nicholson, D.T. 2009: Holocene microweathering rates and processes on ice-eroded bedrock, Røldal area, Hardangervidda, southern Norway. In: Knight, J. & Harrison, S. (eds.): *Periglacial and Paraglacial Processes and Environments*, 29-49. Geological Society, Special Publication 320. Geological Society of London, Bath.
Ødgård, R.S., Sollid, J.L. & Liestøl, O. 1992: Ground temperature measurements in mountain permafrost, Jotunheimen, southern Norway. *Permafrost and Periglacial Processes 3*, 231-234.
Ødgård, R.S., Nesje, A., Isaksen, K., Andreassen, L.M., Eiken, T., Scwikowski, M. & Uglietti, C. 2017: Climate change threatens archaeologically significant ice patches: insights into their age, internal structure, mass balance and climate sensitivity. *The Cryosphere 11*, 17-32.
Oerlemans, J. 2005: Extracting a climate signal from 169 glacier records. *Science 308*, 675-677.
Olesen,O., Dehls, J., Bugum, H., Riis, F., Hicks, E., Lindholm, C., Blikra, L.H., Fjeldskaar, W., Olsen, L., Longva, O., Faleide, J.I., Bockmann, L., Rise, L., Roberts, D., Braathen, A. & Brekke, H. 2000: *NEONOR: Neotectonics in Norway, Final Report.* Norges Geologiske Undersøkelse, Trondheim. [Report

2000.002]
Owen, G., Hiemstra, J.F., Matthews, J.A. and McEwen, L.J. 2010: Landslide-glacier interaction in a neoparaglacial setting at Tverrbytnede, Jotunheimen, southern Norway. *Geografiska Annaler Series A Physical Geography 92*, 421-436.
Pánek, T. 2014: Recent progress in landslide dating: a global overview. *Progress in Physical Geography 39*, 168-198.
Paus, A. & Haugland, V. 2017: Early- to mid-Holocene forest-line and climate dynamics in southern Scandes mountains inferred from contrasting megafossil and pollen data. *The Holocene 27*, 361-383.
Penna, I.M., Hermanns, R.L., Niedermann, S & Folguera, A. 2011: Multiple slope failures associated with neotectonic activity in the Southern Central Andes (37°-37° 30'S), Patagonia, Argentina. *Geological Society of America Bulletin 123*, 1880-1895.
Phillips, M., Wolter, A., Lüthi, R., Amann, F., Kenner, R. & Bühler, Y. 2017: Rock slope failure in a recently deglaciated permafrost rock wall at Piz Kesch (Eastern Swiss Alps), February 2014. *Earth Surface Processes and Landforms 42*, 426-438.
Prager, C., Zangerl, C., Patzelt, G. & Brandner, R. 2008: Age distribution of fossil landslides in the Tyrol (Austria) and its surrounding areas. *Natural Hazards and Earth System Sciences 8*, 377-407.
Prager, C., Ivy-Ochs, S., Ostermann, M., Synal, H.-A. & Patzelt, G. 2009: Geology and radiometric ^{14}C-, ^{36}Cl- and Th/U-dating of the Fernpass rockslide (Tyrol, Austria). *Geomorphology 103*, 93-103.
Proceq 2004: *Operating instructions. Betonprüfhammer N/NR-L/LR.* Proceq SA: Schwerzenbach.
Rapp, A. 1960a: Talus slopes and mountain walls at Templefjorden, Spitzbergen. *Norsk Polarinstitutt Skrifter 119*, 1-96.
Rapp, A. 1960b: Recent development of mountain slopes in Kärkevagge and surroundings, northern Scandinavia. *Geografiska Annaler 42*, 65-200.
Reimer, P.J., Bard, E., Bayliss, A., Beck, J.W., Blackwell, P.G., Ramsey, C.B., Buck, C.E., Cheng, H., Edwards, R.L., Friedrich, M. & Grootes, P.M. 2013: IntCal13 and Marine13 radiocarbon age calibration curves 0–50,000 years cal BP. *Radiocarbon 55*, 1869-1887.
Renssen, H., Seppä, H., Crosta, X., Goose, H. & Roche, D.M. 2012: Global characterization of the Holocene Thermal Maximum. *Quaternary Science Reviews 48*, 7-19.
Sánchez, S.J., Mosquera, D.F & Vidal Romaní, J.R. 2009: Assessing the age-weathering correspondence of cosmogenic ^{21}Ne dated Pleistocene surfaces by the Schmidt hammer. *Earth Surface Processes and Landforms 34*, 1121-1125.
Sandøy, G., Oppikofer, T. & Nilsen, B. 2017: Why did the 1756 Tjellefonna rockslide occur? A back-analysis of the largest historic rockslide in Norway. *Geomorphology 289*, 78-95.
Sass, O. & Wollny, K. 2001: Investigations regarding alpine talus slopes using ground-penetrating radar (GPR) in the Bavarian Alps, Germay. *Earth Surface Processes and Landforms 26*, 1071-1086.
Scarpozza, C. 2016: Evidence of paraglacial and paraperiglacial crisis in Alpine sediment transfer since the last glaciation (Tincino, Switzerland). *Quaternaire 27*, 139-155.
Schleier, M., Hermanns, R.L., Rohn, J. & Gosse J.C. 2015: Diagnostic characteristics and paleodynamics of supraglacial rock avalanches, Innerdalen, Western

Norway. *Geomorphology 245*, 23-39.
Schleier, M., Hermanns, R.L., Goose, J.C., Oppikofer, T., Rohn, J. & Tønnesen, J.F. 2017: Subaqueous rock-avalanche deposits exposed by post-glacial isostatic rebound, Innfjorddalen, Western Norway. *Geomorphology 289*, 117-133.
Seppä, H., Bjune, A.E., Telford, R.J., Birks, H.J.B. Birks & Veski, S. 2009: Last nine-thousand years of temperature variability in Northern Europe. *Climate Past 5*, 523-535.
Shakesby, R.A. 2014: Rockfall. In Matthews, J.A., Barrow, C.J., Boyd, D.S., Caseldine, C.J., Ficken, K.J., Innes, J.L., Nortcliff, S., Owen, G., Pike, J., Shakesby, R.A., Walsh, R.P.D. & Wheeler, D.A. (eds): *Encyclopedia of Environmental Change, Volume 3*, 939-940. SAGE, London.
Shakesby, R.A., Matthews, J.A. & Owen, G. 2006: The Schmidt hammer as a relative-age dating tool and its potential for calibrated-age dating in Holocene glaciated environments. *Quaternary Science Reviews 25*, 2846-2867.
Shakesby, R.A., Matthews, J.A., Karlén, W. & Los, S. 2011: The Schmidt hammer as a Holocene calibrated-age dating technique: testing the form of the R-value–age relationship and defining predicted errors. *The Holocene 21*, 615-628.
Soldati, M., Corsini, A. & Pasuto, A. 2004: Landslides and climate change in the Italian Dolomites since the Late Glacial. *Catena 55*, 141-161.
Stahl, T., Winkler, S., Quigley, M., Bebbington, M., Duffy, B. & Duke, D. 2013: Schmidt hammer exposure-age dating (SHD) of late Quaternary fluvial terraces in New Zealand. *Earth Surface Processes and Landforms 38*, 1838-1850.
Stock, G.M. & Uhrhammer, R.A. 2010: Catastrophic rock avalanche 3600 BP from El Capitan, Yosemite Valley, California. *Earth Surface Processes and Landforms 35*, 941-951.
Stoffel, M. & Huggel, C. 2012: Effects of climate change on mass movements in mountain environments. *Progress in Physical Geography 36*, 421-439.
StormTech 2012: *Tech Sheet 1: porosity of structural backfill.* [http://www.stormtech.com/download_files/pdf/techsheet1.pdf]
Stroeven, A.P., Hättestrand, C., Kleman, J., Heyman, J., Fabel, D., Fredin, O., Goodfellow, B.W., Harbor, J.M., Jansen, J.D., Olsen, L., Caffee, M.W., Fink, D., Lundqvist, J., Rosqvist, G.C., Strömberg, B. & Jansson, K.N. 2016: Deglaciation of Fennoscandia. *Quaternary Science Reviews 147*, 91-121.
Tomkins, M.D., Dortch, J.M., & Hughes, P.D. 2016: Schmidt Hammer exposure dating (SHED): Establishment and implications for the retreat of the last British Ice Sheet. *Quaternary Geochronology 33*, 46-60.
Tomkins, M.D., Huck, J.J., Dortch, J.M., Hughes, P.D., Kirkbride, M.P. & Barr, I.D. 2018a: Schmidt hammer exposure dating (SHED): calibration procedures, new exposure age data and an online calculator. *Quaternary Geochronology 44*, 55-62.
Tomkins, M.D., Dortch, J.M., Hughes, P.D., Huck, J.J., Stimson, A.G., Delmas, M., Calvet, M. & Pallàs, R. 2018b: Schmidt hammer exposure dating (SHED): rapid age assessment of glacial landforms in the Pyrenees. *Quaternary Research* (in press).
Tomkins, M.D., Dortch, J.M., Hughes, P.D., Huck, J.J., Tonkin, T., & Barr, I.D. 2018c: Timing of glacial retreat in the Wicklow Mountains, Ireland, conditioned by glacier size and topography. *Journal of Quaternary Science* (in press).

Torrence, C., & Compo, G.P. 1998: A Practical Guide to Wavelet Analysis. *Bulletin of the American Meteorological Society 79*, 61-78

Trauth. M.H., Alonso, R.A., Haselton, K.R., Hermanns, R.L. & Strecker, M.R. 2000: Climate change and mass movements in the NW Argentine Andes. *Earth and Planetary Science Letters 179*, 243-256.

Trauth, M.H., Bookhagen, B., Marwan, N. & Strecker, M.R. 2003. Multiple landslide clusters record Quaternary climate changes in the northwestern Argentine Andes. *Palaeogeography, Palaeoclimatology, Palaeoecology 194*, 109-121.

Väliranta, M., Salonen, J.S., Heikkilä, M., Amon, L., Helmens, K., Klimaschewski, A., Kuhry, P., Kultti, S., Paska, A., Shala, S., Veski, S. & Birks, H.H. 2015: Plant macrofossil evidence for an early onset of the Holocene summer thermal maximum in northernmost Europe. *Nature Comunications* doi:10.1038/ncomms7809.

Velle, G., Bjune, A.E., Larsen, J & Birks, H.J.B. 2010: Holocene climate and environmental history of Brurskardstjørni, a lake in the catchment of Øvre Heimdalsvatnet, south-central Norway. *Hydrobiologia 642*, 13–34.

Viles, H., Goudie, A., Grabb, S. & Lalley, J. 2011: The use of the Schmidt hammer and Equotip for rock hardness assessment in geomorphology and heritage science: a comparative analysis. *Earth Surface Processes and Landforms 36*, 320-333.

Walker, M.J.C., Berkelhammer, M., Björk, S., Cwynar, L.C., Fisher, D.A., Long, A.J., Lowe, J.J., Newnham, R.M., Rasmussen, S.O. & Weiss, H. 2012: Formal subdivision of the Holocene Series/Epoch: a discussion paper by a Working Group of INTIMATE (Integration of ice-core, marine and terrestrial records) and the Subcommission on Quaternary Stratigraphy (International Commission on Stratigraphy). *Journal of Quaternary Science 27*, 649-659.

Wanner, H., Solomina, O., Grosjean, M., Ritz, S. & Jetel, M. 2011: Structure and origin of Holocene cold events. *Quaternary Science Reviews 30*, 3109-3123.

Wilson, P. 2009: Storurdi: a late Holocene rock-slope failure (Sturzstrom) in the Jotunheimen, southern Norway. *Geografiska Annaler Series A Physical Geography 91*, 47-58.

Wilson, P. & Matthews, J.A. 2016: Age assessment and implications of late Quaternary periglacial and paraglacial landforms on Muckish Mountain, northwest Ireland, based on Schmidt-hammer exposure-age dating (SHD). *Geomorphology 270*, 134-144.

Wilson, P., Matthews, J.A. & Mourne, R.W. 2017: Relict blockstreams at Insteheia, Valldalen-Tafjorden, southern Norway: their nature and Schmidt-hammer exposure age. *Permafrost and Periglacial Processes 28*: 286-297.

Winkler, S. 2009: First attempt to combine terrestrial cosmogenic nuclide (^{10}Be) and Schmidt hammer relative-age dating: Strauchon Glacier, Southern Alps, New Zealand. *Central European Journal of Geosciences 1*, 274-290.

Winkler, S. & Matthews, J.A. 2010: Holocene glacial chronologies: are 'high resolution' global and interhemispherical comparisons possible? *The Holocene 20*, 1137-1147.

Winkler, S. & Matthews, J.A. 2014: Comparison of electronic and mechanical Schmidt hammers in the context of exposure-age dating: are Q- and R-values interconvertible? *Earth Surface Processes and Landforms 39*, 1128-1136.

Winkler S. & Matthews, J.A. 2016: Inappropriate instrument calibration for Schmidt-hammer exposure-age dating (SHD) – A comment on Dortch et al., Quaternary Geochronology 35 (2016), 67-68. *Quaternary Geochronology 36*,

102-103.
Winkler, S., Chinn, T., Gärtner-Roer, I., Nussbaumer, U., Zemp, M. & Zumbühl, H.J. 2010: An introduction to mountain glaciers as climatic indicators with spatial and temporal diversity. *Erdkunde 64*, 97-118.
Winkler, S., Matthews, J.A., Mourne, R.W. & Wilson, P. 2016: Schmidt-hammer exposure ages from periglacial patterned ground (sorted circles) in Jotunheimen, Norway, and their interpretive problems. *Geografiska Annaler Series A Physical Geography 98*, 265-285.
Zerathe, S., Lebourg, T., Braucher, R. & Bourlès, D. 2014: Mid-Holocene cluster of large-scale landslides revealed in the Southwestern Alps by ^{36}Cl dating. Insight on an Alpine-scale landslide activity. *Quaternary Science Reviews 90*, 106-127.

FIGURE CAPTIONS

Fig. 1. Location map: numbers and open circles identify the studied SRSFs; sites of control points are shown by crosses.

Fig. 2. Photographs of selected small rock-slope failures (SRSFs): (A) No. 23, Gravdalen; (B) Nos 7 and 8, Leirdalen; (C) Nos 34-36, Bjørndalen; (D) No. 7, Sognefjell; (E) and (F) No. 22, Gravdalen (also the site of a young control point).

Fig. 3. Schematic of the fan-scar-cliff comparison tests with expected differences in mean R-values between fan boulders, scar bedrock surfaces, unfailed cliffs, and rock surfaces used as younger and older control-point surfaces. Expectations apply to single-event SRSF events without the possible complications discussed in the text.

Fig. 4. Frequency distributions of four SRSF characteristics: (A) fan volume; (B) altitude; (C) aspect; (D) mean R-value. Eight sites in gabbroic gneiss (Sognefjell) are differentiated by solid black shading from 84 sites in pyroxene-granulite gneiss.

Fig. 5. Calibration curves and calibration equations for (A) pyroxene-granulite gneiss and (B) gabbroic gneiss. Note that both calibration curves are based on two control points of known age (25 years and 9700 years) using data presented in Table 3.

Fig. 6. Holocene SHD chronologies of SRSF activity for Jotunheimen: (A) individual SHD dates with their 95% confidence intervals in the different subregions; (B) age-frequency distributions of SRSF events at the regional level using 2000-yr, 1000-yr, 500-yr and 200-yr time intervals; (C) weighted age-frequency distribution with age-frequency curve defined by binomial smoothing; (D) variation in the magnitude of SRSF events based on rock volume using 200-year time intervals. Vertical bands (numbered) are the 4 modes in the weighted age-frequency distribution suggesting phases of enhanced regional SRSF activity.

Fig. 7. Probability density function analysis of SRSF activity for Jotunheimen: (A) histogram and KS density PDE; (B) individual Gaussian age distributions (n = 5), the sum of which integrates to the cumulative PDE with a model fit that is graphically indistinguishable from from the PDE model. The number of ages listed for each Gaussian age distribution (#) exceeds the total number of SRSF events identified in Jotunheimen as some ages contribute to >1 Gaussian distribution; (C) peak Gaussian numerical ages and 1σ uncertainties for the five individual Gaussian age distributions plotted against the peak probability density (PPD). The PPD scales with the number and spatial clustering of individual ages. Reported RSF volumes are based on the sum of individual SRSF volumes (m^3) which comprise each Gaussian age distribution; (D) distribution of SRSF ages, sorted by oldest to youngest. The 42 SRSF events which account for the dominant mode at 4.50 ± 1.42 ka (within 1σ) are highlighted.

Fig. 8. Change detection and related analyses: (A) cumulative sum change detection graph showing positive (blue) and negative (orange) changes and statistically significant departures (> 2σ) from the background SRSF frequency; (B) modelled permafrost depth in Fennoscandia (5% porosity) from Kukkonen & Šafanda (2001), subdivided into five distinct phases; (C) results of discreet Meyer wavelet analysis, showing the lowest frequency decomposed signal (d_6).

Fig. 9. Models for different patterns and causes of Holocene variations in RSF frequency and/or magnitude: (1) continuity-of-activity; (2) intermittent-earthquakes; (3) deglaciation-close-tracking; (4) deglaciation-lagging; (5) cool/wet-climate-response; and (6) the new thermally-driven permafrost-degradation model proposed in this study for SRSFs in Jotunheimen. The subdivisions of the Holocene shown are those proposed by Walker et al. (2012).

Fig. 10. Relationships between SRSF frequency in Jotunheimen and proxy climatic records: (A) temporal variations in SRSF frequency from Fig. 6C; (B) pollen-based reconstruction of annual air temperature for Northern Europe expressed as deviations from the mean (Seppä et al., 2009); (C) mean summer air temperature deviations from present in the Scandes Mountains based on pine tree-limit variations (Dahl and Nesje, 1996); (D) pollen-based July air temperature variations at Øvre Heimdalsvatnet, eastern Jotunheimen (Velle et al., 2010); (E) periods of above average air temperature (shaded) based on the GISP 2 Greenland ice core $\delta^{18}O$ record (Alley, 2004; Wanner et al., 2011); (F) periods of above average sea-surface temperatures in the North Atlantic Ocean (shaded) based on standardized stacked ice-rafted debris (IRD) records (Bond et al., 2001; Wanner, et al., 2011); (G) periods when glaciers in the Smørstabbtindan massif, Jotunheimen, were smaller than today (shaded) based on glaciolacustrine and glaciofluvial stratigraphy (Matthews and Dresser, 2008). Vertical bands indicate phases of enhanced regional SRSF frequency (as in Fig. 6).

SUPPLEMENTARY MATERIAL

(Caption to be included with figure)

Supplementary Fig.1: Full results of discreet Meyer wavelet analysis, showing all six decomposed signals (green), ranging from high (d_1) to low frequency (d_6), of which the latter represents the only single event structure of Holocene SRSF activity. The blue curves (a_1 - a_5) represent the cumulative aggregation of the decomposed signals (d_1 - d_6) where a_6 represents the mean background rate of SRSF occurrence (0.92 ± 0.20), which is identical to the Holocene mathematical mean. The sum of all decomposed signals results in a model (S_m) that is identical to the 100 yr bin histogram data (S_d).

Table 1. Data on the 92 small rock-slope failures (SRSFs) located in Jotunheimen: Leirdalen (Nos 1-29); Bjørndalen (30-40); Gravdalen (41-68); Høgvaglura (69-72); Visdalen (73-80); Veodalen (81-84); Sognefjell (85-92).
Abbreviations: L = fan length; W = fan width; V = fan volume; SD = standard deviation of R-values; C_s = error associated with the dated surface; C_c = error associated with the calibration equation; CI = confidence interval for the SHD age based on the total error (C_t).

No.	L (m)	W (m)	V (m^3)	Altitude (m a.s.l.)	Aspect	Mean R-value	SD	C_s (yr)	C_c (yr)	SHD age (yr ± 95% CI)	Sub-region
1	70	25	1050	1420	West	45.0	9.90	1047	513	7018 ± 1124	Leirdalen
2	80	20	960	1440	West	44.51	8.80	930	414	7277 ± 1018	
3	15	9	81	1400	West	39.69	9.47	1001	458	9833 ± 1101	
4	90	40	2160	1160	West	41.53	9.57	1012	445	8857 ± 1105	
5	15	8	72	1030	West	43.26	10.03	1060	426	7940 ± 1143	
6	90	20	1080	1160	West	43.62	10.23	1081	423	7749 ± 1161	
7	8	25	120	1140	West	44.69	9.41	995	412	7182 ± 1077	
8	30	25	450	1140	West	46.59	10.35	1094	392	6175 ± 1162	
9	8	8	38	1135	West	47.28	8.63	912	385	5809 ± 990	
10	15	25	225	1135	West	44.68	8.85	936	412	7187 ± 1022	
11	30	20	360	1200	North	52.38	10.07	1064	333	3105 ± 1115	
12	50	25	750	1425	North	46.49	8.63	912	394	6228 ± 994	
13	15	25	225	960	East	51.50	8.34	882	342	3572 ± 946	
14	50	25	750	955	East	49.79	10.74	1135	360	4478 ± 1191	
15	70	60	2520	950	East	49.28	8.73	923	365	4749 ± 992	
16	50	25	750	1290	West	48.29	9.98	1055	375	5273 ± 1120	
17	20	40	480	1320	West	54.10	9.90	1047	315	2193 ± 1093	
18	20	15	180	1320	West	57.53	10.15	1073	280	375 ± 1109	
19	30	40	720	1320	West	55.95	8.61	910	296	1213 ± 957	
20	18	14	151	1120	East	48.79	8.43	891	370	5008 ± 965	
21	16	8	77	1120	East	44.40	8.29	876	415	7336 ± 970	
22	25	14	210	1130	East	48.93	9.11	963	368	4934 ± 1031	
23	40	13	312	1170	East	41.30	9.14	966	447	8979 ± 1065	
24	25	15	225	1180	East	40.82	9.16	968	296	9233 ± 1012	
25	15	13	117	1180	East	43.37	9.49	1003	426	7882 ± 1090	
26	20	4	48	1190	East	44.86	8.70	920	410	7092 ± 1007	
27	12	8	58	1240	East	49.28	10.53	1113	365	4749 ± 1171	
28	20	4	48	1240	East	45.92	10.98	1160	399	6530 ± 1227	
29	22	4	53	1200	East	47.15	8.24	871	387	5878 ± 953	
30	90	16	864	1370	East	44.27	10.65	1126	416	7405 ± 1200	Bjørndalen
31	30	15	270	1380	East	44.62	10.10	1068	413	7219 ± 1145	
32	30	10	180	1380	East	52.60	8.62	911	331	2989 ± 922	
33	75	30	1350	1360	East	54.91	8.30	877	307	1764 ± 930	
34	30	15	270	1380	East	49.87	7.53	796	359	4436 ± 873	
35	30	12	216	1380	East	49.46	7.84	829	363	4653 ± 905	
36	20	30	360	1380	East	50.19	8.61	910	355	4266 ± 977	
37	80	35	1680	1330	South	50.23	9.57	960	355	4245 ± 1024	
38	25	15	225	1300	North	54.07	6.73	711	316	2209 ± 778	
39	50	30	900	1305	North	55.37	7.95	840	302	1520 ± 893	
40	25	25	375	1300	North	53.30	8.20	867	323	2617 ± 925	
41	55	20	660	1480	West	49.43	8.11	857	363	4669 ± 931	Gravdalen
42	15	35	315	1480	West	55.49	6.69	707	301	1456 ± 769	
43	65	15	585	1480	West	51.11	8.40	888	346	3778 ± 953	
44	60	15	540	1470	West	50.84	7.05	745	349	3922 ± 823	
45	65	25	975	1470	West	50.01	8.85	936	357	4362 ± 1001	
46	30	15	270	1460	West	52.57	7.97	843	331	3004 ± 905	
47	75	20	900	1460	West	53.03	6.27	663	326	2761 ± 739	
48	25	30	450	1430	South	50.01	7.00	740	357	4362 ± 822	
49	17	8	82	1440	South	49.10	8.45	893	367	4844 ± 964	
50	40	15	360	1440	South	49.71	7.72	816	360	4521 ± 892	
51	15	10	90	1440	South	50.38	7.78	822	356	4165 ± 896	
52	15	6	54	1400	South	56.21	7.38	780	293	1075 ± 834	
53	10	5	30	1400	South	57.99	6.22	658	275	131 ± 713	
54	7	8	34	1360	South	47.32	8.00	846	385	5788 ± 929	
55	10	6	36	1280	South	40.31	10.14	1072	457	9504 ± 1165	
56	12	5	36	1440	South	48.82	8.12	858	370	4992 ± 935	
57	6	5	18	1440	South	47.43	7.72	816	384	5729 ± 902	
58	8	8	38	1440	South	51.63	7.70	814	341	3503 ± 882	
59	4	5	12	1440	South	51.12	6.62	700	346	3773 ± 781	
60	7	4	17	1480	South	48.02	7.43	785	378	5416 ± 872	

61	20	5	60	1480	South	52.10	11.98	1266	336	3254 ± 1310	
62	14	8	67	1480	South	46.17	9.02	953	399	6397 ± 1033	
63	6	12	43	1430	South	48.74	8.09	855	370	5035 ± 932	
64	10	5	30	1430	South	46.99	7.65	809	388	5963 ± 897	
65	14	3	25	1460	South	49.91	8.38	886	358	4415 ± 956	
66	15	4	36	1520	South	51.92	8.34	882	338	3349 ± 944	
67	6	4	14	1540	South	49.95	9.74	1030	358	4393 ± 1090	
68	10	5	30	1540	South	49.37	7.08	748	364	4701 ± 832	
69	20	15	180	1550	East	50.13	7.74	818	356	4298 ± 892	Høgvaglura
70	50	12	360	1550	East	45.16	10.05	1062	407	6933 ± 1138	
71	20	10	120	1540	East	46.35	8.94	945	395	6302 ± 1024	
72	20	10	120	1540	East	42.10	11.92	1260	439	8555 ± 1334	
73	15	4	36	1420	East	47.03	11.08	1171	388	5941 ± 1234	Visdalen
74	15	9	81	1420	East	50.70	10.47	1107	350	3996 ± 1161	
75	10	4	24	1420	East	54.42	9.47	1001	312	2024 ± 1049	
76	25	10	150	1260	West	49.96	10.20	1078	358	4388 ± 1136	
77	40	20	480	1200	East	51.37	10.30	1089	343	3641 ± 1142	
78	70	30	1260	1200	East	52.98	8.86	937	327	2787 ± 992	
79	35	20	420	1200	East	51.57	7.93	838	341	3535 ± 905	
80	60	8	288	1190	East	50.31	10.75	1136	354	4202 ± 1190	
81	55	40	1320	1350	South	53.33	8.72	922	323	2601 ± 977	Veodalen
82	45	12	324	1340	South	54.33	9.34	987	313	2071 ± 1036	
83	50	25	750	1330	South	51.56	10.15	1073	341	3540 ± 1126	
84	45	40	1080	1330	South	49.46	10.60	1121	363	4653 ± 1178	
85	6	10	36	1375	East	37.17	11.29	900	239	9412 ± 931	Sognefjell
86	7	5	21	1425	South	38.53	8.82	703	244	8868 ± 744	
87	6	6	22	1425	South	39.42	10.43	831	247	8513 ± 868	
88	10	5	30	1430	South	41.38	9.86	786	255	7729 ± 826	
89	6	5	18	1430	South	40.73	9.47	755	253	7989 ± 796	
90	16	10	96	1450	South	38.26	8.83	704	243	8976 ± 745	
91	9	5	27	1435	West	42.33	10.03	800	259	7349 ± 840	
92	10	7	42	1370	East	36.95	9.14	729	238	9500 ± 766	

Table 2. Radiocarbon age control for deglaciation in the study area.

Location	Altitude (m. a.s.l.)	^{14}C age ± 1σ (years BP)	Calibrated age* (cal. years BP)	Reference
Leirdalen/Bjørndalen				
Lower Leirdalen	920	9089 ± 61	10426 – 10170 (94.8%)	Barnett et al. 2000
Bøverkinnhalsen	1020	8570 ± 60	9677 – 9475 (95.4%)	Nesje & Dahl 2001
Bjørndalen	1250	8760 ± 100	10066 – 9547 (77.1%)	Matthews et al. 2005
Sognefjell				
Nedre Hervavatnet	1287	8695 ± 75	9921 – 9530 (94.6%)	Hormes et al. 2009
Gjuvvatnet	1248	8885 ± 140	10247 – 9557 (95.4%)	Karlén & Matthews 1992

* Most probable range with probability in brackets

Table 3. Control point data: values used for calibration equations are indicated in bold. *Abbreviations:* Gneiss = pyroxene-granulite gneiss; Gabbro = gabbroic gneiss; Combined = data combined from two replicate sites; SD = standard deviation; CI = confidence interval; n = sample size.

Control point	Geology	Type	Age (years)	Mean R-value	SD	95% CI	n
Gravdalen	Gneiss	SRSF	25	58.22	6.29	0.72	300
Gravdalen	Gneiss	Road cut	25	58.15	6.56	0.75	300
Gravdalen	**Gneiss**	**Combined**	**25**	**58.19**	**6.42**	**0.52**	**600**
Sognefjell	**Gabbro**	**Road cut**	**25**	**60.65**	**7.26**	**0.83**	**300**
Gravdalen	Gneiss	Bedrock	9700	39.71	4.80	1.25	60
Leirdalen	Gneiss	Bedrock	9700	40.19	4.69	1.22	60
SE Smørstabbtindan	**Gneiss**	**Combined**	**9700**	**39.94**	**4.79**	**0.87**	**120**
Leirbreen	Gabbro	Bedrock	9700	35.78	2.84	0.74	60
Bøverbreen	Gabbro	Bedrock	9700	37.12	3.53	0.92	60
W Smørstabbtindan	**Gabbro**	**Combined**	**9700**	**36.45**	**3.25**	**0.59**	**120**

Table 4. Comparative R-values from fans, scars and unfailed cliffs associated with selected SRSFs. Further information on these six SRSFs are provided in Table 1.

No.	Fan			Scar			Unfailed cliff		
	Mean	SD	95% CI	Mean	SD	95% CI	Mean	SD	95% CI
5	43.26	10.03	2.00	41.34	7.75	1.55	42.20	7.86	1.57
46	51.63	7.70	1.54	51.32#	8.10	1.62	41.63†	9.20	1.83
47	51.12	6.62	1.32	54.05#	8.05	1.69	43.26†	10.19	2.03
51	37.17*	11.29	2.25	42.89	9.73	1.94	38.54	10.37	2.07
58	36.95*	9.14	1.82	43.99	10.44	2.08	40.68	12.30	2.45
81	49.96*	10.20	2.03	54.47#	8.07	1.60	43.38†	10.78	2.15

* Fan significantly different from scar ($p<0.05$)
\# Scar significantly different from unfailed cliff ($p<0.05$)
† Unfailed cliff significantly different from fan ($p<0.05$)

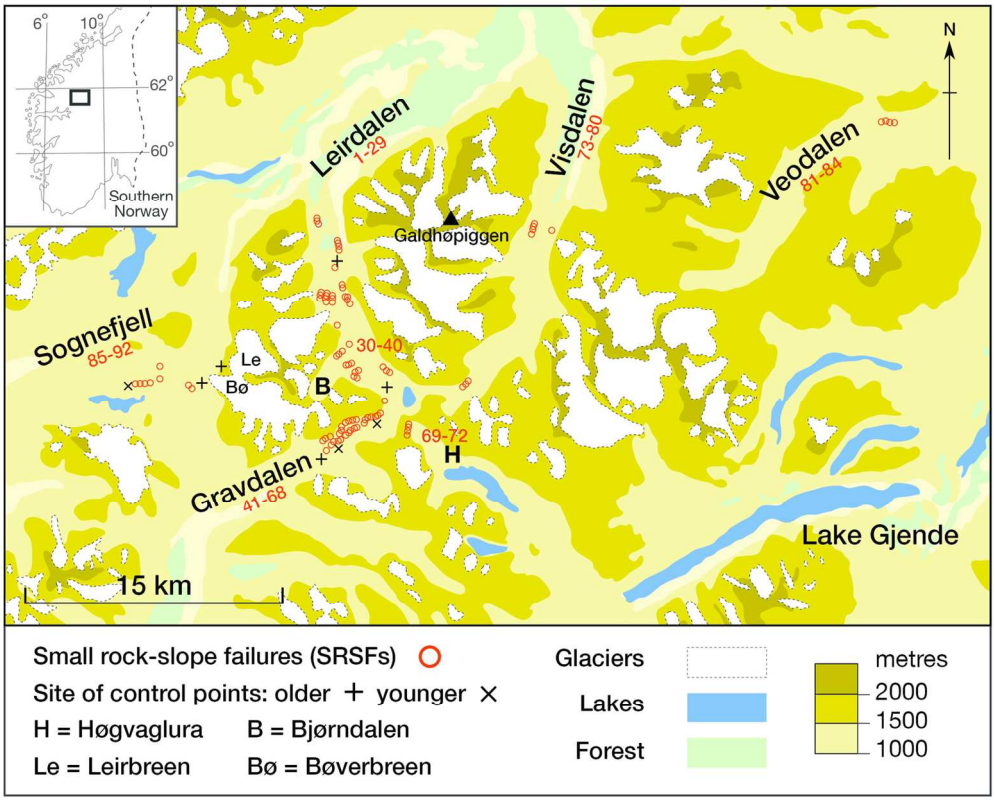

Fig. 1. Location map: numbers and open circles identify the studied SRSFs; sites of control points are shown by crosses.

143x115mm (300 x 300 DPI)

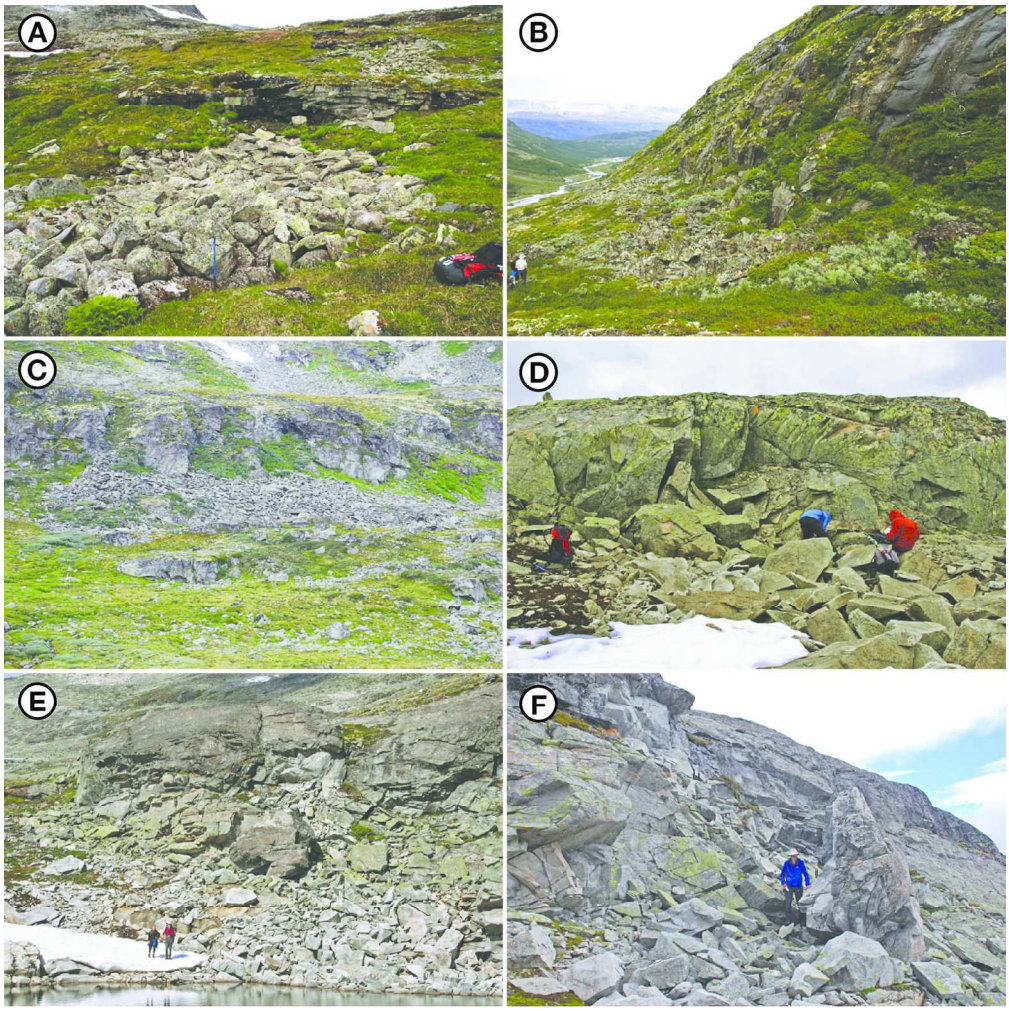

Fig. 2. Photographs of selected small rock-slope failures (SRSFs): (A) No. 23, Gravdalen; (B) Nos 7 and 8, Leirdalen; (C) Nos 34-36, Bjørndalen; (D) No. 7, Sognefjell; (E) and (F) No. 22, Gravdalen (also the site of a young control point).

174x173mm (300 x 300 DPI)

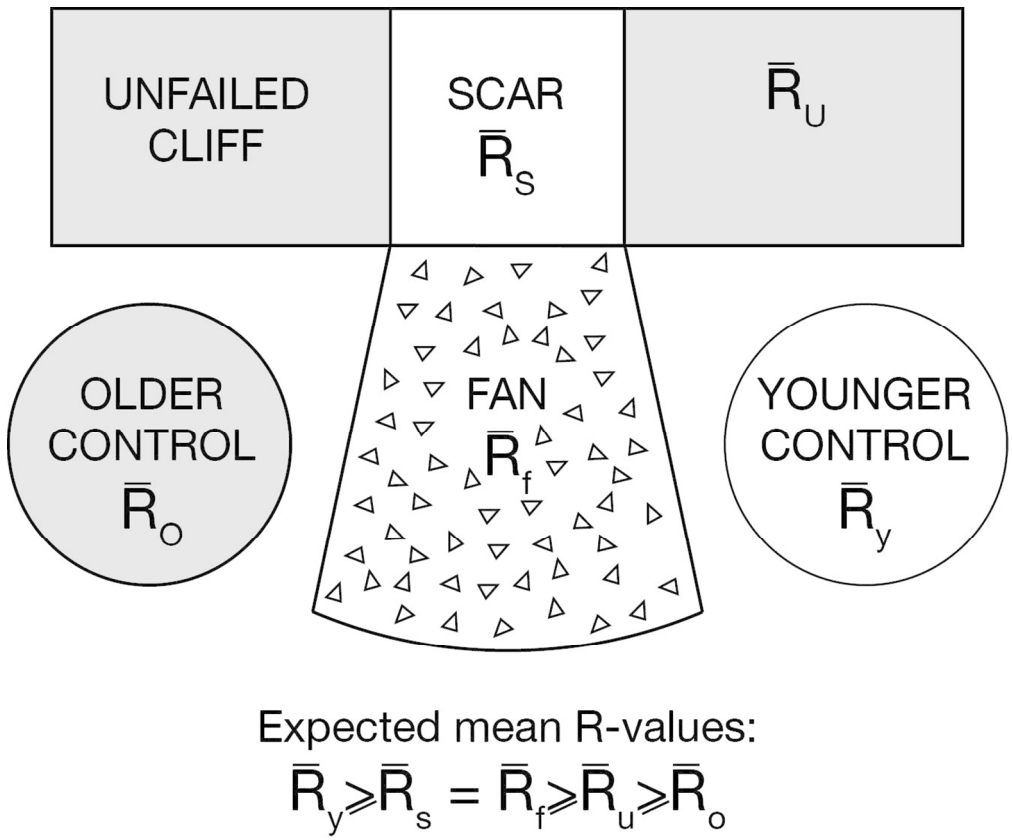

Fig. 3. Schematic of the fan-scar-cliff comparison tests with expected differences in mean R-values between fan boulders, scar bedrock surfaces, unfailed cliffs, and rock surfaces used as younger and older control-point surfaces. Expectations apply to single-event SRSF events without the possible complications discussed in the text.

113x96mm (300 x 300 DPI)

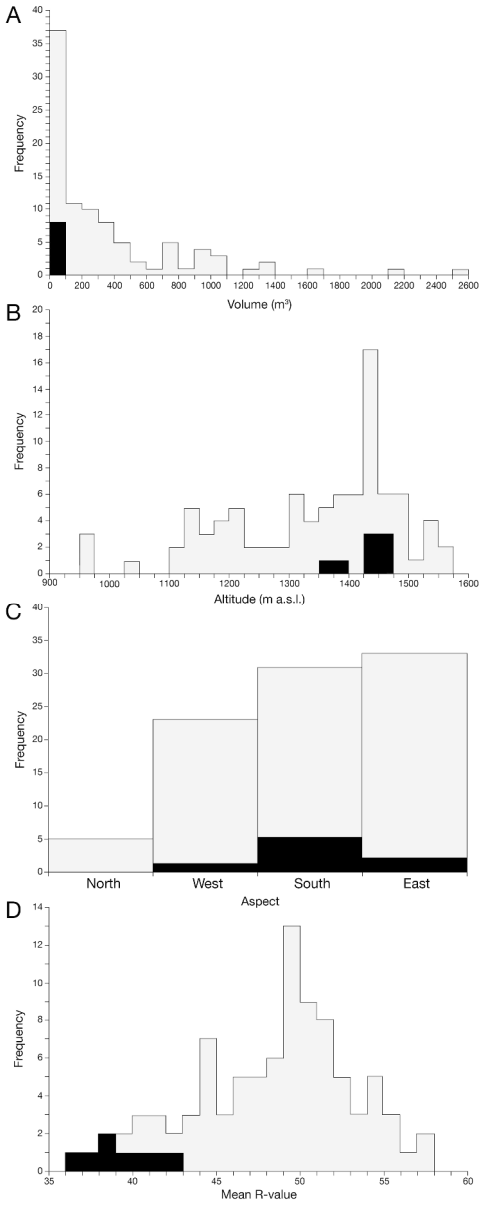

Fig. 4. Frequency distributions of four SRSF characteristics: (A) fan volume; (B) altitude; (C) aspect; (D) mean R-value. Eight sites in gabbroic gneiss (Sognefjell) are differentiated by solid black shading from 84 sites in pyroxene-granulite gneiss.

276x701mm (300 x 300 DPI)

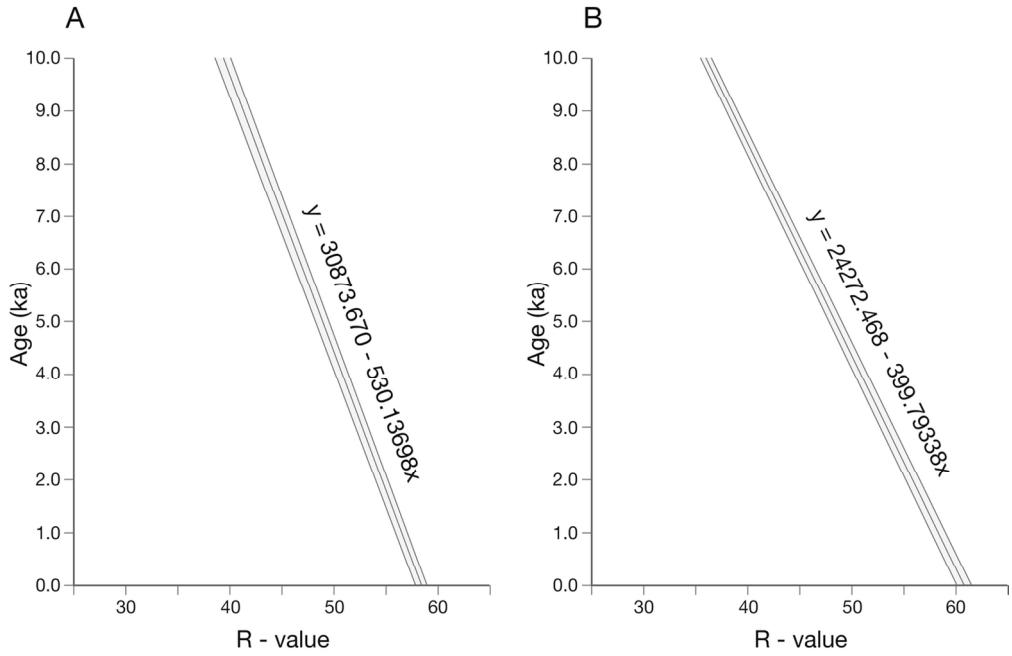

Fig. 5. Calibration curves and calibration equations for (A) pyroxene-granulite gneiss and (B) gabbroic gneiss. Note that both calibration curves are based on two control points of known age (25 years and 9700 years) using data presented in Table 3.

128x84mm (300 x 300 DPI)

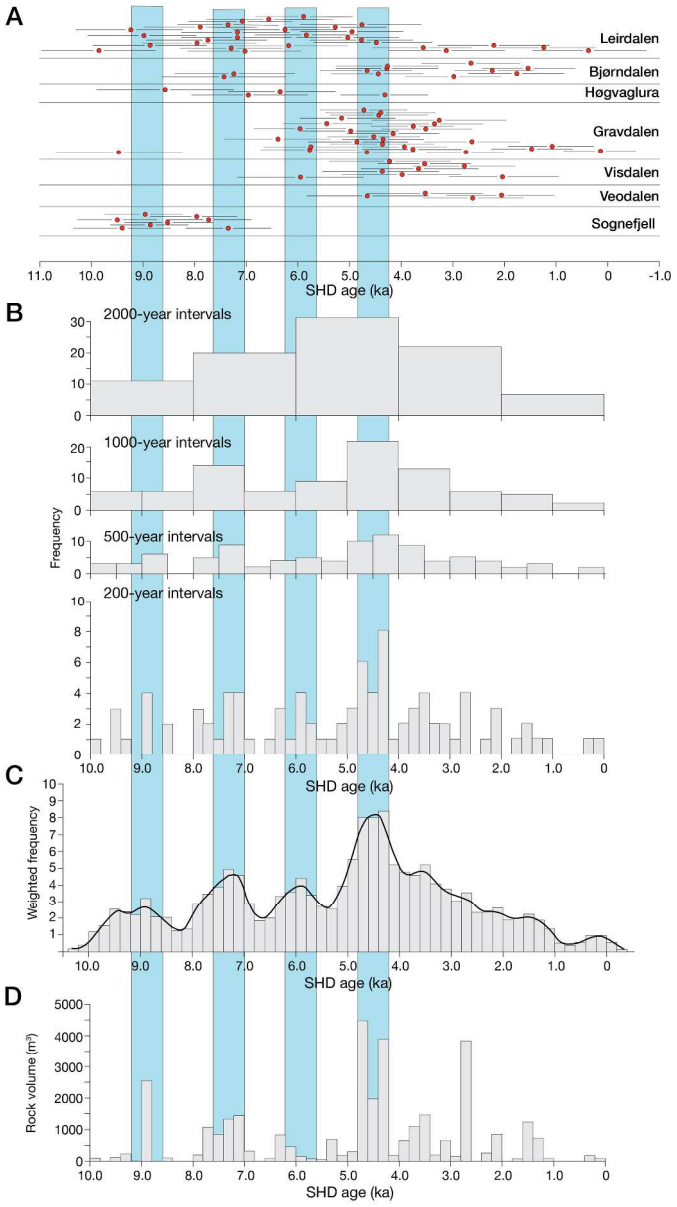

Fig. 6. Holocene SHD chronologies of SRSF activity for Jotunheimen: (A) individual SHD dates with their 95% confidence intervals in the different subregions; (B) age-frequency distributions of SRSF events at the regional level using 2000-yr, 1000-yr, 500-yr and 200-yr time intervals; (C) weighted age-frequency distribution with age-frequency curve defined by binomial smoothing; (D) variation in the magnitude of SRSF events based on rock volume using 200-year time intervals. Vertical bands (numbered) are the 4 modes in the weighted age-frequency distribution suggesting phases of enhanced regional SRSF activity.

332x598mm (300 x 300 DPI)

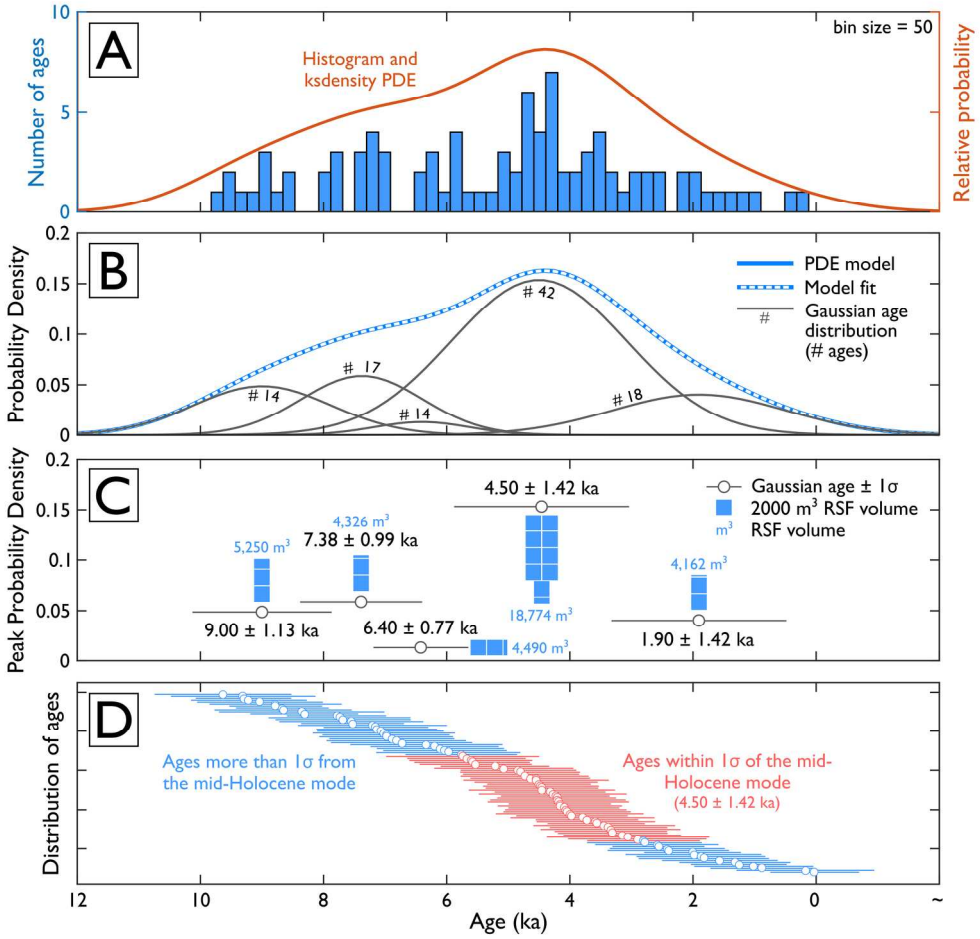

Fig. 7. Probability density function analysis of SRSF activity for Jotunheimen: (A) histogram and KS density PDE; (B) individual Gaussian age distributions (n = 5), the sum of which integrates to the cumulative PDE with a model fit that is graphically indistinguishable from from the PDE model. The number of ages listed for each Gaussian age distribution (#) exceeds the total number of SRSF events identified in Jotunheimen as some ages contribute to >1 Gaussian distribution; (C) peak Gaussian numerical ages and 1σ uncertainties for the five individual Gaussian age distributions plotted against the peak probability density (PPD). The PPD scales with the number and spatial clustering of individual ages. Reported RSF volumes are based on the sum of individual SRSF volumes (m3) which comprise each Gaussian age distribution; (D) distribution of SRSF ages, sorted by oldest to youngest. The 42 SRSF events which account for the dominant mode at 4.50 ± 1.42 ka (within 1σ) are highlighted.

190x180mm (300 x 300 DPI)

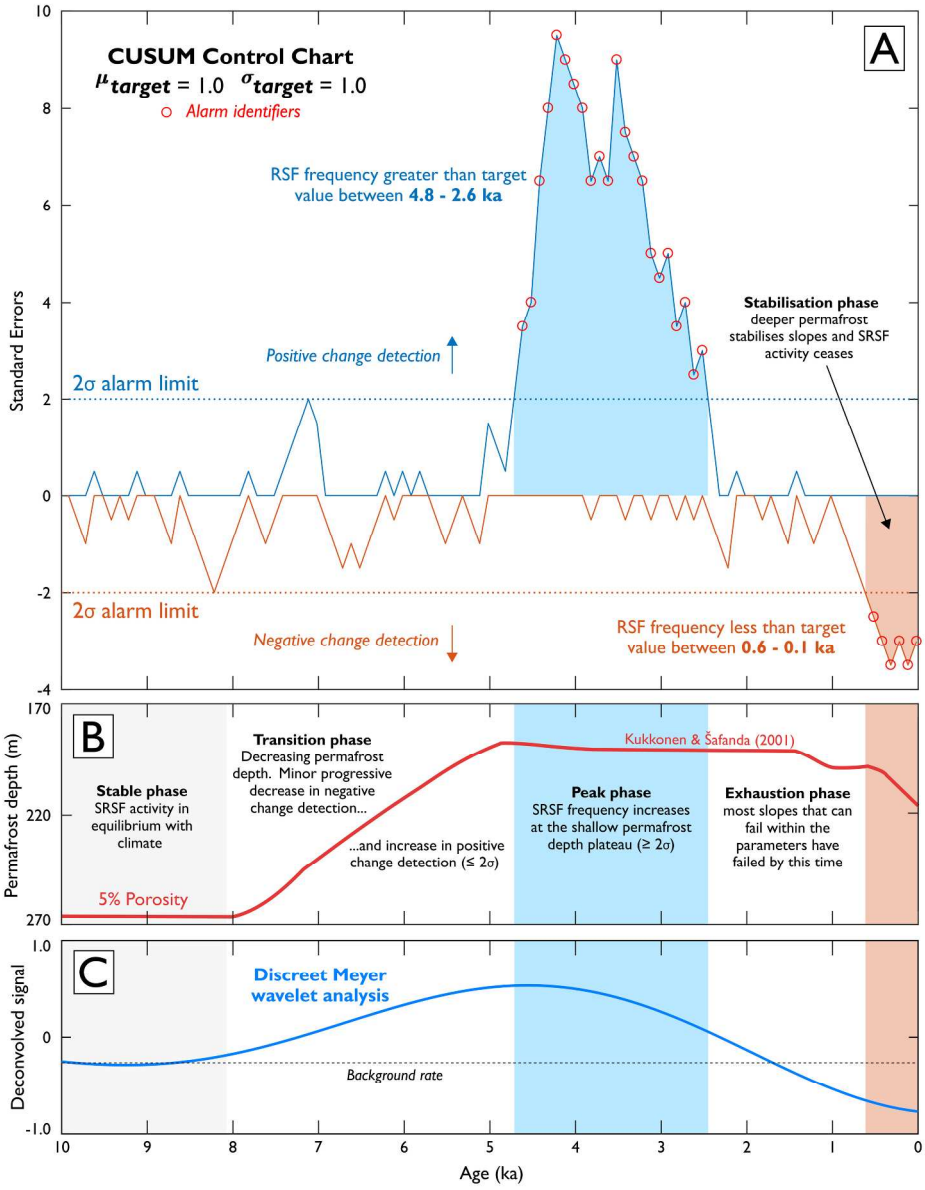

Fig. 8. Change detection and related analyses: (A) cumulative sum change detection graph showing positive (blue) and negative (orange) changes and statistically significant departures (> 2σ) from the background SRSF frequency; (B) modelled permafrost depth in Fennoscandia (5% porosity) from Kukkonen & Šafanda (2001), subdivided into five distinct phases; (C) results of discreet Meyer wavelet analysis, showing the lowest frequency decomposed signal (d6).

293x372mm (300 x 300 DPI)

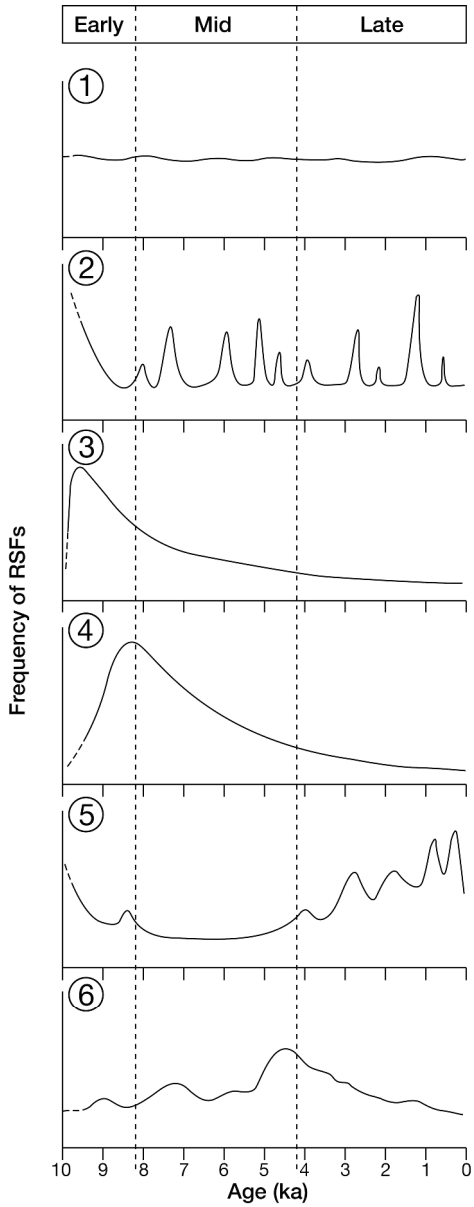

Fig. 9. Models for different patterns and causes of Holocene variations in RSF frequency and/or magnitude: (1) continuity-of-activity; (2) intermittent-earthquakes; (3) deglaciation-close-tracking; (4) deglaciation-lagging; (5) cool/wet-climate-response; and (6) the new thermally-driven permafrost-degradation model proposed in this study for SRSFs in Jotunheimen. The subdivisions of the Holocene shown are those proposed by Walker et al. (2012).

254x657mm (300 x 300 DPI)

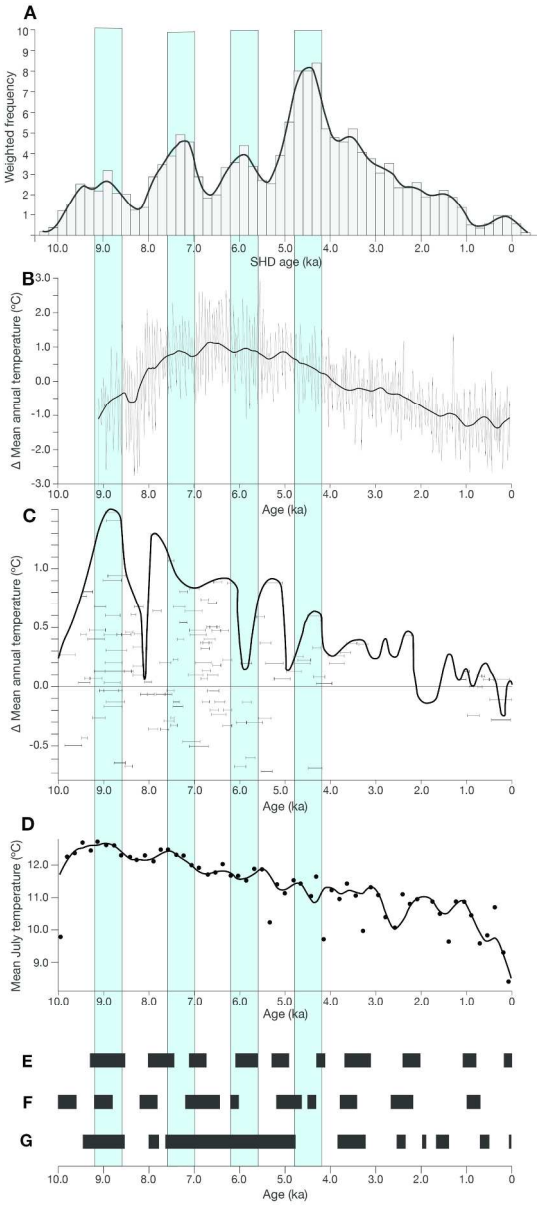

Fig. 10. Relationships between SRSF frequency in Jotunheimen and proxy climatic records: (A) temporal variations in SRSF frequency from Fig. 6C; (B) pollen-based reconstruction of annual air temperature for Northern Europe expressed as deviations from the mean (Seppä et al., 2009); (C) mean summer air temperature deviations from present in the Scandes Mountains based on pine tree-limit variations (Dahl and Nesje, 1996); (D) pollen-based July air temperature variations at Øvre Heimdalsvatnet, eastern Jotunheimen (Velle et al., 2010); (E) periods of above average air temperature (shaded) based on the GISP 2 Greenland ice core δ18O record (Alley, 2004; Wanner et al., 2011); (F) periods of above average sea-surface temperatures in the North Atlantic Ocean (shaded) based on standardized stacked ice-rafted debris (IRD) records (Bond et al., 2001; Wanner, et al., 2011); (G) periods when glaciers in the Smørstabbtindan massif, Jotunheimen, were smaller than today (shaded) based on glaciolacustrine and glaciofluvial stratigraphy (Matthews and Dresser, 2008). Vertical bands indicate phases of enhanced regional SRSF frequency (as in Fig. 6).

272x612mm (300 x 300 DPI)

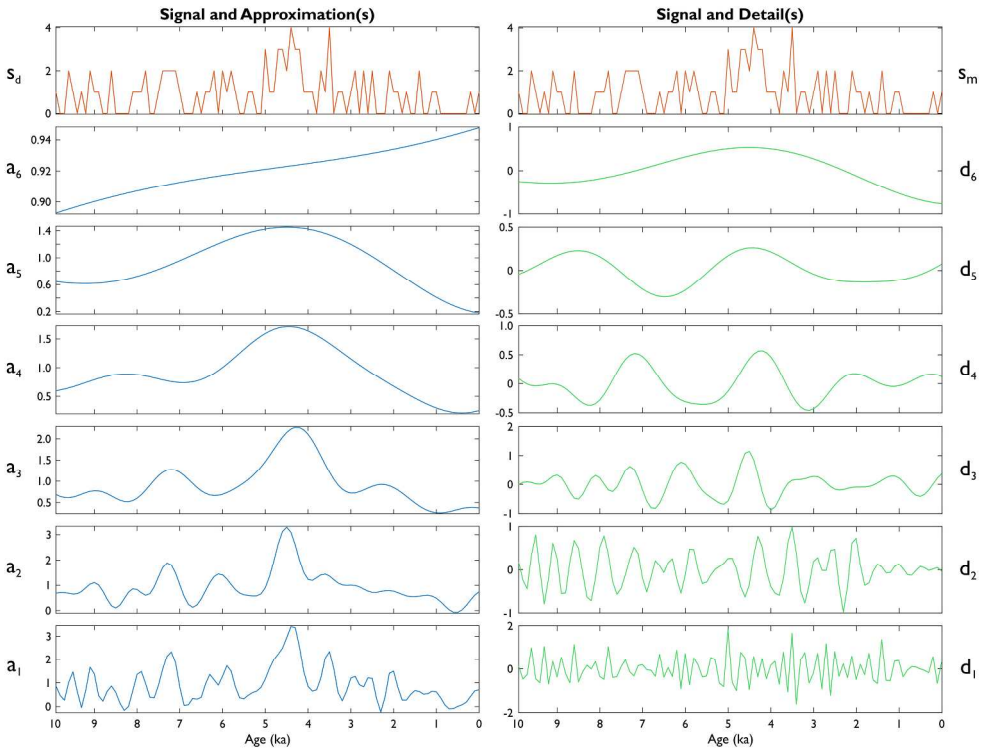

259x196mm (300 x 300 DPI)